University of Stuttgart

European XFEL

Optimizing Aerosol-Based Sample Delivery for Single Particle Imaging at X-Ray Free-Electron Lasers

Pushing the Limits: Boosting Data Collection, Minimizing Background Noise, and Expanding Sample Compatibility

Dissertation

Presented to the Faculty of Energy-, Process-, and Bio-Engineering (Faculty 4)
University of Stuttgart

For the Fulfillment of the Requirements for the Degree of
Doctor of Engineering (Dr.-Ing.)

by
Safi Rafie-Zinedine

September, 2024

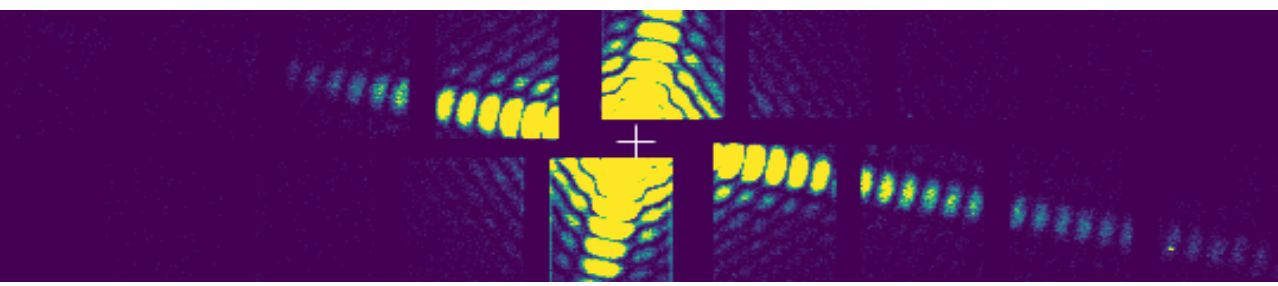

Optimizing Aerosol-Based Sample Delivery for Single Particle Imaging at X-Ray Free-Electron Lasers

Pushing the Limits: Boosting Data Collection, Minimizing Background Noise, and Expanding Sample Compatibility

Von der Fakultät 4 – Energie-, Verfahrens- und Biotechnik der Universität Stuttgart zur Erlangung der Würde eines Doktors der Ingenieurwissenschaften (Dr.-Ing.) genehmigte Abhandlung

Vorgelegt von

Safi Rafie-Zinedine

aus Swaida, Syrien

Hauptberichter: **Jun.Prof. Dr. Michael Heymann**

Mitberichter: **Prof. Dr. Filipe R. N. C. Maia**

Tag der mündlichen Prüfung: 17/09/2024

Institut für Biomaterialien und biomolekulare Systeme der Universität Stuttgart

2024

Optimizing Aerosol-Based Sample Delivery for Single Particle Imaging at X-Ray Free-Electron Lasers

Pushing the Limits: Boosting Data Collection, Minimizing Background Noise, and Expanding Sample Compatibility

Dissertation

Presented to the Faculty of Energy-, Process-, and Bio-Engineering (Faculty 4)
University of Stuttgart

For the Fulfillment of the Requirements for the Degree of
Doctor of Engineering (Dr.-Ing.)

by
Safi Rafie-Zinedine

September, 2024

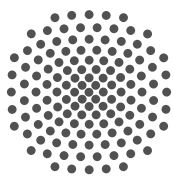

University of Stuttgart

PhD Dissertation Advisors:
Jun.Prof. Dr. Michael Heymann
Stuttgart University

Dr. Joachim Schulz
European XFEL

Dr. Johan Bielecki
European XFEL

PhD Dissertation Committee:
Prof. Dr. Andreas Kronenburg
Institute of Technical Combustion
Stuttgart University

Jun.Prof. Dr. Michael Heymann
Institute of Biomaterials and Biomolecular Systems
Stuttgart University

Prof. Dr. Filipe R. N. C. Maia
Department of Cell and Molecular Biology
Uppsala University

Dean of the Faculty:
Prof. Dr. Kai Hufendiek
Faculty 4 - Energy-, Process- and Bio-Engineering
Stuttgart University

.

Institute of Biomaterials and Biomolecular Systems
Faculty 4 - Energy-, Process- and Bio-Engineering
University of Stuttgart

Pfaffenwaldring 57
D-70569 Stuttgart
Germany

Language: English

Dedicated to
the memory of my father
Sulaiman Zinedine.

Abstract

Optimizing Aerosol-Based Sample Delivery for Single Particle Imaging at X-Ray Free-Electron Lasers

University of Stuttgart
Faculty 4 - Energy-, Process- and Bio-Engineering
By Safi Rafie-Zinedine

One of the most promising applications of X-ray Free Electron Lasers (XFELs) is the imaging of isolated particles, such as proteins, using single-particle X-ray diffractive imaging (SPI). This technique can provide high-resolution structural information on individual particles and facilitate the study of dynamic processes at the nanoscale. SPI, employing gas phase injection through an aerodynamic lens stack (ALS), has attracted significant attention due to its low background scattering and suitability for high-rate data collection. Despite these advantages, these SPI experiments encounter several challenges, especially with smaller and lighter biomolecule particles. These include low signal strength, limited collected datasets, high background scattering, and issues with sample compatibility in delivery system. In this doctoral thesis, I address the latter three challenges by developing and optimizing traditional electrospray-based gas phase sample delivery systems for SPI at XFELs. My research aims to enhance particle transmission efficiency, reduce background scattering, and expand the conductivity range of these systems to enable high-resolution imaging of smaller biological particles.

I have developed three modified electrospray systems based on the traditional system to improve SPI at XFELs: enhanced electrospray, helium electrospray (He-ES), and coaxial helium electrospray (CHeES). The enhanced electrospray, upgraded from the traditional system by exploring different neutralizers and geometries, achieves an eightfold increase in particle transmission efficiency by employing a VUV neutralizer and optimizing the counter electrode's orifice size. This enhanced system achieves over 40% particle transmission from solution to the X-ray interaction region. The He-ES system uses a 3D-printed nozzle to reduce N_2 and CO_2 usage compared to traditional electrospray while ensuring stable sample delivery. It enhances particle delivery efficiency tenfold for 26 nm-sized biological particles and decreases gas load in the interaction chamber by 80%. Lastly, the CHeES system uses a coaxial 3D-printed nozzle to accommodate a broader conductivity range up to 40 000 µS/cm—eight times higher than traditional systems, and to lower background noise using He-ES technique. In tests at the European XFEL, the CHeES system notably lowered background noise by more than threefold in helium mode.

My findings indicate improvements in transmission efficiency, background noise reduction, and sample versatility in SPI experiments, potentially enhancing both data quality and quantity. These advancements could yield higher-resolution structures and expand the scope for studying diverse biological and material science samples. My research has broader implications for structural biology, as obtaining higher-resolution structures is crucial for understanding the atomic structure of proteins and other biomolecules.

Zusammenfassung

Eine der vielversprechendsten Anwendungen von Freie-Elektronen-Röntgenlasern (XFELs) ist die Abbildung isolierter Partikel, wie Proteine, durch Einzelpartikel-Röntgenbeugungs-Bildgebung (single particle imaging, SPI). Diese Technik kann hochauflösende strukturelle Informationen über einzelne Partikel liefern und die Untersuchung dynamischer Prozesse im Nanobereich erleichtern. SPI, bei dem Proben in Gasphase durch ein aerodynamisches Linsensystem (ALS) in die Vakuumkammer eingebracht werden, hat aufgrund seiner geringen Hintergrundstreuung und seiner Eignung für die Sammlung von Daten mit hoher Rate große Aufmerksamkeit erregt. Trotz dieser Vorteile stoßen SPI-Experimente auf mehrere Herausforderungen, insbesondere bei kleineren und leichteren Biomolekülpartikeln. Diese umfassen eine geringe Signalintensität, begrenzte gesammelte Datensätze, hohe Hintergrundstreuung und Probleme mit der Kompatibilität der Proben im Liefersystem. In dieser Dissertation befasse ich mich mit den letztgenannten drei Herausforderungen, indem ich traditionelle, auf Elektrospray basierende Proben-Liefersysteme bei SPI an XFELs entwickle und optimiere. Mein Ziel ist es, die Partikelübertragungseffizienz zu erhöhen, die Hintergrundstreuung zu reduzieren und den Leitfähigkeitsbereich der Proben-Systeme zu erweitern, um hochauflösende Abbildungen kleinerer biologischer Partikel zu ermöglichen.

Ich habe drei modifizierte Elektrospraysysteme auf der Grundlage des traditionellen Systems entwickelt, um SPI an XFELs zu verbessern: verbessertes Elektrospray, Helium-Elektrospray (He-ES) und koaxiales Helium-Elektrospray (CHeES). Das verbesserte Elektrospray, das durch die Untersuchung verschiedener Neutralisatoren und Geometrien vom traditionellen System ausgehend modifiziert wurde, erreicht eine achtfache Steigerung der Partikelübertragungseffizienz durch den Einsatz eines VUV-Neutralisators und die Optimierung der Öffnungsgröße der Gegenelektrode. Dieses verbesserte System erreicht eine Partikelübertragung von über 40% von der Lösung bis zur Röntgeninteraktionsregion. Das He-ES-System verwendet eine 3D-gedruckte Düse, um den Verbrauch von N_2 und CO_2 im Vergleich zu traditionellen Elektrosprays zu reduzieren, während eine stabile Probenlieferung gewährleistet bleibt. Es steigert die Partikellieferungseffizienz um das Zehnfache für 26 nm große biologische Partikel und reduziert die Gaslast in der Interaktionskammer um 80%. Schließlich verwendet das CHeES-System eine koaxiale 3D-gedruckte Düse, um einen breiteren Leitfähigkeitsbereich der Probe von bis zu 40 000 µS/cm zu unterstützen—achtmal höher als bei traditionellen Systemen—und um Hintergrundrauschen durch die He-ES-Technik zu reduzieren. Bei Tests am European XFEL senkte das CHeES-System das Hintergrundrauschen im Heliummodus um mehr als das Dreifache.

Meine Ergebnisse zeigen Verbesserungen bei der Übertragungseffizienz, der Reduzierung des Hintergrundrauschens und der Vielseitigkeit der Proben in SPI-Experimenten, was potenziell sowohl die Datenqualität als auch die -quantität verbessert. Diese Fortschritte könnten zu höher aufgelösten Strukturen führen und das Spektrum der untersuchten biologischen und materialwissenschaftlichen Proben erweitern. Meine Forschung hat weitreichende Implikationen für die Strukturbiologie, da hochauflösende Strukturen entscheidend für das Verständnis der atomaren Struktur von Proteinen und anderen Biomolekülen sind.

Contents

List of Tables

List of Figures

List of Publications

This thesis is based on the following publications, referred to by their Roman numerals:

i **Enhancing Electrospray Ionization Efficiency for Particle Transmission through an Aerodynamic Lens Stack**
Rafie-Zinedine, S., Varma Yenupuri, T., Worbs, L., Maia, F. R. N. C., Heymann, M., Schulz, J., & Bielecki, J.
J. Synchrotron Rad. **31**, 222-232, (2024), https://doi.org/10.1107/S1600577524000158

ii **Helium-electrospray improves sample delivery in X-ray single-particle imaging experiments**
Varma Yenupuri, T., **Rafie-Zinedine, S.**, Worbs, Heymann, M., Schulz, J. Bielecki, J., L., & Maia, F. R. N. C.
Scientific Reports, **14**, 4401, (2024), https://doi.org/10.1038/s41598-024-54605-9

iii **Coaxial Helium Electrospray for Single-Particle Imaging at X-ray Free Electron Lasers**
Rafie-Zinedine, S., Schulz, J., Bielecki, J., & Heymann, M.
Submitted to J. Synchrotron Rad.

List of Additional Publications not Included in the Thesis

iv **Coherent diffractive imaging of lipid vesicles and synaptic vesicles by femtosecond x-ray FEL pulses**
Neuhaus, C., Alfken, J., Komorowski, K., Stammer, M. L., Bean, R., Bielecki, J., de Wijn, R., Letrun, R., **Rafie-Zinedine, S.**, Juncheng, E., Mancuso, A., Jahn, R., & Salditt, T.
Biophysical Journal, 122(3), 322a. (2023), https://doi.org/10.1016/j.bpj.2022.11.1803

v **Dynamics of Reversible and Irreversible Nanoplasma Processes in Spherical and Fibrous Nanoparticles**
Gerke, F., Tümmler, P. , Biswas, S., Dold, S., Rivas, D., Baumann, T., Kruse, B., Seiffert, L., Mullins, T., Grychtol, P., Ovcharenko, Y., Wassermann, B., **Rafie-Zinedine, S.**, Meyer, M., Maity, A., Polshettivar, V., Kling, M. F., Peltz, C., Fennel, T., & Rühl, E.
In preparation

vi **Dancing in the blue light: an ultrafast movie on superheated silver nanocubes**
Colombo, A., Dold, S., Haddad, A. A., Bielecki, J., Goy, F., Graf, C., Hecht, L., Jakobs, G., Joschko, M., Knopp, G., Kolatzki, K., Peltz, C., **Rafie-Zinedine, S.**, Reichenbach, T., Sauppe, M., Schenk, F., Schnorr, K., Sun, Z., Tümmler, P., Ussling, C. F., Yarema, M., Yazdani, N., Zhang, H., Moseler, M., Bostedt, C., Rupp, D., & Issendorff, B. V.
In preparation

vii **Observation of Aerosolization-induced Morphological Changes in Viral Capsids**
Mall, A., Munke, A., Shen, Z., Mazumder, P., Bielecki, J., E, Juncheng., Estillore, A., Kim, C., Letrun, R., Luebke, J., **Rafie-Zinedine, S.**, Round, A., Round, E., Rutten, M., Samanta, A. K., Sarma, A., Sato, T., Schulz, F., Seuring, C., Wollweber, T., Worbs, L., Vagovic, P., Bean, R., Mancuso, A. P., Loh, N. D., Beck, T., Kuepper, J., Maia, F. R. N. C., Chapman, H. N., & Ayyer, K.
In preparation

Acknowledgements

Embarking on this journey, I was aware of the challenges that lay ahead, but the unwavering support, insightful discussions, and invaluable assistance I have received along the way have been my guiding lights. The scientific work presented in this thesis is a testament not just to my efforts, but to the collective wisdom, encouragement, and support of many remarkable individuals to whom I owe my deepest gratitude.

First and foremost, my supervisors, Joachim Schulz and Michael Heymann, deserve special mention. Their constant encouragement and the intellectually stimulating discussions during our weekly Zoom meetings have significantly deepened my understanding of the subject. Their guidance has been paramount in shaping the direction and success of my work. I am also immensely grateful to Johan Bielecki, whose stimulating discussions and invaluable help have been a cornerstone of my research. Johan's willingness to lend his expertise and his open-door policy have been a tremendous help in navigating the myriad challenges I encountered.

Special thanks to Simon Dold, whose helpful discussions enriched my research experience, and to Mohammad Vakili and Agnieszka Wrona for their expertise and assistance with 3D printing and nozzle assembly. James Moore's help with the SEM and Matthäus Kitel's assistance with 3D printing were indispensable. Elisa Delmas deserves a heartfelt thank you for her assistance with technical drawings, and Vasilii Bazhenov for his enlightening discussion on safety in the laboratory. Marco Schrage's help with machine shop work has been invaluable, for which I am profoundly thankful.

I extend my gratitude to all the members of the Sample Environment & Characterization group and the Scientific Instrument SPB/SFX group. Your support and sense of community have made my years as a PhD student not only productive but also immensely enjoyable. The collaboration with the Uppsala group, including Filipe Maia, Tej Varma Yenupuri, and Lena Worbs, on the Helium electrospray publication, has been an enriching experience that I value deeply.

Above all, my heartfelt thanks go to my family. Your unwavering support and encouragement have been my strength and motivation. Layal, your support has been my rock, and to you, I owe an immeasurable debt of gratitude. To my family, friends, and everyone who has supported me throughout this journey, your belief in me has been a source of constant encouragement. Thank you, from the bottom of my heart.

This thesis is not just a reflection of my work, but a testament to the collective spirit of all those who have walked this path with me. Thank you for being part of my journey.

Abbreviations

ALS Aerodynamic Lens Stack

AmAc Ammonium Acetate

CDI Coherent Diffractive Imaging

CFD Computational Fluid Dynamics

CHeES Coaxial Helium Electrospray

CO_2 Carbon Dioxide Gas

CPC Condensation Particle Counter

Cryo-EM Cryo-Electron Microscopy

DFFN Double Flow Focusing Nozzle

DMA Differential Mobility Analyzer

EMC Expand-Maximize-Compress algorithm

ES Electrospray

EuXFEL the European XFEL

FWHM Full Width at Half Maximum

GDVN Gas Dynamic Virtual Nozzle

He Helium Gas

He-ES Helium Electrospray

HVE High-Viscosity Extruder

ID Inner Diameter

LCLS the Linac Coherent Light Source

LCP Lipidic Cubic Phases

N_2 Nitrogen Gas

OD Outer Diameter

PD Photo diode

PDMS Polydimethylsiloxane

PEG Polyethylene Glycol

PGMEA Propylene Glycol Methyl Ether Acetate

PS Polystyrene Spheres

PVP Polyvinylpyrrolidone

RGA Residual Gas Analyzer

SAXS Small-Angle X-ray Scattering

SFX X-ray Crystallography

SMPS Scanning Mobility Particle Sizer

SNR Signal-to-Noise Ratio

SPI Single Particle Imaging

2D Two Dimensional

2PA Two Photon Absorption

2PP Two Photon Polymerization

3D Three Dimensional

VUV Vacuum Ultraviolet neutralizer

WAXS Wide-Angle X-ray Scattering

XAS X-ray Absorption Spectroscopy

XFEL X-ray Free Electron Laser

XPS X-ray Photoelectron Spectroscopy

XRF X-ray Fluorescence

Chapter 1

Motivation

Understanding the intricate architecture of biological molecules is a gateway to unraveling the mysteries of life and health. At the heart of structural biology lies the quest to map the molecular structures of proteins and other critical biomolecules at atomic resolution, revealing how their shapes dictate their roles in life's processes. Traditional techniques, primarily x-ray crystallography, have provided a wealth of information by detailing the structures of molecules crystallized into a repetitive array. However, this method's requirement for crystallization presents a tricky barrier, as numerous essential proteins, especially many membrane proteins, stubbornly resist assembling into ordered crystals necessary for this analysis [1]. The challenge to visualize the molecular world in its full diversity has sparked a relentless pursuit of alternative methods, notably single-particle Cryogenic Electron Microscopy (cryo-EM) and the innovative use of x-ray free-electron lasers (XFELs) [2, 3].

The European XFEL is a groundbreaking facility poised to revolutionize structural biology with its ultra-short, ultra-intense X-ray pulses [4]. These capabilities are well-suited for single particle imaging experiments, capturing high-resolution structural data from single particles before radiation damage occurs. This "diffraction before destruction" principle overcomes the challenges faced by traditional methods [5]. This technique not only bypasses the need for crystallization but also opens the door to studying a broader range of biological molecules in their native states [6]. Moreover, the European XFEL's capability to provide insights into fast dynamic processes at the atomic level, see Figure 1.1, holds the potential to vastly expand our understanding of biomolecular function, mechanisms of disease, and the development of novel therapeutics [7–9]. The implications of this technology extend beyond structural biology, promising to catalyze advancements across a spectrum of scientific disciplines, including pharmacology, chemistry, materials science, and energy research, thereby

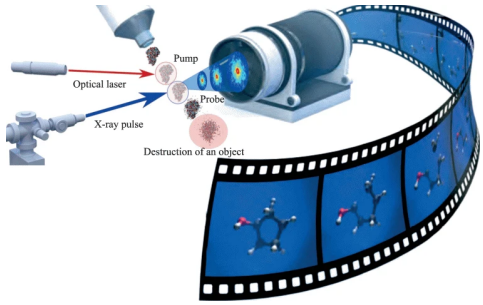

Figure 1.1: Illustration of creating molecular movies through time-resolved experiments at XFELs: Initially, an optical laser flash initiates a chemical reaction. Subsequently, pulses from the XFEL are delivered at varying intervals after the initial flash. These pulses capture snapshots of the changes occurring within the molecule. (reproduced with permission [10]).

ushering in a new era of scientific discovery and technological innovation.

On the frontier of chemistry, the European XFEL offers a window into the atomic-level mechanics of catalysis and other chemical processes, areas where mysteries abound despite their widespread applications in industry [11]. By enabling scientists to film chemical reactions with unmatched precision, the facility provides insights into the interplay between molecules and catalysts, potentially leading to more efficient production methods and novel materials. This knowledge not only paves the way for advancements in chemistry but also has far-reaching implications for environmental sustainability and the development of new energy sources, illustrating the profound impact of the European XFEL across multiple dimensions of research and innovation.

However, the single particle imaging's promise is currently tempered by significant challenges, particularly in the domain of sample delivery, detector technology, and beamline instrumentation [12, 13]. In the sample delivery aspect, the ability to present particles to the X-ray beam in an optimal state for capturing high-quality diffraction patterns is a bottleneck that hinders the realization of single particle imaging's full potential. Efficient, versatile sample delivery with minimal background noise is crucial for generating the volume and quality of data necessary for groundbreaking discoveries, yet existing systems often fall short in terms of noise reduction, compatibility with a wide range of samples, and overall efficiency.

Addressing this challenge, the thesis investigates sample delivery methods to improve the performance of single particle imaging experiments at XFELs. By focusing on the creation of a sample delivery system that is not only more efficient and reliable but also capable of handling a broader spectrum of sample types with minimal noise, the research aims to facilitate the collection of a statistically significant number of high-quality diffraction patterns from individual protein molecules, a prerequisite for achieving high-resolution structural determinations [12].

1.1 Outline of This Thesis

The aim of this study is to enhance the performance of the current electrospray (ES)-based gas-phase sample delivery system to ensure compatibility with a broader range of samples and to generate dense particle beams with minimal background scattering, which is crucial for single particle imaging experiments at XFELs. To achieve this objective, we first investigated the working principles of the electrospray as an aerosol generator, along with the aerosol injector. We then improved the setup, where 3D printing technology played a pivotal role, enabling the fabrication of high-precision nozzles for the electrospray. This work marks a significant step forward in refining sample delivery methods for single particle imaging experiments, contributing to the journey towards achieving high-resolution imaging of single proteins at XFELs. Notably, modifications to the sample delivery system were employed in experiments at the European XFEL, either in part or in entirety.

This thesis is structured as follows: Chapter 2 lays the groundwork by introducing the fundamental concepts underpinning the research presented in subsequent chapters. It explores the background of XFEL and single particle imaging, with a focus on sample delivery methods, particularly aerosol injection, and the current ES-based gas-phase sample delivery methods, highlighting their advantages and limitations. This chapter also discusses strategies to overcome these limitations, primarily through the use of high-precision 3D printing technology. Chapters 3 to 5 comprise the main results of this thesis, drawing on manuscripts that have been published or submitted to scientific peer-reviewed journals.

In Chapter 3, we examine several modifications to the ES geometry and neutralization methods within the ES setup. By studying absolute particle transmission across different neutralizers and ES setup geometries—while maintaining conditions suitable for single particle imaging experiments—we discovered that a vacuum ultraviolet ionizer achieves a transmission efficiency approximately seven times higher than that of the previously used soft X-ray ionizer. Furthermore, by optimizing the orifice size on the counter electrode, we attained more than 40% particle transmission from solution to the X-ray interaction region.

Chapter 4 introduces the Helium Electrospray [He-ES] technique, which utilizes a novel 3D-printed nozzle designed to replace most of the nitrogen and carbon dioxide gases with helium gas in the interaction chamber, as helium has a lower cross-section with x-rays. This technique minimizes gas background scattering and enhances the signal-to-noise ratio. Our modifications resulted in a significant replacement of these gases, achieving an approximately 83% decrease of N_2 and CO_2 in the interaction region.

Chapter 5 presents the development of a Coaxial Helium Electrospray [CHeES] technique, featuring a 3D-printed microfluidic coaxial nozzle, aimed at expanding the spectrum of single particle imaging samples compatible with XFEL. By employing the coaxial electrospray technique—which supports a wider range of sample conductivities—and integrating He-ES, we achieved a notable reduction in background noise and enhancement in data quality for single particle imaging experiments. The CHeES system can handle samples with conductivities up to 40,000 µS/cm, approximately an eightfold increase over the traditional ES system. We demonstrated the CHeES system's effectiveness in single particle imaging experiments at the European XFEL, observing a significant reduction in background noise (more than threefold) when operating in helium mode. Chapter 6 concludes the thesis and outlines directions for future work.

Chapter 2

Introduction

2.1 X-ray Free Electron Lasers

X-ray Free Electron Lasers (XFELs) represent the pinnacle of X-ray technology evolution, introducing a paradigm shift in the observation of molecular and atomic structures and their dynamics. They produce X-ray pulses with unique properties that significantly enhance their capabilities compared to other X-ray generating technologies such as synchrotrons. These properties include high photon energy, ultra-intense, ultra-short, and spatially coherent pulses. Additionally, the European XFEL (EuXFEL) has a high repetition rate, delivering these pulses in trains at a repetition rate of 10 Hz, with each train containing up to 2700 pulses spaced 220 ns apart [14].

The high photon energy of XFEL pulses enables deeper penetration into materials, making them particularly advantageous for dense or thick samples in various scientific fields such as biology, material science, and geophysics. This capability allows for the examination of the internal structures of these samples, providing insights that are mostly inaccessible through surface or thin sample techniques like Cryo-EM.

Ultra-intense pulses contain an extremely high number of photons, which is critical for generating strong signals from very small or weakly scattering samples that would not produce detectable signals with less intense beams [15]. This high intensity enhances the signal in the collected data. One of the most groundbreaking applications of XFELs is in single-molecule imaging, where ultra-intense pulses can indeed illuminate individual molecules. This enables researchers to capture detailed structural information without the need to crystallize the molecules, opening up new possibilities for studying non-crystallizable molecules.

Although high-intensity pulses might imply a greater potential for sample damage, the ultra-short duration of XFEL pulses, measured in femtoseconds (10^{-15} seconds), enables capturing images before the deposited energy significantly damages the sample. This phenomenon, known as "diffraction before destruction," preserves the natural state of the biomolecules under study [5], as shown in Figure 2.1. This is particularly advantageous for biological samples sensitive to radiation. Another benefit of these ultra-short pulses is their exceptional temporal resolution, allowing scientists to "freeze" motion at the femtosecond scale [2, 15]. This enables the observation of rapid events, such as electron movements within atoms or molecules during chemical reactions—events previously inaccessible with longer pulse durations. These time-resolved studies, essential for understanding dynamic processes, track changes in a system over time after being triggered by an external stimulus. For instance, in pump-probe experiments, an initial "pump" pulse, often from a laser, triggers a reaction or state change in a sample, and subsequent XFEL "probe" pulses capture snapshots at different intervals, revealing dynamics on atomic and molecular scales. Many chemical reactions and physical changes occur on the femtosecond scale, and XFELs enable real-time observation of these processes, which is crucial for understanding fundamental phenomena in chemistry, physics, and materials science. This capability allows visualization of state transitions, electron transfer reactions, and other ultrafast events.

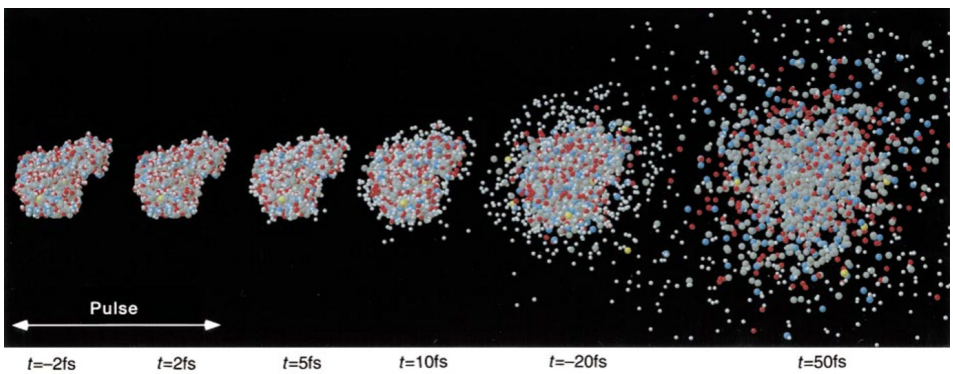

Figure 2.1: Illustration of the diffraction-before-destruction concept, demonstrated by a time-resolved experiment at an XFEL using the T4 lysozyme protein subjected to varying X-ray pulse durations. This highlights an inertial delay in protein explosion with shorter pulses of 2 fs pulse duration and subsequent disintegration. (reproduced with permission [5]).

Synchrotron sources, though highly useful for a broad range of applications, typically emit x-ray pulses in the range of a few picoseconds (10^{-12} seconds) which are longer compared to the femtosecond pulses from XFELs [15]. These shorter pulses from XFELs allow for the study of ultrafast processes approximately 1000 times faster than those observable with synchrotrons. In terms of intensity and light coherence, XFELs generate coherent x-ray pulses that are billions of times more intense than those

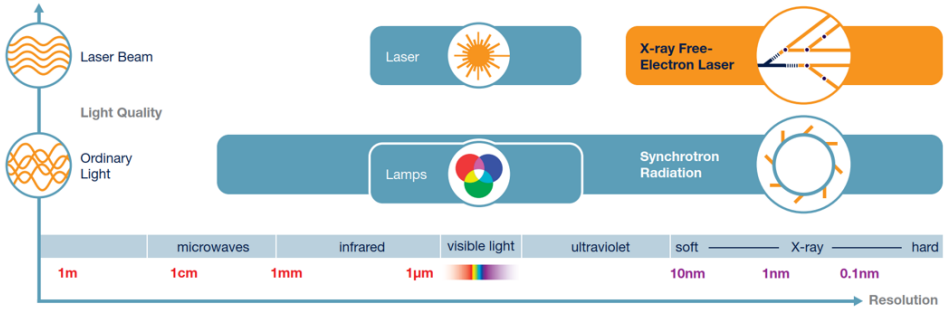

Figure 2.2: Comparison of light sources in terms of light quality and wavelength. It details the range of wavelengths emitted by various light sources and describes their light coherence properties, particularly emphasizing the capability of XFEL facilities (highlighted in orange) to produce coherent X-ray light. (reproduced with permission from European XFEL GmbH).

produced by modern synchrotrons, facilitating the observation of small and weakly scattering samples, see Figure 2.2.

Cryo-EM is another powerful tool for studying molecular structures at high resolution; however, it typically operates at millisecond timescales [3]. XFELs, with their ultra-short pulses, can capture events that occur within the femtosecond to millisecond range, enabling scientists to observe molecular dynamics that are too fast for cryo-EM. Additionally, since cryo-EM requires samples to be frozen, it can introduce artifacts not present in the natural, dynamic state of the sample. By studying samples in a more natural state without the need for freezing, XFELs provide a clearer view of biological or chemical processes as they naturally occur.

The XFEL process starts in the injector where electrons are produced, typically through photoemission. In this method, high-intensity laser light illuminates a photocathode material, which emits electrons via the photoelectric effect [2, 16, 17] . These electrons are then collected into compact bunches using electric fields and magnetic devices called bunching cavities. These cavities adjust the electron speeds within the bunch, allowing tighter grouping as they move through the accelerator. Following this, the electrons enter a linear accelerator (LINAC), where radiofrequency (RF) cavities accelerate them to high energies, often several gigaelectronvolts (GeV), up to 17 GeV for the EuXFEL. Tuned to the electron frequency, these RF cavities provide energy boosts at precise intervals to enhance acceleration efficiency. The electrons reach speeds close to the speed of light, maximizing their kinetic energy for X-ray production.

After being accelerated, the electron bunches are directed into a series of devices called undulators, consisting of alternating magnetic poles [18]. As the electrons navigate through these poles, they follow a sinusoidal path, inducing a "wiggling" motion. This movement causes the electrons to emit radiation due to acceleration. Initially, the radiation is incoherent. However, within the undulators, a key phenomenon

known as Self-Amplified Spontaneous Emission (SASE) occurs [19]. As high-energy electrons pass through the magnetic fields of the undulator, they follow a sinusoidal trajectory, emitting X-rays spontaneously with random phases and directions, resulting in incoherent radiation. These emitted X-rays interact with the electron beam, creating an oscillating electric field that influences electron motion. This interaction causes the electrons to bunch at intervals corresponding to the emitted X-ray wavelength, a phenomenon known as microbunching, which is crucial for amplification. As microbunched electrons travel through the undulator, they emit more X-rays in phase with the initial spontaneous emission, leading to constructive interference and significantly amplifying X-ray intensity. X-ray photons travel faster than electrons, so precise control of the delay between electron bunches and emitted X-rays is crucial. The undulator is designed to keep electrons and X-ray photons in sync over its length, allowing effective amplification. The process of microbunching and coherent emission causes an exponential increase in X-ray intensity. Each subsequent section of the undulator contributes to this amplification, with electron bunches becoming more tightly packed and emitted X-rays more coherent. Eventually, amplification reaches saturation, where energy transfer from the electron beam to the X-rays becomes less efficient, and X-ray intensity growth slows down. At this point, the initially incoherent X-ray emission has transformed into a highly coherent and intense beam. After several passes through the undulators, the light becomes highly coherent, enhancing brightness and narrowing the emission spectrum. The resulting ultra-intense, ultrashort, coherent X-ray pulses are then transported to various instrument stations for experimental use.

The beam transport path in an XFEL is maintained under high vacuum conditions to minimize the interaction of the X-ray beam with air molecules, which can absorb or scatter photons, thereby degrading beam quality and increasing background noise on the detector [18]. This vacuum is achieved using a series of vacuum pumps, such as turbomolecular and ion pumps, that continuously evacuate air from the beamline. Additionally, the vacuum system includes beamline isolation valves capable of quickly isolating sections in the event of a vacuum breach or other issues. These valves are crucial for protecting the vacuum integrity of the beamline, ensuring system stability, and preventing widespread contamination or damage.

Between the undulators and the instrument stations, the X-ray beam passes through various beamline components that manipulate and control the beam according to the specific needs of experiments at the instrument stations [16, 17]. These components include attenuators, made from materials such as diamonds, which control the beam's intensity. Shutter systems block the beam when not in use, maintaining safety and operational integrity. Alignment support systems, cameras, and Yttrium Aluminum Garnet (YAG) screens aid in visualizing and adjusting the beam's position and pro-

file. Monochromators, employing crystals or gratings, refine the beam to a specific wavelength by selectively filtering X-rays. Slits, adjustable apertures in the beam path, clean the beam by trimming its edges and removing stray photons and diffraction artifacts, thus shaping the beam profile. Focusing systems utilize Kirkpatrick-Baez (KB) mirrors, precisely curved mirrors arranged to focus the beam. Lastly, beam diagnostics systems, comprising various sensors and detectors, measure properties such as intensity, shape, energy spectrum, and pulse length to ensure the beam meets specific experimental requirements.

At the instrument stations, X-rays facilitate a variety of scientific experiments, including [20]:

- Wide-Angle X-ray Scattering (WAXS): Measures X-ray scattering patterns deflected at small angles upon encountering a sample, capturing high-resolution details.
- Small-Angle X-ray Scattering (SAXS): Similar to WAXS but focuses on very small scattering angles to explore larger structures with lower resolution.
- X-ray Fluorescence (XRF): Analyzes secondary X-rays emitted from a material after excitation by an X-ray beam.
- X-ray Absorption Spectroscopy (XAS): Measures X-ray absorption by a material as a function of energy, revealing details about the electronic states and local structures around specific atoms.
- X-ray Photoelectron Spectroscopy (XPS): Measures the kinetic energy of electrons ejected from a material when irradiated with X-rays, providing information on elemental and chemical states of surfaces.
- X-ray Raman Scattering (XRS): investigates low-energy excitations, including phonons and low-energy electronic transitions in materials. This technique enhances traditional Raman spectroscopy by utilizing X-rays instead of visible light. XRS is particularly useful for studying materials under extreme conditions, such as high pressures and temperatures.
- X-ray Crystallography (SFX): Determines the atomic and molecular structures of crystals by measuring the angles and intensities of diffracted X-ray beams, creating a three-dimensional electron density map.
- X-ray microscopy: Combines X-ray imaging with microscopic techniques for high-resolution imaging at the nanometer scale.

- X-ray tomography: Especially Computed Tomography (CT), captures X-ray images from various angles around an object and reconstructs them into cross-sectional slices, which can be further assembled into a 3D model.
- X-ray Imaging: Creates images of an object's internal structure, with methods tailored for specific contrasts and resolutions.
- Single particle imaging: Integrates X-ray diffraction and imaging to determine the structure of individual particles, such as proteins, without crystallization.

2.1.1 Single Particle Imaging

Coherent diffractive Single Particle Imaging (SPI) at XFELs is an advanced technique in structural biology and nanoscience, providing unparalleled views of atomic and molecular structures of isolated particles. This method involves exposing identical particles to an X-ray beam and capturing their diffraction patterns based on the 'diffraction-before-destruction' principle, as shown in Figure 2.3. These patterns facilitate the 2D and sometimes 3D reconstruction of structures, eliminating the need for sample crystallization.

However, the 3D reconstruction of a particle's structure from diffraction patterns in SPI experiments introduces its own complexities, notably in phase retrieval—an essential step that involves deciphering the phase information lost during the detection of diffraction patterns. To reconstruct the sample's electron density, the diffraction intensity in Fourier space is measured experimentally, while the phase information is retrieved computationally [17]. To properly understand this reconstruction process, it is essential to start with the fundamental concepts of sample electron density in real space and its Fourier transform in reciprocal space, along with the necessary notation to describe the phase problem in SPI.

The electron density of a sample, denoted as $\rho(r)$, represents the spatial distribution of electrons within the sample at position r in real space. This function quantifies the electron concentration at various points in a material and is fundamental to understanding the sample's structure at the molecular or atomic level. In the context of XFEL and SPI, the real space coordinate, r, is a vector representing a point in three-dimensional space where the electron density is measured[1]. In SPI, the electron density $\rho(r)$ is not directly observable. Instead, the experiment measures the diffraction pattern in Fourier space, or reciprocal space. The Fourier transform of the electron density in reciprocal space ($\hat{\rho}(q)$) is a complex function representing the

[1]The real space coordinate r is typically expressed in units of nanometers (nm) or Angstroms (Å) when dealing with atomic and molecular scales.

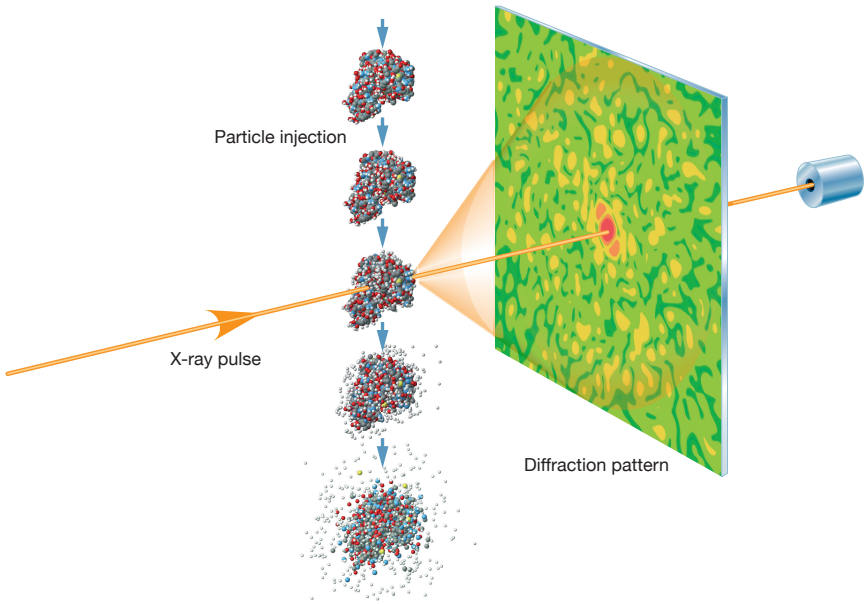

Figure 2.3: Schematic of coherent diffractive single particle imaging at XFELs: A stream of single particles intersects with a femtosecond X-ray pulse. The interaction scatters X-rays from the sample, creating a diffraction pattern captured by a pixelated detector. Concurrently, the X-ray pulse photo-ionizes the sample, inducing plasma formation and a Coulomb explosion in the highly ionized particle. This sequence allows for the capture of a single diffraction pattern from each particle. A large dataset of these patterns, collected from identical particles in random orientations, is analyzed to reconstruct the particle's 3D structure. (reproduced with permission from European XFEL GmbH).

amplitude and phase of waves that reconstruct the electron density $\rho(r)$ upon inverse transformation. It is calculated as:

$$\hat{\rho}(q) = \int \rho(r) \exp(-2\pi i q \cdot r)\, dr$$

where q is the reciprocal space coordinate, a vector in reciprocal space, directly related to the angles at which X-rays are scattered by the sample. It is defined in inverse units of real space (e.g., inverse Angstroms).

One of the primary challenges in SPI is the phase problem. During the measurement of diffraction patterns, detectors count only photons, and therefore, only the intensity of the scattered waves, $I(q)$, is recorded, not the phase information. This intensity, representing the squared magnitude of $\hat{\rho}(q)$, is given by:

$$I(q) = |\hat{\rho}(q)|^2$$

While this intensity is directly observable in experiments, the phase information, $\phi(q)$, essential for reconstructing the image, is lost during this process, leading to

the phase problem where the challenge is to retrieve:

$$\hat{\rho}(q) = \sqrt{I(q)} \exp(i\phi(q))$$

where $\phi(q)$ denotes the phase of the wave at each point in reciprocal space.

To reconstruct $\rho(r)$ from $I(q)$, it is necessary to computationally retrieve the lost phase information. The inverse Fourier transform is employed to convert the measured intensities, alongside the computationally retrieved phase, back into the real-space electron density:

$$\rho(r) = \int \hat{\rho}(q) \exp(2\pi i q \cdot r)\, dq$$

Phase retrieval is complex and typically requires iterative algorithms to estimate $\phi(q)$. The process is further complicated by noise and experimental errors, which can distort the measured diffraction patterns.

The Gerchberg-Saxton algorithm is one of the simplest and earliest methods developed for phase retrieval [21, 22]. This iterative algorithm alternates between real and reciprocal spaces to estimate missing phase information from measured intensity data. It begins with an initial guess for the phase, $\phi_0(q)$, often assumed to be zero or a random distribution. The initial Fourier amplitude is then calculated as $\hat{\rho}_0(q) = \sqrt{I(q)} \exp(i\phi_0(q))$. The process continues iteratively: first, compute the inverse Fourier transform to estimate the real-space electron density:

$$\rho_n(r) = \int \hat{\rho}_n(q) \exp(2\pi i q \cdot r)\, dq$$

Next, apply real-space constraints by modifying $\rho_n(r)$ to fit known constraints, such as non-negativity and support constraints. Then, compute the Fourier transform of the modified real-space density:

$$\hat{\rho}'_n(q) = \int \rho'_n(r) \exp(-2\pi i q \cdot r)\, dr$$

Enforce measured intensities by replacing the amplitude of $\hat{\rho}'_n(q)$ with the square root of the measured intensities while preserving the computed phase:

$$\hat{\rho}_{n+1}(q) = \sqrt{I(q)} \exp(i \arg(\hat{\rho}'_n(q)))$$

Repeat the iterative process until convergence is achieved, typically indicated by minimal changes between successive iterations or by reaching a maximum number of iterations.

Since the Gerchberg-Saxton algorithm was introduced, significant advancements in phase retrieval have enhanced the robustness and efficiency of image reconstruction from diffraction data. Notably, Fienup's algorithms, including the Hybrid Input-Output (HIO) and Error Reduction (ER) methods, address the non-convex nature of phase retrieval [22]. These methods improve convergence and accuracy by iteratively refining phase guesses and applying real-space constraints effectively. Additionally, the use of oversampling methods, which collect more data points than the Nyquist sampling theorem requires, leverages redundant information in oversampled Fourier transforms. This enhances solution stability and uniqueness, making the algorithms more resistant to noise and experimental imperfections. The Shrinkwrap algorithm further advances phase retrieval techniques by dynamically adjusting the support constraint of the electron density map based on the evolving reconstruction [23]. This adaptation focuses the retrieval process on the most relevant parts of the diffraction pattern, thereby improving convergence rates and the quality of the final image. These developments collectively advance the accurate reconstruction of complex structures in coherent diffractive imaging.

The Expand-Maximize-Compress (EMC) algorithm is another method designed for addressing the challenges of SPI data from XFEL experiments [24]. It uses an iterative process to fit a model of the particle to the measured diffraction patterns. This process involves adjusting the model to make the synthetic diffraction patterns it generates align as closely as possible with the actual measured patterns. This approach effectively reconstructs the particle without explicitly calculating the phase at every point, focusing on finding a model that best explains the observed data. This algorithm processes millions of noisy, incomplete, and unoriented diffraction patterns from identical copies of a single particle. It comprises three steps: Expand, Maximize, and Compress. In the expand step, the EMC algorithm transforms each observed diffraction pattern into a full set of potential orientations to construct a detailed three-dimensional intensity model, representing a probability distribution of all possible orientations and positions. The maximize step refines this model to better match the experimental data by adjusting intensities and orientations, enhancing the likelihood of the observed data fitting the model through iterative refinement. The compress step reduces the complexity of the model by consolidating similar structures and orientations, effectively compressing the data into a more manageable form while retaining the essential features needed for accurate reconstruction.

Implemented in software like Dragonfly and utilizing parallel computing frameworks such as MPI+OpenMP, the EMC algorithm efficiently handles large data volumes and complex computations required in XFEL experiments [25]. After constructing the 3D intensity model of the diffraction volume, the next task involves retrieving phase information lost during the measurement process, as only intensities are captured. The

EMC algorithm aids in this by robustly modeling the origins of each diffraction pattern within the volume. Phase retrieval is then achieved through iterative techniques that estimate the phases, which, when combined with the intensities, reconstruct the sample's real-space structure. However, the EMC algorithm encounters several challenges: it must deal with the inherently noisy and incomplete nature of diffraction data from XFEL experiments, necessitating advanced noise filtering and data processing techniques. Moreover, it requires substantial computational resources, including memory and processing power, to handle and analyze large datasets.

The successful reconstruction of a particle's structure at atomic resolution in SPI at XFELs depends significantly on the quality and quantity of the diffractive patterns captured during experiments. A high Signal-to-Noise Ratio (SNR) is essential, as it ensures that details within the diffraction pattern are clearly distinguishable from the noise [26, 27]. This clarity is crucial because the finer details of the pattern, corresponding to higher spatial frequencies, encode information about the atomic-scale structures within the sample. Moreover, the phase retrieval process, crucial for reconstructing both the amplitude and phase of the wavefront from the measured intensity, depends heavily on this clarity. Noise primarily affects the lower intensity regions of the diffraction pattern, which can lead to errors in estimating the phase information. Such misestimation directly impacts the accuracy and fidelity of the reconstructed real-space image. Furthermore, most phase retrieval algorithms, including the Gerchberg-Saxton and Fienup algorithms, are iterative and sensitive to initial conditions and data quality. Noise can cause these algorithms to converge to incorrect solutions or to fail to converge, especially when the iterative steps amplify the noise level in each cycle. To mitigate the effects of low SNR, methods such as oversampling are employed, where the Fourier transform of the object is sampled more frequently than the Nyquist rate [28]. Although this redundancy helps stabilize the phase retrieval, it requires the collection of more data.

Over time, driven by advances XFELs and computational data analysis, SPI has transitioned from theory to a practical tool. It successfully determined the structures of samples, including cells [29], viruses [30–39], cell organelles [40], proteins [27], lipid vesicles and synaptic vesicles [41], and inorganic nano-particles [42, 43].

Despite significant achievements, SPI faces key challenges in reconstructing high-resolution structures, particularly with smaller, lighter biological samples [44]. To enhance both the quality and quantity of diffraction data for better reconstruction, several areas can be optimized. These include improving sample delivery systems to increase the efficiency of particle transport into the X-ray beam's path, reducing background noise from the delivery medium, and ensuring compatibility with a diverse range of samples. Additionally, increasing the X-ray fluence from XFELs can enhance the signal from weakly scattering particles, although it can also increase the

background scattering, by providing more diffracted photons in the diffraction pattern. Advancements in detector technology could reduce intrinsic noise and support higher acquisition rates, and implementing advanced computational algorithms can optimize phase retrieval and improve the accuracy of reconstructed images.

2.2 Sample Delivery Systems for SPI Experiments

At the heart of a successful SPI experiment lies the challenge to efficiently deliver samples to the interaction region of an XFEL in a manner that maximizes data quality and quantity while minimizing sample consumption. Among the diverse strategies developed for this purpose, liquid jet systems, fixed target, and gas phase injections stand out for their unique capabilities. Each of these methods plays a crucial role in the evolving landscape of SPI experiments.

Liquid jet systems employ several devices for delivering samples in a fluid medium. Notably, the Gas Dynamic Virtual Nozzle (GDVN) injector allows sample delivery within an uninterrupted liquid stream, achieving tunable stream diameters by adjusting the nozzle size and gas flow [45, 46]. This system utilizes a sheathing gas to create a "virtual" nozzle, accelerating and focusing the liquid into a cylindrical jet with diameters as small as a few micrometers, as illustrated in Figure 2.4. GDVN technology has been applied in various X-ray scattering experiments, including SFX, SAXS, and WAXS [8, 13, 46–53].

However, the GDVN injector, while widely used, exhibits several disadvantages, particularly for SPI. Its use of a liquid carrier medium results in strong X-ray scattering, which elevates background signals and complicates the measurement of diffraction patterns from weakly scattering samples, such as biological samples, where the contrast between the liquid and the biomolecule is low. Additionally, the creation of shockwaves can damage upstream samples, an issue mitigated in gas-phase injection, thereby underscoring aerosol injectors' distinct benefit.

Furthermore, GDVN injectors exhibit high sample consumption rates, typically with flow rates of 20 μL min^{-1}, for stable jets of protein crystal suspensions exceeding 10^{11} crystals per mL. These rates pose challenges for valuable or hard-to-obtain samples [53]. The stability of the liquid jet in the GDVN injector is sensitive to the flow rate, and lower flow rates may not be suitable for all samples. To address this issue, the double-flow focusing nozzle (DFFN) was developed, as documented by Oberthuer *et al.* in 2017 [56]. The DFFN employs a coaxial, faster-flowing outer liquid (typically ethanol) to focus an inner sample stream, forming a fine jet within an ethanol jet, which is subsequently focused by a coaxial gas flow, similar to traditional GDVN se-

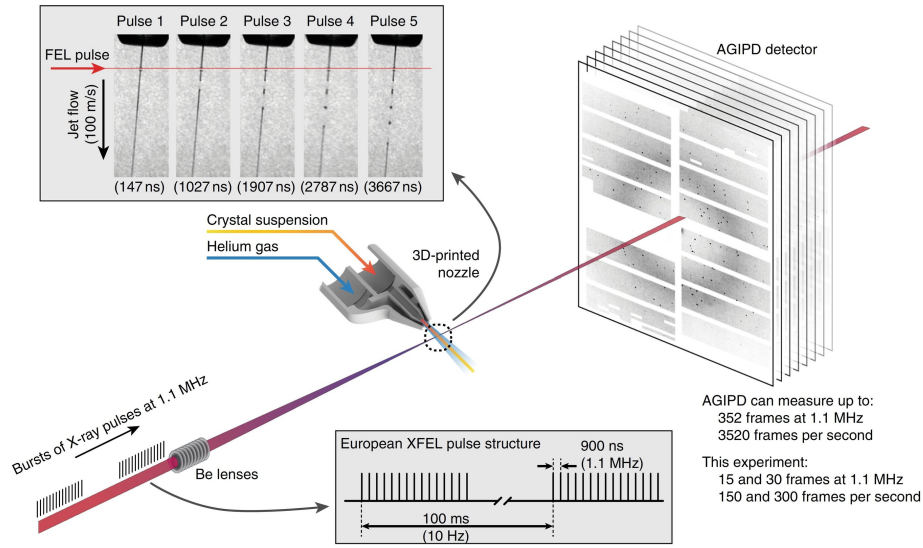

Figure 2.4: A GDVN-based sample delivery system at the European XFEL features a 3D-printed GDVN nozzle that produces a liquid jet with a diameter of 1.8 µm and speeds ranging from 50 m/s to 100 m/s. This jet is directed into the focus of the X-ray beam, where the scattered X-rays are captured by the AGIPD detector. The inset displays a sequence of images showing the jet at a speed of 100 m/s at various times post-X-ray pulse, illustrating the recovery process of the jet to deliver fresh sample for the subsequent pulse. (reproduced with permission [54]).

tups. With this configuration, where the jet mainly consists of the sheath liquid, the DFFN enhances nozzle operational stability. Another approach to minimize sample consumption involves developing segmented flow systems. These systems generate sub-nanoliter crystal suspension droplets, segmented by an immiscible oil, which significantly reduces sample waste. This method aligns with the requirements for rapid sample replenishment necessitated by the EuXFEL's MHz repetition rates [57].

Liquid sheet jet systems represent another advancement in liquid jet technology that addresses the challenges posed by radiation-induced explosions and variations in the effective interaction volume [55]. Unlike cylindrical jets, which are affected by the X-ray pointing instability and thus exhibit variable interaction volumes, liquid sheet jets offer a consistent, planar surface. These systems enhance sample delivery by increasing the surface area available for interaction with the XFEL beam, as illustrated in Figure 2.5. Additionally, they may reduce background scattering and provide a more predictable background. However, despite these advantages, liquid sheet jets consume samples at an average rate of approximately 100 μL min^{-1}, which is higher than the already substantial consumption rates of conventional jets.

Additionally, traditional liquid jet systems faced challenges in delivering viscous samples, such as membrane proteins in lipidic cubic phases (LCP) or other viscous media.

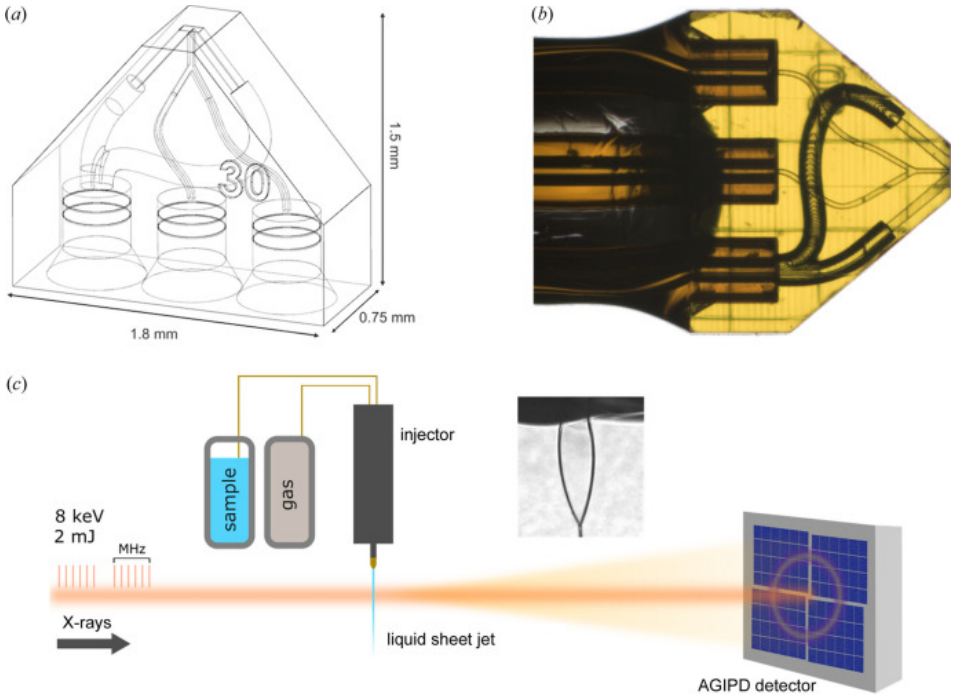

Figure 2.5: A sheet jet-based sample delivery system at the European XFEL utilizes a 3D-printed nozzle to produce a liquid sheet jet. a) The CAD drawing shows the nozzle's design, featuring two liquid inlets merging into a single channel above the nozzle tip, with gas channels originating from a single inlet and set at an 80-degree angle. b) Photograph of the assembled sheet jet nozzle. c) The experimental arrangement at the SPB/SFX beamline. (reproduced with permission [55]).

These samples, difficult to crystallize in aqueous environments, risk denaturation, aggregation, or degradation outside their native lipid contexts. To overcome this, the high-viscosity extruder (HVE) was introduced by Weierstall *et al.* in 2014, enabling the production of wide streams of crystal suspensions at flow rates ranging from 0.05 to 2.0 μL min^{-1} [58].

The fixed target method involves depositing samples onto a solid support, such as silicon nitride membranes, amorphous carbon films, or microfluidic chips, selected carefully based on their compatibility with the sample and the experimental requirements. Once deposited, the samples are scanned through the X-ray beam [59, 60], as shown in Figure 2.6. This technique has found widespread application in various fields, notably in the study of 2D crystalline samples and in Coherent Diffractive Imaging (CDI) experiments at synchrotrons, owing to its several distinct advantages. These include significant reductions in sample consumption compared to other methods, and a comparatively straightforward setup and execution process. Additionally, the fixed target method proves indispensable in scenarios requiring specific sample orientations or experiments aimed at characterizing the X-ray beam itself.

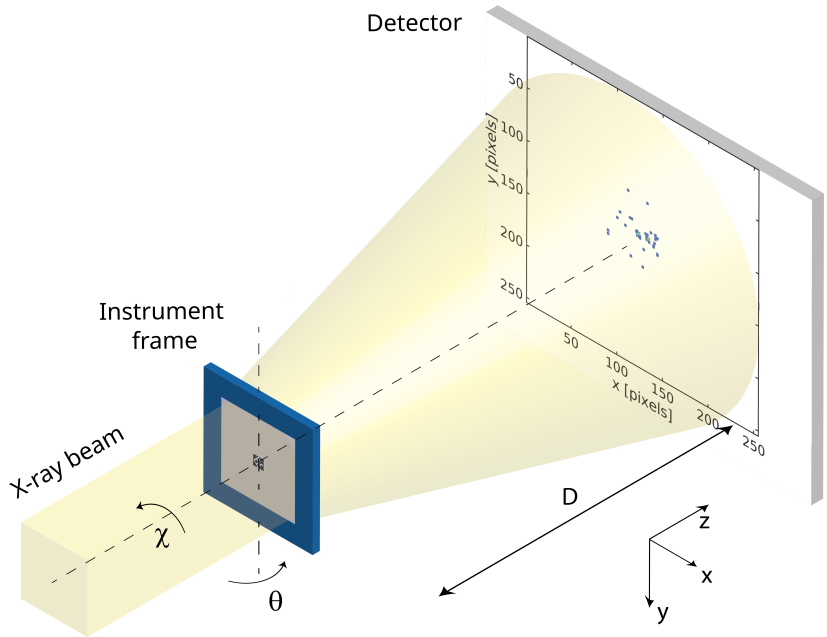

Figure 2.6: A fixed target-based sample delivery system at the European XFEL uses a gold nanostructure sample mounted on a silicon nitride membrane, which is secured to an instrument frame. This frame allows rotation around the y-axis by angle θ and in-plane rotation around the z-axis by angle χ. Such configuration permits the acquisition of diffraction patterns from multiple orientations relative to the x-ray axis, z. (reproduced with permission [59]).

However, despite its numerous benefits, the fixed target method faces the challenge of strong background noise, often overshadowing the sample's signal, especially when silicon nitride is used as the support material [13]. The genesis of this noise can be traced to the interaction between the X-ray beams and the support material, as X-rays interact with both the sample and the support. Any scattering from the latter contributes to the background noise observed in the experimental data, which can significantly hinder the analysis of diffraction patterns and make interpreting results challenging, particularly in cases involving small or weakly scattering samples. To mitigate this issue, the development of the support material, including its composition and thickness, is crucial.

Another challenge with the fixed target method, which is only compatible with low repetition rates typically lower than 10 Hz in stepping mode, arises from the time required to move to the next sample between exposures [60]. To address this challenge, ongoing efforts are focused on developing compact, fast positioning systems that can accurately position samples within micrometers, while allowing movements of up to 100 mm. However, in sweeping mode, the repetition rate can reach up to 120 Hz.

In response to these challenges, aerosol-based gas phase systems, particularly those

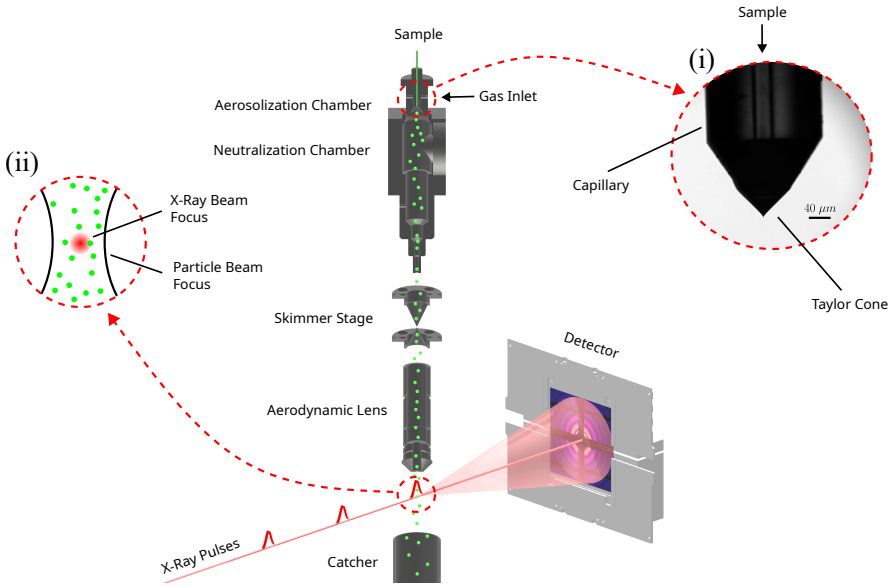

Figure 2.7: An ES-based sample delivery system at the European XFEL, displaying the ES at the top where the sample is aerosolized and neutralized, then transported through the skimmer stages to remove excess gas. The sample is subsequently focused into the interaction chamber, by an aerodynamic lens, where it intersects with the XFEL beam. The scattered photons from the sample are then recorded by a detector. (i) A typical Taylor cone, (ii) illustration of the interaction region where the X-ray beam focus is significantly smaller than the particle beam focus. Source [61]: Safi Rafie-Zinedine et al, J. Synchroton Rad., 2024 (reproduced with permission from IUCr Journals).

utilizing an Aerodynamic Lens Stacks (ALS), have gained attention for their potential to overcome the limitations of traditional delivery methods [30, 40], as illustrated in Figure 2.7. This approach provides numerous benefits, such as reduced sample consumption, enhanced scattering contrast, minimized background scattering, the elimination of shockwave issues in liquid mediums, and the capacity for high-rate data collection, taking advantage of unique facilities like the European XFEL, known for its high repetition rates and rapid data acquisition potential. These features make ALS-based systems an attractive option for SPI experiments, particularly for studying smaller particles, such as proteins and viruses, which require precise sample delivery and minimal background noise for high-resolution particle reconstruction.

2.2.1 Gas Phase Injection Systems

The introduction of gas phase injection systems through ALS has significantly advanced SPI at XFELs [30, 40, 44, 46, 62, 63]. Several types of aerosol generators that can be used in these systems, including atomizers, nebulizers, GDVNs, and Electrosprays (ES). Each method relies on distinct mechanisms to generate aerosols, giving them unique advantages and limitations that make them suitable for specific applica-

tions.

Atomizers, among the earliest aerosolization technologies, transform liquids into aerosol droplets primarily using shear forces [64]. In typical atomizers, such as pressure atomizers, the liquid is expelled through a narrow orifice under high pressure. The fast-moving liquid, encountering resistance from the surrounding air, is broken into droplets by shear forces. This simple, robust design accommodates a range of liquid viscosities and compositions. However, atomizers often generate large droplets, typically ranging from 50 to 500 microns in diameter, and a broad spectrum of droplet sizes. This can be disadvantageous in applications that require smaller droplets and precise control over droplet size distribution. Atomizers are widely used in perfumes, paint sprayers, fuel injectors, and inhalation therapies.

Jet nebulizers utilize compressed gas to convert liquid into fine droplets [64, 65]. As the gas moves through a narrow channel, it accelerates and is directed towards a capillary nozzle. Passing through the nozzle, the high-velocity flow creates a low-pressure area, the Venturi effect, that draws liquid up due to the pressure differential. When the liquid meets the high-velocity airstream at the nozzle, it is broken into fine droplets by impaction and shear forces. However, nebulizers often produce large droplets ranging from 1 to 10 microns and exhibit a broad spectrum of droplet sizes. They are typically limited to aqueous solutions that are not overly viscous. Nebulizers are widely used in medical devices for respiratory therapies, treating conditions like asthma and cystic fibrosis.

Ultrasonic nebulizers use high-frequency ultrasound waves to induce vibrations in the liquid, generating capillary waves on its surface [64, 65]. As these waves gain amplitude from continuous ultrasonic energy, their crests become sharply peaked. Eventually, the surface tension and cohesive forces within the liquid at these peaks are insufficient to hold it together against the vibrational disturbances, resulting in droplet formation. However, ultrasonic nebulizers are constrained by the viscosity of the liquid and potential degradation of heat-sensitive substances due to ultrasonic heat. Typically, they produce larger, more uniform droplets of a few microns compared to jet nebulizers. These devices are commonly used in medical inhalation therapies.

GDVN nozzles can generate liquid jets as previously discussed, but they can also used as a droplet source and integrate with an aerosol injector using an aerodynamic lens stack for SPI experiments. They aerosolize liquid by forcing it through a micron-sized orifice surrounded by a high-speed gas sheath, typically an inert gas like nitrogen (N_2) or helium (He). This gas sheath forms a virtual nozzle that focuses and accelerates the exiting liquid into a fine jet [45, 46, 53]. As the jet breaks up due to Rayleigh instability, where the liquid's surface tension cannot maintain its form against gas disturbances, droplets form. The droplet size can be adjusted by varying parameters such as gas

pressure, liquid flow rate, and orifice size. GDVN is recognized for producing smaller droplets compared to the previous generators, from 500 nm to a few microns, offering enhanced control over droplet formation and resulting in more uniform aerosols. However, challenges persist, including the difficulty in generating sufficiently small mono-disperse droplets and the tendency of non-volatile buffer components to adhere to the sample, complicating the acquisition of valid single particle images [44], which require even smaller droplets to minimize sample contamination. Using GDVN nozzles as a droplet source in the aerosol injector for SPI experiments, a flow rate of 2 μL min^{-1} was previously employed [44]. However, even with this lower flow rate compared to the flow rate used in liquid jet mode, GDVN systems still tend to consume large amounts of sample.

ES, a technique that uses electrical forces to generate aerosols of nano- to micrometer-sized droplets, offers an effective solution for producing fine, uniform droplets while minimizing sample consumption [44, 66]. The droplets generated via ES are smaller and more uniform, ranging from tens of nanometers to a micron, than those produced by the other methods, such as GDVN [44], nebulizers, or atomizers. ES's ability to produce highly uniform and controlled droplet sizes makes it particularly suitable for applications requiring precise sample delivery. These applications include mass spectrometry, drug delivery [67], thin-film deposition, particle encapsulation [68], the fabrication of nanoparticles [69], fuel spraying, ink-jet printers, colloid microthrusters [70], and SPI experiments at XFEL, leading to virtually contaminant-free sample delivery [44]. However, the performance of ES can be sensitive to the electrical properties of the liquid.

2.2.2 The Physics of Taylor Cone Formation

Understanding the formation of the Taylor cone involves delving into the fundamental physics of electric fields interacting with liquid surfaces. At a basic level, when an electric field is applied to a conductive liquid at a nozzle, it induces charges on the liquid's surface. These charges experience a repulsive force that, when sufficiently strong, overcomes the liquid's surface tension, deforming the liquid surface into a cone-jet meniscus, termed the Taylor cone, at the nozzle's tip. This balance between the electrostatic force pulling the liquid outward and the surface tension striving to minimize surface area, pulling the liquid inward, is critical for the formation of the Taylor cone [66, 71, 72].

The process of droplet formation from the Taylor cone is equally governed by fundamental physical principles. As the electric forces continue to deform the liquid, the apex of the cone becomes increasingly sharp until it reaches a point where the electric field strength is enough to overcome the cohesive forces of the liquid, causing the

emission of a fine jet that subsequently breaks up into droplets. This breakup is influenced by perturbations in the jet flow, leading to the formation of highly charged, small, uniformly sized droplets due to the Plateau-Rayleigh instability [73, 74].

This Plateau-Rayleigh instability, rooted in fluid dynamics and interfacial science, explains the breakup of a continuous liquid stream into discrete droplets. This phenomenon, seemingly simple, is driven by the intricate balance of forces such as surface tension, inertia, and viscosity [75]. When a liquid jet experiences perturbations, like diameter variations, and if these perturbations' wavelength surpasses the jet's circumference, they amplify, causing the jet to fragment. The physics underlying this phenomenon can be further understood through a detailed examination of the forces at play. The surface tension seeks to minimize surface area, while the inertia of the liquid resists changes in motion, and viscosity dissipates kinetic energy into heat, opposing the flow's deformation. In the absence of external forces, a perfect cylinder of liquid would remain stable. However, any disturbance—no matter how small—can set the stage for the instability to develop. These disturbances can be amplified by the electric field in ES processes, where the charged nature of the jet and surrounding medium introduces electrostatic forces into the mix, complicating the dynamics further. When the electric field at the apex of the Taylor cone becomes sufficient to eject a jet, it not only initiates the flow but also imposes an additional stabilizing or destabilizing force, depending on its interaction with the charged liquid. The electric forces can elongate the jet, enhancing the effects of any present perturbations. As these perturbations grow, the jet's uniformity is lost, leading to constrictions and bulges along its length. The points of constriction, where the jet is thinnest, experience the highest curvature and thus the highest surface tension force per unit length, driving the jet to pinch off at these locations and form droplets [73–75].

The size of the droplets generated in the ES process is determined by several factors, including the flow rate of the liquid, the properties of the liquid (such as its viscosity and surface tension), and the strength of the applied electric field [76]. Theoretical models help in predicting the emission radius from the tip of the Taylor cone and, consequently, the size of the resulting droplets.

In the static solution context, the formation of the Taylor cone is characterized by an equilibrium state wherein the electrical field is aligned perpendicularly to the conducting liquid surface. This configuration generates an electrostatic force that balances the force exerted by surface tension, with gravitational forces considered negligible for simplicity [Fig. 2.8]. The pressure exerted by surface tension, denoted as P_γ, is expressed in spherical coordinate system (r, ϕ, θ) by the equation [76]:

$$P_\gamma = \gamma \, \frac{\cos\varphi}{(1 - \cos^2\varphi)} \, \frac{1}{r}$$

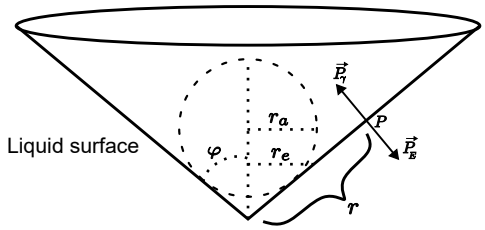

Figure 2.8: Illustration of the Taylor Cone which characterized by the interplay of two primary forces on its surface: the surface tension pressure, denoted as P_γ, and the electrostatic pressure, denoted as P_E. These forces collectively facilitate the formation of the Taylor Cone. The cone angle is represented by φ, while r signifies the distance of a given point P from the cone's tip. Additionally, r_e is defined as the radius of the emission zone at the Taylor Cone's tip, and r_a represents the radius of curvature at the tip of the cone.

where γ represents the surface tension coefficient, φ is the angle of the liquid cone, and r is the distance of a given point P on the liquid surface from the cone's tip. Conversely, the electrostatic pressure P_E, which endeavors to extend the liquid outward, is quantified in spherical coordinate system (r, ϕ, θ) by [76]:

$$P_E = \frac{1}{2}\,\epsilon_0 \phi_0^2 r^{2(n-1)} \left[\frac{\partial}{\partial\theta} P_n(\cos\theta)\right]^2$$

Here, ϕ_0 signifies the electrical potential constant, P_n corresponds to the Legendre Polynomial of degree n, and ϵ_0 the vacuum permittivity. For equilibrium to prevail,

$$P_\gamma = P_E$$

the conditions dictate that P_γ and P_E must exhibit identical dependence on r, necessitating that n equals 0.5. Concurrently, the orthogonality of the electric field to the fluid surface results in a liquid cone angle φ of 49.3°, derived from the relationship [76, 77]:

$$\theta_P = 180^\circ - \varphi = 130.7^\circ \quad \Longrightarrow \quad \varphi = 49.3^\circ$$

where θ_P represents the complementary angle to φ.

When considering a dynamic solution, where the fluid is in motion, the situation becomes more complex. The voltage drop over the cone alters the balance of forces, typically resulting in a smaller cone angle [76]. This dynamic scenario is more representative of practical ES processes, where fluids are often flowing. The change in cone angle with fluid flow indicates the sensitivity of the Taylor cone's shape to both external electric fields and internal fluid dynamics.

A theoretical approximation for dynamic cases has been derived in [76], applicable primarily under experimental conditions that closely align with the static Taylor Cone, wherein the liquid surface serves as an equipotential plane. To estimate droplet size

under these conditions, it is essential to determine the size of the zone from which the liquid is ejected. At high flow rates, a liquid jet emerges from the apex of the Taylor Cone, subsequently breaking into droplets. Conversely, reduced flow rates result in shorter jets, with the lowest flow rates producing droplets directly from the cone's tip, thereby aligning the emission diameter with the droplet diameter. While the droplet size typically surpasses the emission diameter, reducing the flow rate can enhance their alignment. For sufficiently low flow rates,

$$r_e = r_{droplet}$$

where r_e is the emission radius from the Taylor Cone's tip. This radius is given by [76]:

$$r_e = \left(\frac{\rho}{4\pi^2 \gamma \tan(\frac{\pi}{2} - \varphi) \left[\left(\frac{U_a}{U_T} \right)^2 - 1 \right]} \right)^{1/3} Q^{2/3}$$

where ρ is the fluid density, γ is the surface tension, φ is the liquid cone angle, U_a is the applied voltage, U_T is the threshold voltage, and Q the flow rate of the liquid.

Another model proposed to calculate droplet size in ES processes is the scaling law developed by Gañán-Calvo and Montanero. This model expresses the droplet diameter ($d_{droplet}$) as [78, 79]:

$$d_{droplet} = k \left(\frac{\rho \epsilon_0}{\sigma K} \right)^{\frac{1}{6}} Q^{\frac{1}{2}},$$

where $k \simeq 1.2$, with an error margin of below ±15%, is a constant. Here, ρ represents the density of the liquid, ϵ_0 is the vacuum permittivity, σ is the surface tension, K is the conductivity of the liquid, and Q is the liquid flow rate.

This scaling law has been experimentally validated across a range of liquids and flow rates, demonstrating good agreement with experimental data. However, other experimental studies, as reported in [53, 80], have observed deviations from this scaling law, indicating that the droplet size follows:

$$D \sim Q^{\frac{1}{3}}$$

Apart from the extensively studied cone-jet mode, ES can exhibit various modes. Building on the insights provided by Chen et al. (1995) regarding ES modes, ES can display various modes under different operating conditions [66, 73, 74, 81, 82]. These include the dripping, pulsating, cone-jet, multi-jet, and the silver bullet modes. Each mode presents unique characteristics affecting droplet size, distribution, and spray stability—essential factors for optimizing ES applications in diverse fields, from nanomaterial synthesis to drug delivery systems.

The dripping mode occurs at lower applied voltages and is characterized by droplet formation directly at the tip of the ES capillary, without forming a stable jet. This results in larger, less charged droplets, making it generally less suitable for applications that require high monodispersity or precise droplet size control. As voltage increases, so does the current, due to a higher frequency of dripping events. This mode is relatively stable but transitions to more complex modes with increased voltage.

With further voltage increases, the system may shift to the pulsating mode before reaching the cone-jet mode. The pulsating mode features an unstable liquid meniscus oscillating between rounded and cone shapes, leading to variability in droplet formation and size distribution. The current remains nearly constant in this mode, resulting in a wider size distribution due to diverse liquid shapes and breakup mechanisms.

The cone-jet mode, highly sought after for ES applications, is known for producing highly monodisperse, finely controlled droplet sizes. It is marked by a stable Taylor cone from which a thin liquid jet is emitted. The current increases at the onset of this mode and then stabilizes, facilitating the production of monodisperse droplets with finely adjustable sizes by modulating the liquid flow rate and electrical conductivity of the liquid.

At higher voltages, the ES may enter the multi-jet mode, characterized by the simultaneous emission of multiple jets from the liquid surface. Although this mode can increase droplet production throughput, it may compromise uniformity and control over the droplet size distribution. The current drastically increases compared to other modes, and stability becomes less predictable, making droplet size control more challenging.

Interestingly, the "silver bullet" mode, introduced by Chen et al. [66], is observed when the applied voltage is slowly increased, allowing the liquid to wet the outer surface of the capillary. This mode produces a bullet-shaped, brightly shining liquid meniscus under microscopic observation, yielding slightly larger droplets than the cone-jet mode but with good monodispersity and stability. It allows for lower voltage operation, providing a potentially energy-efficient alternative for producing monodisperse aerosols. The current is similar to or slightly higher than that of the cone-jet mode but remains stable over time, ensuring consistent droplet formation.

2.3 ES-Based Gas Phase Injection System For SPI Experiments

The ES-Based system for SPI experiments comprises two components: an ES-based aerosol generator that transforms sample particles into neutral aerosol particles, and an aerosol injector that eliminates excess gases and directs the aerosol particles into the

interaction region, as shown in Figure 2.7. Utilizing this system, numerous successful SPI experiments have been conducted at XFEL facilities on a variety of samples, including cells [29], cell organelles [40], proteins [27], viruses [30–39], and inorganic nanoparticles [42, 43].

2.3.1 ES-Based Aerosol Generator

The design of the ES-based aerosol generator for SPI involves two main chambers: aerosolization and neutralization, separated by an orifice disk plate [44, 66], as shown in Figure 2.9. The aerosolization chamber converts sample solutions into charged aerosol droplets via an ES process initiated at a tapered nozzle's tip. This nozzle is made from a single glass capillary with an outer diameter of 360 μm and typically an inner diameter of 40 μm. Droplet size is adjustable by modifying solution flow rate in the ES setup, while Taylor cone stability is managed by varying the electrical potential, carrier gases, and sample conductivity. Such precise control ensures the aerosols' uniformity and reproducibility, crucial for the success of SPI experiments.

After aerosolization, charged droplets enter the neutralization chamber. Here, soft X-ray neutralizer ionize nearby gas molecules into positive and negative ions, which neutralize the droplets [83]. The droplets capture ions of the opposite charge. After solvent evaporation, this process leaves behind neutral sample particles. These particles are then transported via conductive tubing to the inlet of the aerosol injector setup. The neutralization step is crucial for preventing particle accumulation on grounded surfaces.

Integral to the operation of the ES aerosol generator are the gas flow and electric circuits that facilitate the generation, transportation, and neutralization of aerosolized particles, as shown in Figure 2.9. The gas circuit controls the flow rate of carrier gases (CO_2 and N_2) and the sample solution by adjusting the differential pressure across the capillary, thereby managing the liquid flow rate. In the electrical circuit, the sample reservoir is set to a positive high voltage, while the orifice plate, aerosolization chamber, and neutralization chamber are grounded. This circuit ensures the electrical conditions necessary for Taylor cone formation.

To monitor the stability of Taylor cone, an optical system comprises a fiber-coupled LED light source, infinity-corrected objectives, a tube lens, and a CCD camera, facilitating high-resolution observation of the Taylor cone in the aerosolization chamber [61].

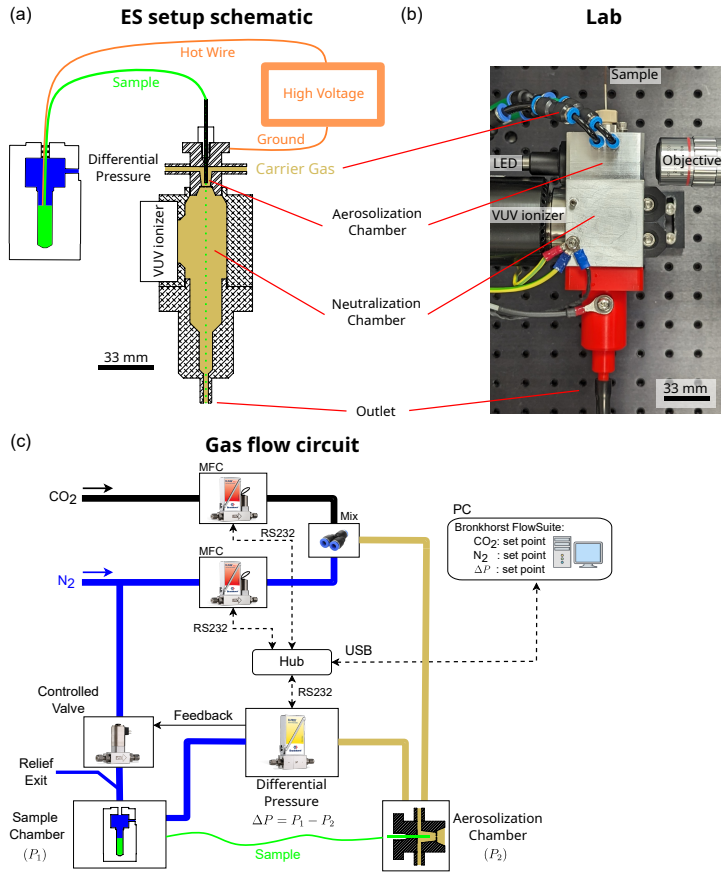

Figure 2.9: Illustration of the ES system used in aerosol injectors for SPI experiments at XFELs. (a) Diagram of the ES process, where a sample forms a Taylor cone and is aerosolized. This aerosol travels to a neutralization chamber where it is neutralized by a vacuum ultraviolet (VUV) ionizer before moving to the interaction chamber. (b) Laboratory setup of the ES system. (c) Diagram of the gas flow circuit, including gas flow meters, differential pressure sensors, and valves for controlling the flow rates of the sample and carrier gases. (reproduced with permission [61]).

2.3.2 ES-Based Aerosol Injector

Aerosol injectors are essential in SPI experiments for manipulating and focusing aerosolized particles for X-ray beam interaction. The "Uppsala injector" has notably contributed to improving sample delivery and data acquisition in SPI experiments [30, 40]. This design incorporates a two-stage nozzle-skimmer system and an ALS [63].

The nozzle-skimmer stage design, which involves precisely shaped and positioned nozzle and skimmer, effectively refines the particle beam by eliminating excess gas and allowing particles to pass through [44]. The nozzle and the skimmer are concentrically

aligned, with an adjustable gap between them, which is connected to a rough pump. Operating on fluid dynamics principles, it creates a differential pressure system to manage gas density. As aerosols move from a high-pressure nozzle to a lower-pressure area, the gas expands, causing some to diverge from the particle stream. A rough pump connected to this area removes the diverging gas. Larger particles, less affected by this divergence due to their inertia, continue straight towards the skimmer's opening, maintaining their trajectory as surrounding gas is diverted. The skimmer's shape and angle are crucial for effective gas-particle separation. After the first skimmer, particles enter another differential pressure stage and a second skimmer, further reducing gas presence. This staged process ensures particles are optimally prepared for XFEL beam imaging with minimal accompanying gas [63, 84, 85].

Following the initial preparation by the nozzle-skimmer stages, the aerosolized particles encounter the ALS, a critical component for focusing the particle beam into the interaction region [86, 87]. This focusing is achieved through a carefully designed series of lenses that manipulate the flow of particles based on aerodynamic principles, ensuring that a dense particle beam intersects with the X-ray. The lens stack's ability to increase particle density at the point of interaction directly correlates with a higher hit rate, crucial for obtaining large datasets of diffraction patterns of identical particles and then improving the statistical analysis for particle reconstruction. The ALS functions based on fluid dynamics, using Bernoulli's Principle, as the aerosol accelerates through the narrow regions of the lenses, the pressure decreases [87–90]. This mechanism regulates particle movement and speed. Moreover, the design promotes laminar airflow, minimizing turbulence and ensuring a smooth passage of particles through the system, following the gas flow lines when drag and other gas-related forces outweigh gravity or Brownian motion. By varying the lens diameters, the stack induces converging airflows that accelerate particles and narrow the beam. As particles traverse the lens stack, they undergo acceleration and focusing, culminating in a focused beam. At the end of the ALS, there is a nozzle that focuses the particle beam onto the interaction region with the X-ray beam. So, the focus of the particle beam intersects with the focus of the X-ray beam.

2.4 Challenges in ES-Based Gas Phase Injection System

To understand the challenges associated with ES-based gas phase injection systems in SPI experiments at XFELs, it is essential to trace the evolution of SPI from its inception. The concept of "diffraction-before-destruction," proposed by Neutze et al. in 2000 [5], brought the feasibility of SPI experiments at XFELs closer to reality. A significant milestone was reached in 2011 with the pioneering work of Seibert et al. [91], who successfully imaged single mimivirus particles (400-450 nm) delivered using a

GDVN combined with an ALS at the Linac Coherent Light Source (LCLS). Later experiments by Hantke et al. in 2014 used the same delivery method for smaller particles (approximately 100 nm), specifically carboxysomes—icosahedral cell organelles from photosynthetic cells [40]. However, the diffraction patterns indicated that the particles were mostly spherical, a consequence of large droplets produced by the GDVN, where non-volatile contaminants in the droplets deposited on the samples. Consequently, ES, which produces much smaller droplet sizes (approximately 150 nm) and more monodisperse samples, was introduced into SPI experiments in combination with the ALS [44]. Repeating the carboxysome experiment using the ES-based system yielded markedly improved diffraction patterns. This success paved the way for testing even smaller particles, such as the tomato bushy stunt virus (approximately 35 nm) and the E. coli 70S ribosome (approximately 20 nm), which also demonstrated successful diffraction patterns. Despite these advancements, further experiments with even smaller particles, like the chaperonin 60 from Escherichia coli (GroEL, approximately 15 nm), encountered significant challenges, including high background noise from scattering by the injection gases and low sample delivery efficiency, complicating the interpretation of the diffraction patterns [27]. These challenges underscore the necessity for improvements in ES-based gas phase injection systems for SPI at XFELs. This section will discuss the limitations of current ES-based systems, focusing on three main challenges: inefficient sample delivery, high background noise, and constraints imposed by the conductivity of the sample solution. Our analysis aims to guide improvements in these systems.

The transmission efficiency of particles through the ES-based injection system is notably low, approximately 5%, primarily due to the inefficient neutralization of charged droplets and the specific geometry of the ES setup. This inefficiency has profound implications for SPI experiments, significantly reducing the dataset of diffraction patterns obtainable, in particular when the sample size decreases [12]. Consequently, this limitation not only diminishes the quality of the final 3D reconstruction but also results in a considerable waste of experimental time and resources.

Moreover, the high background noise from the scattering of carrier gases, such as N_2 and CO_2, further exacerbates these challenges [27]. This noise significantly lowers the signal-to-noise ratio for small light particles, a critical factor for small biological samples. The resultant low-quality diffraction patterns pose substantial hurdles in accurately reconstructing the 3D structure of the sample, further complicating SPI experiments.

An additional limitation stems from the narrow range of sample solution conductivities that can be effectively sprayed using the ES configurations [66]. This constraint impacts the quality and feasibility of SPI experiments, as manipulating the sample solution to achieve optimal conductivity without compromising sample integrity proves

to be a delicate balance. The stability of the ES operation is thus directly tied to the ability to maintain this balance, presenting yet another hurdle for researchers.

2.5 Precision in 3D Printing: The Role of Two-Photon Polymerization

Two-photon polymerization (2PP) is a leading 3D printing technology recognized for producing intricate micro and nanostructures with unmatched precision. It leverages a nonlinear optical process, two-photon absorption (2PA), where two infrared photons simultaneously absorbed by a photopolymerizable resin trigger a polymerization reaction [92]. The technique's distinct advantage is its high localization of polymerization at the laser's focal point due to the quadratic relationship between 2PA and light intensity, enabling the creation of structures beyond the diffraction limits of light.

The core principle of 2PP centers on directing a femtosecond laser beam into a photopolymerizable resin volume [95, 96]. At the beam's focal point, the laser intensity reaches a level sufficient to initiate two-photon absorption, causing the resin to polymerize but only at that specific point, as shown in Figure 2.10. This selective polymerization enables the creation of complex three-dimensional structures by precisely moving the laser's focus through the resin. Mathematically, the rate of two-photon absorption is expressed as:

$$R \propto I^2$$

Here, R represents the absorption rate, and I denotes the laser light's intensity [97].

The Nanoscribe Photonic Professional GT, a 2PP-based 3D printer we utilized for nozzle production, employs a tightly focused femtosecond laser to precisely polymerize photosensitive resin, as illustrated in Figure 2.10. This printer achieves feature sizes down to 200 nm, serving photonics, microfluidics, and biomedical applications well. It integrates advanced optics, precise mechanics, and sophisticated software for nanometer-scale printing accuracy [98].

In microfluidics, 2PP has transformed device fabrication, allowing for complex, precise structures difficult with traditional methods. This includes detailed nozzles, channels, valves, and mixers for unparalleled fluid manipulation [53]. This technology accelerates the transition from rapid prototyping to production, significantly enhancing functionalities such as improved droplet formation and particle delivery in our ES-based systems.

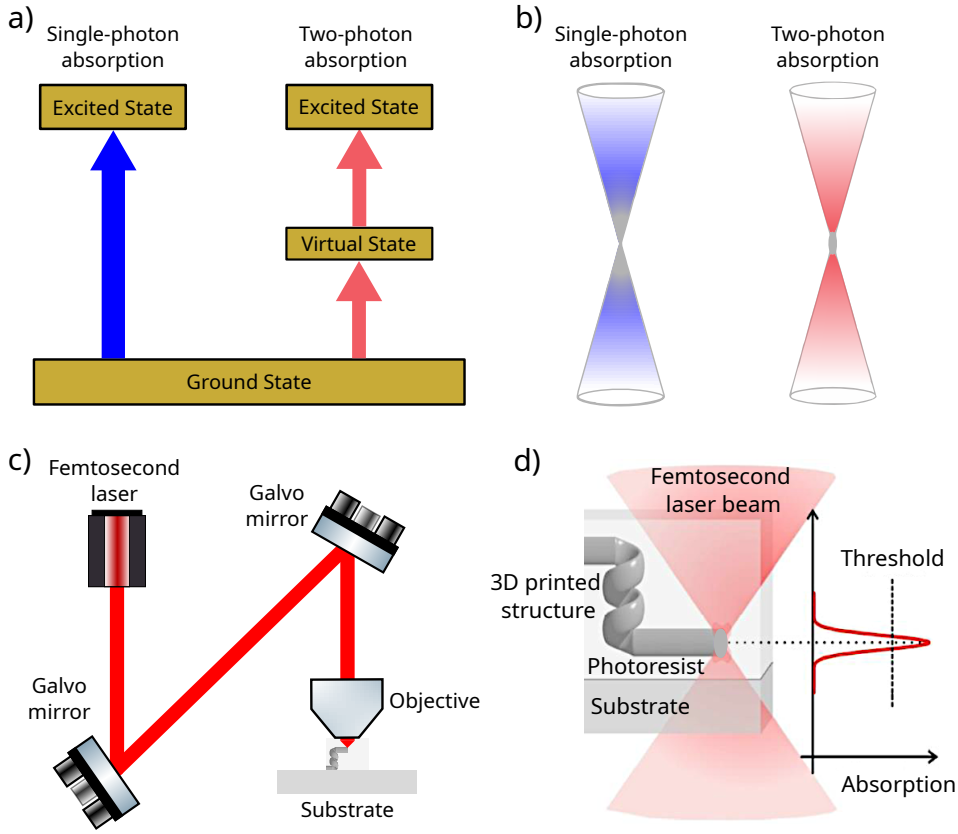

Figure 2.10: Illustration of 3D printing using two-photon polymerization. a) Schematic comparing the two-photon polymerization process with single-photon polymerization. b) Illustration of the excitation volume in two-photon polymerization versus single-photon polymerization. c) Schematic of a 3D printer based on two-photon polymerization. d) Illustration of the printing volume in 2PP where the laser intensity reaches a level sufficient to initiate two-photon absorption, causing the resin to polymerize exclusively at that specific point. (reproduced with permission [93, 94]).

2.6 Optimizing Sample Preparation for ES-based Injection System

A wide variety of samples, from biological specimens to inorganic nanoparticles, are supported by the ES-based injector system [30–39, 42, 43, 99, 100]. To ensure compatibility between the samples and this system, various preparation methods are utilized. These methods help maintain the structural integrity of the samples and prepare them in a suitable medium for spraying. At the heart of these methods is the careful selection of solvents and buffers, which are key to successful sample delivery in ES-based SPI experiments. Fine-tuning these substances is crucial for achieving optimal conditions for sample delivery. This often requires a trial-and-error approach to identify

the most suitable conditions, taking into account several critical factors:

- pH Stability: The pH of a buffer plays a pivotal role in influencing the structure and functionality of a sample, particularly biological samples. Proteins, for instance, exhibit optimal stability and maintain their native structure within specific pH ranges. Deviating from these ranges can lead to denaturation or aggregation, compromising biological activity. For example, proteins are made up of amino acids, many of which have side chains that can be ionized. The ionization state of these side chains is pH-dependent. At certain pH levels, the side chains of acidic (e.g., aspartic acid, glutamic acid) and basic (e.g., lysine, arginine, histidine) amino acids can gain or lose protons. This alters the overall charge of the molecule. This change impacts the electrostatic interactions within the protein and with its surroundings, potentially affecting protein conformation, stability, and interactions with other molecules [101]. Therefore, selecting a buffer that preserves the optimal pH, close to 7.4 for human proteins, is essential for maintaining sample stability and activity.

- Buffer Concentration: The concentration of a buffer can significantly influence the osmolarity of a solution, which, in turn, affects the stability of samples, especially biological ones such as proteins or cells. Osmolarity is defined as the total concentration of solute particles in a solution and plays a pivotal role in preserving the osmotic balance of biological specimens. Inappropriate osmolarity levels, whether excessively high or low, can precipitate protein or induce cell lysis. For instance, biological cells, which are sensitive to osmotic pressure variations in their environment, react distinctively to the osmolarity of the buffer solution. If the osmolarity of the buffer solution is too high, water will osmotically exit cells, causing them to shrink and potentially leading to cellular damage [102]. Conversely, if the osmolarity is too low, water will enter the cells, leading to swelling and possibly causing the cells to burst. Typically, a concentration of 10 mM to 50 mM is used to maintain osmolarity without interfering with the biological activity of the sample.

- Ionic strength: The ionic strength of a buffer significantly influences both the solubility of samples and the strength of electrostatic interactions between molecules, especially in samples involving proteins, nucleic acids, and other biomolecules [103]. This influence manifests through phenomena known as "salting in" and "salting out," where ionic strength modulates biomolecule solubility. During the "salting in" phase, slight to moderate ionic strength increments enhance solubility by mitigating electrostatic repulsion among similarly charged molecules, thus promoting their dissolution in water. Conversely, surpassing a specific ionic strength threshold triggers the "salting out" effect, where

high concentrations of ions compete with the biomolecules for water molecules, reducing solubility and potentially precipitating the biomolecules out of solution. Furthermore, ionic strength directly impacts the Debye length, indicative of the solution's electrostatic screening effect. An increase in ionic strength corresponds to a reduced Debye length, which signifies more effective screening of electrostatic interactions between charged molecules by surrounding ions. Consequently, proper ionic strength adjustment is essential for biomolecule stability, preventing aggregation or precipitation and ensuring that proteins, for instance, retain their soluble and functional state. Common biological experiment buffers like phosphate-buffered saline (PBS), Tris, or HEPES require precise ionic strength adjustments for experimental needs, with the salt choice and concentration (e.g., NaCl, KCl) being crucial for ionic strength control.

- Solubility: The choice of solvents or solvent mixtures also depends on their solubility [104]. For example, polar molecules are often effectively dissolved in polar solvents such as water, methanol, or acetonitrile, whereas non-polar molecules may require non-polar solvents like chloroform or toluene. Polar solvents are particularly useful for dissolving biological molecules, including peptides, proteins, and other polar metabolites. Mixtures of water with organic solvents such as methanol or acetonitrile are common, as they provide a balance between solubility and volatility.

- Metal ions: Metal ions in buffer solutions can greatly affect the stability of biological samples by influencing protein structure, enzymatic activity, nucleic acid integrity, and molecular interactions [102]. Enzymes often need specific metal ions (e.g., Mg^{2+}, Ca^{2+}, Zn^{2+}, Mn^{2+}) as cofactors to function properly. These ions may stabilize the enzyme's active site or directly participate in catalysis. However, unsuitable metal ions can inhibit enzyme activity by competing with essential ions or altering the enzyme's structure. Metal ions also play a critical role in stabilizing protein structures. For instance, calcium ions help maintain the structure of cadherin and selectin, vital for cell adhesion, while zinc ions support the configuration of zinc finger proteins, important in DNA binding and gene expression. Additionally, Mg^{2+} ions are pivotal for nucleic acid stability, neutralizing DNA or RNA's phosphate backbone's negative charges to facilitate the formation of crucial secondary structures like helices and loops.

- Volatility: It is essential that buffers and solvents exhibit sufficient volatility to prevent sample contamination in SPI experiments. As the droplets, generated by ES, traverse toward the interaction chamber, the solvent evaporates, leaving the sample particles behind. Conversely, non-volatile components may fail to evaporate efficiently, adhering to the sample particles [44]. Such adherence

could result in the accumulation of salts or non-volatile residues, potentially contaminating the sample and complicating SPI experiments. Moreover, these non-volatile components could adhere to system surfaces, leading to clogs and thereby hindering system operation and increasing maintenance requirements.

- Surface tension: The surface tension of a liquid is a critical parameter that significantly impacts the operation and efficiency of ES-based sample delivery system in SPI experiments, influencing several aspects of the ES process [99, 100]. At the heart of this process is the formation of the Taylor cone, a phenomenon governed by the balance between electrostatic forces, which aim to disperse the liquid, and the liquid's surface tension, striving to reduce its surface area at the ES's tip. A lower surface tension makes it easier for the electrostatic forces to stretch the liquid into a cone, enabling the emission of a jet from its tip. This process allows for the formation of a sharper cone with a finer tip, conducive to generating smaller droplets. Smaller droplets are advantageous due to their higher surface area-to-volume ratio, which increases the efficiency of solvent evaporation. Conversely, a higher surface tension resists deformation, necessitating higher applied voltages to achieve a similar effect. This may result in a less sharp cone, leading to larger droplets, a higher risk of corona discharge that can collapse the Taylor cone, and an increased likelihood of disruptions, such as pulsations or fluctuations in the cone shape and jet stream. These factors can affect the consistency and reproducibility of the results.

- Conductivity: The conductivity of the solution is a critical factor affecting the stability of the ES process [66, 100]. In this process, a high voltage is applied to the solution to induce a charge on the liquid's surface. Adequate conductivity allows the solution to carry electrical charges efficiently, facilitating an even distribution of charges across the surface of the liquid being sprayed. This even charge distribution is crucial for the formation of a stable Taylor cone. Conversely, low conductivity implies insufficient ions to conduct electricity effectively, resulting in poor charge distribution on the liquid's surface and unstable spray. Additionally, to compensate for low conductivity, higher voltages may be required, increasing the risk of corona discharges that can disrupt the ES process. Higher conductivity enables a more stable jet, as the charges are more uniformly distributed across the liquid's surface, resulting in smaller, more uniform droplets. Although a certain level of conductivity is beneficial, excessively high conductivity can overload the liquid's surface with charge, causing instability in the Taylor cone. It is crucial to ensure that the sample solution's conductivity is within the optimal range for the ES system, specifically between 600 - 2500 μS cm^{-1}, to achieve stable sample delivery.

- Viscosity: The viscosity is another important property of the solutions that can

affect the ES process [104]. Liquids with higher viscosity resist shear forces more, impacting the stability of the Taylor cone. Above a certain viscosity threshold, maintaining a stable spray becomes challenging. This resistance influences droplet size and dispersion as well; higher viscosities often result in larger droplets due to increased resistance to breakup, which is less desirable. Furthermore, viscosity affects the flow rate through the ES system, where higher viscosity may decrease flow rates and increase the risk of capillary clogging.

Despite efforts in selecting the solvents and buffers to achieve optimal conditions, fully ideal circumstances may not always be attainable, necessitating the consideration of compromise solutions. Such compromises might involve accepting semi-stable sample delivery, which, while not optimal, allows for some level of data collection in SPI experiments. Additionally, these compromises could lead to reduced sample stability due to degradation or aggregation. This, in turn, might necessitate more frequent sample maintenance between data collections, further impacting the efficiency and effectiveness of data collection in SPI experiments.

Furthermore, various additives may be incorporated into buffer solutions to enhance the stability of samples, addressing specific stability concerns and improving robustness during experiments. For inorganic nanoparticle samples, these additives help stabilize or passivate nanoparticles to prevent aggregation, enhance solubility, or confer specific surface properties [105–107]. For instance, Polyvinylpyrrolidone (PVP) acts as a stabilizer and dispersant, adsorbing onto nanoparticle surfaces to provide steric stabilization against aggregation. This is especially useful for nanoparticles like silver and gold due to PVP's excellent solubility in water and various organic solvents. Similarly, Polyethylene Glycol (PEG) enhances colloidal stability through steric stabilization. Cetyltrimethylammonium Chloride (CTAC), a cationic surfactant, modifies nanoparticle surface charges, promoting stabilization through electrostatic repulsion. Oleylamine, an organic amine, serves both as a surfactant and stabilizer by forming a monolayer on nanoparticles to prevent oxidation. Trihexyltetradecylphosphonium Bis(trifluoromethylsulfonyl)amide, an ionic liquid, acts as both a solvent and stabilizer, offering electrostatic and steric stabilization. Oleic Acid, an organic acid, also stabilizes nanoparticles by forming a hydrophobic monolayer around them.

For biological samples, these additives play several roles, including protecting against degradation and preserving the native structure and functionality of biomolecules [102]. For instance, reducing agents like Dithiothreitol (DTT) and β-mercaptoethanol prevent protein oxidation by protecting sensitive sulfhydryl groups. This prevention is crucial as oxidation can form improper disulfide bonds, altering protein structure and function. Chelating agents, such as EDTA and EGTA, bind divalent metal ions that could otherwise catalyze biomolecule degradation or cause detrimental interac-

tions affecting molecular conformation. Stabilizing sugars and polyols, like Sucrose and Glycerol, protect against thermal denaturation and aggregation by increasing solution viscosity and reducing molecular mobility. Surfactants and detergents, such as Tween and Triton X-100, maintain membrane protein solubility and prevent aggregation by mimicking the lipid environment or disrupting non-specific protein interactions. The type and concentration of detergent are vital for preserving membrane protein solubility and activity.

2.6.1 Common Solvents, Buffers, and Reference Samples

Common solvents used in ES include water, ethanol, isopropanol, methanol, and acetonitrile [104]. Among these, water is often the primary choice due to its compatibility with a wide range of biological samples. Ethanol is known for its low viscosity and high volatility, as well as its good solvent properties and compatibility with a wide range of inorganic samples. However, organic solvents such as ethanol, isopropanol, methanol, and acetonitrile are frequently used either singly or in combination to adjust the solution properties.

Concurrently, commonly used buffers are categorized into two types: acidic and basic, each serving distinct roles tailored to the nature of the sample and the experimental requirements. Acidic buffers, pivotal for maintaining a lower pH, are crucial in stabilizing certain biomolecules and ensuring optimal charge states during the ES process. These buffers include: Formic Acid, Often utilized in low concentrations, formic acid creates a mildly acidic environment conducive to the stability of proteins and peptides under such conditions [104]. Acetic Acid, Similar in function to formic acid, acetic acid can provide a slightly varied pH range, offering benefits for specific molecules or complexes. Conversely, basic buffers are essential for adjusting conditions to a higher pH value. Among these, Ammonium Acetate (AmAc) is particularly noteworthy. This volatile salt is recognized for its versatility in both positive and negative ion modes of ES. Its volatility is advantageous, leaving minimal residue on the sample. AmAc is especially preferred for compounds sensitive to pH fluctuations, offering a stable buffering capacity without significantly altering the sample's natural state.

To ensure the effective operation of the ES-based system in SPI experiments, we typically begin with well-characterized, stable buffer solutions such as 20 mM AmAc in water or 80 mM AmAc in ethanol. These solutions are selected because their conductivity, viscosity, and surface tension are within the optimal range for ES operation. For calibration and alignment in SPI experiments, the following samples are commonly utilized:

- Sucrose Solutions: These are available in various volume-to-volume concentra-

tions (e.g., 0.5%, 1%, 3%, 5%) dissolved in 20 mM AmAc in water. Chosen for their efficient and stable sample delivery, these solutions have a low density and controllable particle size that mimic biological samples, providing an excellent reference for system alignment. Their simple spherical shape is easily identifiable in diffraction patterns, making them ideal for calibration purposes.

- Gold Nanospheres: These are suspended in 20 mM AmAc in water and are available in different sizes. With their higher density and simple spherical shape, gold nanospheres produce diffraction patterns with a high signal-to-noise ratio, serving as reliable references, particularly for inorganic nanoparticle samples.

- Silver Nanocubes: Available in sizes such as 55 nm or 75 nm side length and suspended in 80 mM AmAc in ethanol, these nanocubes, with their more complex cubic shape and high density, yield high signal-to-noise ratios and produce distinct diffraction patterns. This makes them especially valuable in distinguishing between silver nanocubes and potential contaminants that may form sphere-like shapes.

2.6.2 Nanoparticles to Biomolecules: Electrospray Applications

ES is a versatile technique employed for analyzing a broad spectrum of samples, including biological ones such as proteins, peptides, nucleic acids, and inorganic nanoparticles like polymers and metal nanoparticles. Common challenges with inorganic samples include rapid aggregation or sedimentation. Nevertheless, with careful sample preparation and repeated optimization, ES has been successfully applied in SPI experiments at European XFEL using inorganic samples such as cesium lead bromide ($CsPbBr_3$) nanocrystals, EuXFEL proposal number 4417. These are used to elucidate polaron formation mechanisms in perovskite quantum dots, known for their superior optoelectronic properties. The nanocrystals, ranging from 5 to 12 nm in size, demonstrate exceptional photon collection and photoluminescence efficiencies—key for observing optically induced polaronic deformations. They were dispersed in a toluene solution at a concentration of 10^{14} particles/mL. To ensure the stability of the CsPbBr3 nanocrystals within the solution, a combination of oleic acid and oleamine was employed as a coating to prevent aggregation. Additionally, an ionic liquid, trihexyltetradecylphosphonium bis(trifluoromethylsulfonyl)amide, was integrated into the solution to enhance stability. Despite the sample's relatively low conductivity, measured at 30 to 60 μS/cm, this preparation allowed for semi-stable sample delivery, ensuring successful data acquisition during the experiment.

To investigate single-particle incoherent diffractive imaging techniques, a method that

utilizes the transient coherence of X-ray fluorescence for nanometer-resolution imaging of atomic structures, copper nanocubes were selected due to their shape and notable fluorescence properties, EuXFEL proposal number 5476. To optimize conditions for sample delivery through an ES-based injector, several trials were conducted to determine the ideal concentration of AmAc and the appropriate stabilizer for the sample solution. Ultimately, the copper nanocubes were successfully sprayed using a solution containing 12 mM AmAc and PEG as a stabilizer, ensuring the sample's integrity throughout the spraying process.

To explore the strong resonances in late 3d transition metals through element-specific diffractive imaging, samples of iron oxide cores with silica shells and silver cores with nickel shells were prepared in aqueous solutions, EuXFEL proposal number 2654. During the sample preparation for delivery via ES-based aerosol injection, a stabilization step involving PVP was employed to enhance nanoparticle stability. However, this method resulted in stable operation for the iron oxide nanoparticles with silica shells, whereas the silver cubes with nickel coatings sedimented rapidly. To resolve this issue, the PVP stabilizer was replaced with PEG, which significantly improved the stability of the samples.

For biological samples, fragmentation or degradation often poses the significant challenges. However, careful sample preparation and iterative refinement have enabled the successful application of ES-based aerosol injection systems in SPI experiments at the European XFEL. One such example is the tobacco mosaic virus (TMV), a rod-shaped virus characterized by a regular helical array of identical protein subunits with a single RNA molecule embedded within, forming a helix, EuXFEL proposal number 4462. Due to its basic rod shape, TMV was utilized in optical-pump FEL-probe studies to demonstrate the controlled alignment of (bio-) nanoparticles using strong lasers. These studies also aimed to provide a systematic understanding of how alignment reduces orientational uncertainty in SPI experiment reconstructions. To optimize sample delivery for this experiment, various concentrations of AmAc were tested. Ultimately, a 30 mM AmAc solution proved most stable for both the TMV sample and the delivery system.

To obtain the first high-resolution 3D structure of a single protein using low background high-repetition rate 3D X-ray imaging, several candidate samples were considered: GroEL from E. coli, Photosystem Complex I, and E. coli 70S ribosomes, EuXFEL proposal number 4098. The GroEL complex, part of the chaperonin family of molecular chaperones, is prevalent in many bacteria. It was expressed in an E. coli overproducing strain and selected for its role in understanding protein folding. Photosystem Complex I, a substantial membrane protein complex, was chosen for its key function in photosynthesis. The E. coli 70S ribosome, isolated from Escherichia coli strain K-12, was selected due to its involvement in cellular translation mecha-

nisms. For optimal sample delivery in this experiment, it was determined that both the GroEL complex and Photosystem Complex I exhibit stable injection conditions in 20 mM AmAc buffer. The E. coli 70S ribosomes, however, were suspended in the same buffer, resulting in two distinct peaks on the SMPS, corresponding to sizes of 18 and 14 nm, respectively. The combined volume of these peaks was measured at 20.5 nm, which aligns with the expected full size of the ribosome, indicating potential sample fragmentation. To enhance stability, the 70S ribosomes were subsequently cross-linked using glutaraldehyde in a 20 mM AmAc solution, rendering the sample more stable.

To investigate biological vesicles, synaptic vesicles (SVs) and unilamellar lipid vesicles (LVs) were chosen for their role in neurotransmitter storage and release, and as models for membrane dynamics, respectively [41]. SVs, which are found in neuron synapses, facilitate the rapid transmission of signals through the release of neurotransmitters into the synaptic cleft. LVs, on the other hand, are simpler systems that consist of a single lipid bilayer, making them ideal for studying the fundamental properties of lipid membranes and their interactions with various molecules. These vesicles are approximately 20 nm in radius. To optimize sample delivery, we tested various combinations of buffers and additives. For LVs, a solution containing 10 mM LVs with 1 mM calcium chloride in water proved stable, achieving a consistent hit rate of approximately 0.5%. For SVs, two solutions were stable and were delivered: SVs in 20 mM AmAc in water, and SVs with 6 μM Synapsin in 20 mM AmAc in water.

Chapter 3

Enhancing Electrospray Ionization Efficiency for Particle Transmission Through an Aerodynamic Lens Stack

This chapter is based on the publication: **Rafie-Zinedine, S.**, Varma Yenupuri, T., Worbs, L., Maia, F. R. N. C., Heymann, M., Schulz, J., & Bielecki, J., "Enhancing Electrospray Ionization Efficiency for Particle Transmission through an Aerodynamic Lens Stack", *J. Synchrotron Rad.* **31**, 222-232, (2024), [61]. Reproduced with permission from the Journal of Synchrotron Radiation.

Contribution

I contributed to the conception of the idea, development and construction of the setup, data recording and data analysis, preparation of figures for the manuscript, writing of the initial draft, and revising the manuscript in collaboration with all co-authors.

Abstract

We investigate the performance of the electrospray aerosol generator at the European X-ray Free Electron Laser (EuXFEL). This generator is, together with an aerodynamic lens stack that transports the particles into the X-ray interaction vacuum chamber, the main way to deliver particles for single particle coherent diffractive imaging (SPI) experiments at the EuXFEL. For these experiments to be successful, it is necessary to achieve high transmission of particles from solution into the vacuum interaction region. The particle transmission is highly dependent on efficient neutralization of the charged aerosol generated by the electrospray mechanism as well as the geometry in the vicinity of the Taylor cone. We report absolute particle transmission values for different neutralizers and geometries while keeping the conditions suitable for SPI experiments. Our findings reveal that a VUV ionizer demonstrates a transmission efficiency approximately 7 times greater than the previously used soft x-ray ionizer. Combined with an optimized orifice size on the counter electrode, we achieve $> 40\%$ particle transmission from solution into the X-ray interaction region. These findings offer valuable insights for optimizing electrospray aerosol generator configurations and data rates for SPI experiments.

3.1 Introduction

Methods for delivering a dense beam of single particles to the interaction region of a Free Electron Laser (FEL) are of significant interest in uncovering the structural properties of small nanometer-scale particles. Commonly employed methods for achieving this include liquid jet injection and gas phase injection. Among these methods, gas phase injection through an Aerodynamic Lens Stack (ALS) offers several advantages. It provides increased scattering contrast, reduced background scattering, and the ability to collect data at high rates. In particular, aerosolized particle delivery provides an opportunity to harness the unique capabilities of the European XFEL (EuXFEL), which emits X-ray 'trains' at 10 Hz, each containing up to 2700 pulses separated by 220 ns [14]. The high repetition rate allows for rapid acquisition of large data sets, provided that the sample delivery system is compatible with the XFEL pulse structure. Aerosol injection can meet the latter requirement, where gas-phase particles can achieve velocities ranging from tens to hundreds of meters per second, thereby preventing multiple exposures from subsequent pulses [44, 108].

There are several aerosolization methods available for gas phase injection through an ALS, including Electrospray (ES), atomizers, Gas Dynamic Virtual Nozzle (GDVN), and others. However, ES stands out among these methods due to its capability to

produce smaller droplets, which results in virtually contaminant-free sample delivery [44]. ES is a powerful technique that uses electrical forces to atomize liquids, transforming them into nanometer to micrometer-sized droplets. This process is accomplished by overcoming the liquid surface tension with electric forces as the liquid flows through a capillary nozzle. There are several forms of ES, including 'grinded' single-capillary, dual-capillary, and tri-nozzle ES, with single-capillary ES being the most extensively researched and documented [66, 71, 72].

ES systems typically consist of a spray nozzle positioned opposite a plate, with or without an orifice at the center. By applying an electric field between the nozzle and the plate, a cone-jet meniscus, called Taylor cone, forms when the liquid surface tension is counterbalanced by the electric force. The liquid jet undergoes Rayleigh breakup into a mono-disperse droplet stream, which has gained significant interest for its potential applications [109] such as drug delivery [67], nanoparticle material synthesis [69], thin-film deposition, and particle encapsulation [68], surface coating, agricultural treatments, fuel spraying, ink-jet printers, and colloid micro-thrusters [70].

Our primary focus in this study is ES's application as a particle delivery system for Single Particle Imaging (SPI) experiments at free-electron X-ray laser facilities[44, 87]. In these experiments, shown schematically in Figure 3.1 the droplet stream from the ES is allowed to evaporate in order to transfer the sample particles from solution into the gas-phase. Subsequently, the particles pass through an ALS [110, 111], described in detail in ref. [108], which creates a focused particle beam that intersects the pulsed X-ray beam. Each X-ray pulse contains enough photons to produce a diffraction pattern of a single particle, while the pulse duration of ≈10 fs has been considered short enough to enable 'diffraction-before-destruction'[5]. The information in each pattern can be used to obtain 2D, or in some cases pseudo-3D, information about individual particles in an ensemble. If the particles are reproducible, it is also possible to merge the individual patterns into a 3D volume in reciprocal space. After phase retrieval, one can obtain the full 3D structural information about the particle. Numerous such experiments have been performed at free electron lasers on cells [29], viruses [30–39], cell organelles [40], proteins [27], and inorganic nano-particles [42, 43]. Despite the successful imaging experiments, concerns persist regarding particle transmission efficiency, especially as the sample size decreases[12].

Although substantial research has explored droplet aerosolization in ES processes [76, 77, 112], further study is necessary to optimize particle neutralization and transmission at various stages. Initially, the spray is narrow, but the Coulomb repulsion of highly charged droplets causes the spray to widen and increases the likelihood of deposition on the counter electrode. To transport electrospray-generated particles through a carrier gas flow, it is essential to neutralize the charged particles. This can be ac-

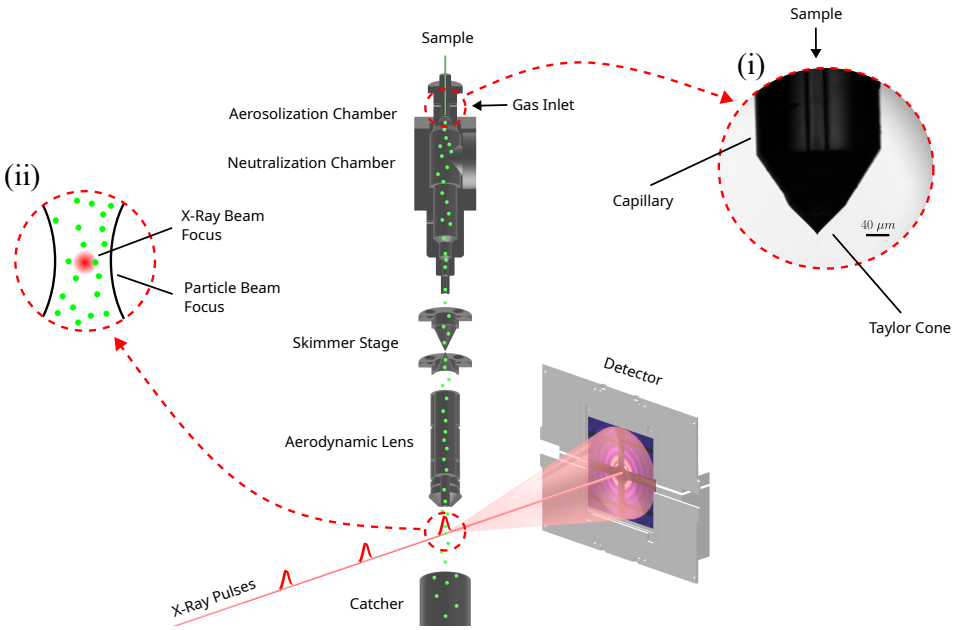

Figure 3.1: A schematic diagram detailing the experimental setup of an electrospray-based aerosol injector used at the European X-ray Free Electron Laser (EuXFEL). The injector includes the ES process depicted at the top, where the sample is aerosolized. The aerosol beam then passes through the skimmer stages and the aerodynamic lens before reaching the interaction chamber, where it is hit by the XFEL beam. The XFEL pulses are scattered off particles in the aerosol beam to produce diffraction patterns on the detector. Insets illustrate a typical Taylor cone (i), here injecting sliver nano-cube in 80 mM ammonium acetate dissolved in ethanol. Note how the X-ray beam focus is significantly smaller than particle beam focus (ii).

complished by exposing the particles to an environment with ions produced using methods such as radioactive sources, corona discharge, and VUV/soft X-ray irradiation [66, 83, 113, 114]. Each of these techniques presents its own challenges and limitations, such as strict regulations for radioactive materials, high voltage power supplies and potential ozone production for corona discharge, and complicated safety regulations for operating soft X-ray ionizers. VUV radiation sources, in contrast, offer an accessible, safe, and efficient alternative for bipolar ion generation. In comparison to other methods, VUV sources are easily purchased, operated, and integrated into various applications. Their compact size and portability make them an ideal candidate for particle charge reduction.

In a previous study on electrospray transmission efficiency by Fu *et al*[114] it was highlighted that the highly charged nature of particles produced by ES leads to significant particle loss at the counter electrode orifice plate due to Coulombic repulsion between the highly charged particles [114]. It was found that the electrospray transmission could be improved by increasing either the bi-polar charge density from the neutralizer, the carrier gas flow, and/or the orifice diameter in the counter electrode. Thus,

we primarily optimized the performance of our sample delivery system by varying the types of ionizers (VUV, soft X-ray, and ^{210}Po) as well as the geometry of the ES setup. However, the limitations on gas flow rate for single-particle imaging made it difficult to explore higher rates as in prior studies.

Utilizing advancements in Two-Photon Polymerization, a cutting-edge technique for creating intricate 3D fluidic devices with submicron accuracy, can significantly improve microfluidic nozzle design. This innovative approach has the potential to transform the development and production of microfluidic nozzles, resulting in enhanced performance, miniaturization, and customization possibilities [46, 53]. Employing this technique, tailored microfluidic nozzles can be designed to generate two Taylor cones simultaneously. Using this technique, we designed a custom 'twin nozzle' capable of producing dual Taylor cones. We tested it against a grinded single nozzle to enhance particle production and delivery. The results have implications for XFEL single particle imaging and future injector development.

3.2 Experimental Setup And Methods

3.2.1 Configurations of Electrospray Aerosol Generator

Figure 3.2 illustrates the design of an ES aerosol generator incorporating a VUV ionizer with emission sharply peaked at $\lambda = 155$ nm. The generator is composed of two primary chambers: the aerosolization and neutralization chambers, which are divided by an orifice disk plate. A grinded single glass capillary featuring an inner diameter (ID) of $40\,\mu\mathrm{m}$ and an outer diameter (OD) of $360\,\mu\mathrm{m}$ serves as the spray nozzle in the aerosolization chamber. The sample reservoir is biased at a positive high voltage, while the orifice plate, aerosolization chamber, and neutralization chamber are electrically grounded. The distance between the capillary tip and the grounded orifice plate is kept constant at around 1 mm. N_2 mixed with CO_2 to prevent corona discharge formation was used as the particle carrier gas. Mass flow controllers (Bronkhorst model F-201CV) independently control the two gas flow rates. A differential pressure (ΔP) meter (Bronkhorst model P-506C) coupled with Direct-operated control valves (Bronkhorst model F-001) regulates ΔP across the capillary to control the liquid flow rate. An optical system, including a fiber coupled LED light source, infinity-corrected objectives (5X Mitutoyo Plan Apo f=200), tube lens (Thorlabs TTL200-A), and a CCD camera (Basler acA2440-20gm) enables high-resolution observation of the Taylor cone in the aerosolization chamber (Figure 3.1). The neutralization chamber includes a cylindrical interaction region measuring $25.2\,\mathrm{mm}$ in diameter, which facilitates the interaction between ionizer radiation and the particle beam along with its carrier gas.

Five distinct configurations of the ES aerosol generator were tested and compared in this study, including four configurations for optimizing particle transmission efficiency and one for enhancing particle production. The emitted droplet sizes were characterized previously[53]. The baseline configuration is a single electrospray capillary, $0.5\,\mathrm{mm}$ counter electrode orifice, N_2 volumetric flow rate of $1\,\mathrm{L/min}$, CO_2 volumetric flow rate of $0.3\,\mathrm{L/min}$, and deuterium-based VUV lamp as neutralizer (Hamamatsu L12542) positioned at a 90-degree angle relative to the particle beam (Figure 3.4a). The emission spans wavelengths from $115\,\mathrm{nm}$ to $400\,\mathrm{nm}$. The second configuration (Figure 3.4b), replaces the neutralizer with a soft X-ray source (Hamamatsu L12645) whose emission peaks at around 5 keV. An additional spacer of $36\,\mathrm{mm}$ between the orifice plate and neutralization chamber is included in this configuration to prevent X-ray photons from discharging the Taylor cone directly. The third configuration mirrors the baseline configuration, but with a negatively biased electrode at the end of the neutralization chamber intended to pull positively charged droplets away from the orifice disc (Figure 3.5a). The fourth configuration has a larger $1\,\mathrm{mm}$ orifice diameter (Figure 3.6a). Finally, the fifth configuration operates with a 3D-printed twin nozzle capable of producing two Taylor cones simultaneously (Figure 3.7b).

In the data collection process we alternated between different electrospray configurations to ensure reproducibility of our results and we ensured that the Taylor cone remained stable and consistent across all configurations. The gas flow rate was set to the maximum level appropriate for SPI experiments, taking into account gas mass flow constraints for safe X-ray detector operation. Lower gas flow rates resulted in reduced transmission efficiency and was not investigated further.

The electrospray was operated using a capillary with fixed inner diameter $D = 40\,\mu\mathrm{m}$ and length $L = 30\,\mathrm{cm}$. A stable cone-jet mode was maintained for all tests by adjusting the voltage bias relative to the counter electrode. The CO_2 flow rate was fixed at $0.3\,\mathrm{L/min}$. The sample flow rate Q was controlled between $433\,\mathrm{nL/min}$ and $866\,\mathrm{nL/min}$, respectively by varying ΔP according to the Hagen-Poiseuille equation:

$$Q = \frac{\pi (D/2)^4 \Delta P}{8 \eta L} \tag{3.1}$$

where η is the viscosity of the fluid.

The twin nozzle was designed using Siemens' NX software, featuring two capillary inlets compatible with $360\,\mu\mathrm{m}$ OD fused silica capillaries and dual outlets (Figures 3.7). The design was exported in STL format. Print-job instructions, or GWL files, were generated using Nanoscribe's DeScribe software. To enhance structural stability, we used a solid-volume printing strategy with $1\,\mu\mathrm{m}$ slicing and $0.5\,\mu\mathrm{m}$ hatching. Printing was conducted on the Nanoscribe Photonic Professional GT, using IP-S photoresist.

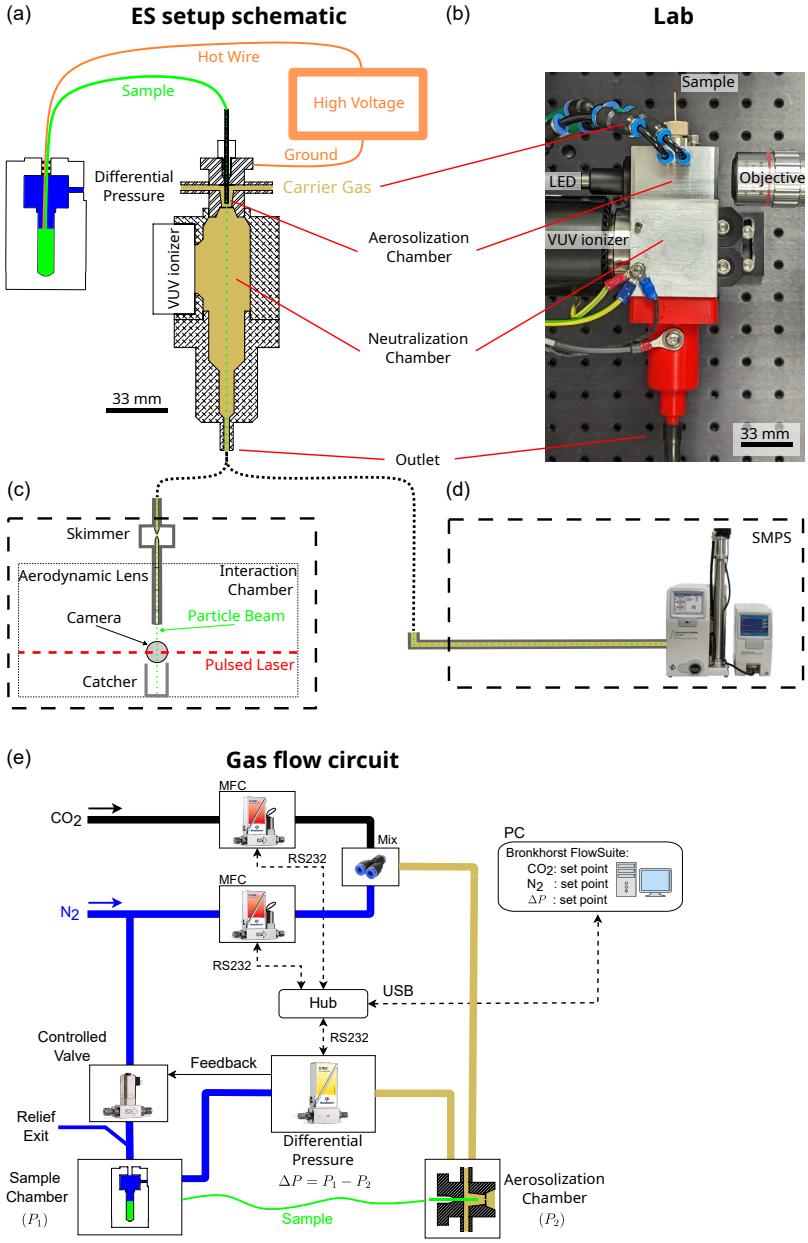

Figure 3.2: A schematic diagram of the experimental setup used to measure particle transmission efficiency. (a) Schematic diagram of the ES setup, in which the sample is aerosolized by forming a Taylor cone. The aerosol is then carried to the neutralization chamber, where it is neutralized by a VUV ionizer before exiting either through a Rayleigh scattering setup or an SMPS setup. (b) A layout of the ES setup as arranged in the laboratory. (c) Rayleigh scattering setup, which comprises double skimmer stages that remove excess gas and an aerodynamic lens that focuses the particle beam before passing through the interaction chamber and being detected by a pulsed laser beam. (d) SMPS setup, which uses a series of differential mobility analyzers and a condensation particle counter to analyze the sample. (e) Schematic of the gas flow circuit, which incorporates gas flow meters, differential pressure, and valves to regulate the flow rate of the sample and carrier gases.

Post-printing, the device was immersed in propylene glycol methyl ether acetate (PGMEA) for 1-2 days to remove uncured material. After this development phase, the devices were rinsed in isopropanol twice for 30 minutes each time and then air-dried on a cleanroom cloth. Assembly was done on a polydimethylsiloxane (PDMS) sheet and observed under an optical microscope. Two 360 µm OD fused silica capillaries

were inserted into the inlets and secured with 5-minute epoxy (from Devcon). These were routed through hollow 1/16-inch OD stainless-steel tubing (IDEX U-145, ID 0.046 inches) and affixed in place. The 3D model of the twin nozzle is publicly accessible and can be downloaded from the following GitHub repository: `https://github.com/safirafie/ESDesign`.

3.2.2 Characterization and Sample Delivery Setup

The ES aerosol generator's characterization was conducted using a Scanning Mobility Particle Sizer (SMPS) setup (TSI 3082 Electrostatic classifier, TSI 3788 N-WCPC, TSI, Shoreview, MN), and a Rayleigh-scattering setup [108] (Figure 3.2). For each measurement, the generation system's outlet was initially connected to the SMPS setup to record size distribution spectra (Figure 3.3a). Subsequently, it was connected to the Rayleigh-scattering setup to image particles reaching the interaction chamber (Figure 3.3b). Then, the particle transmission efficiency was calculated for each configuration.

In addition to particle losses from the electrospray generator, particles can potentially

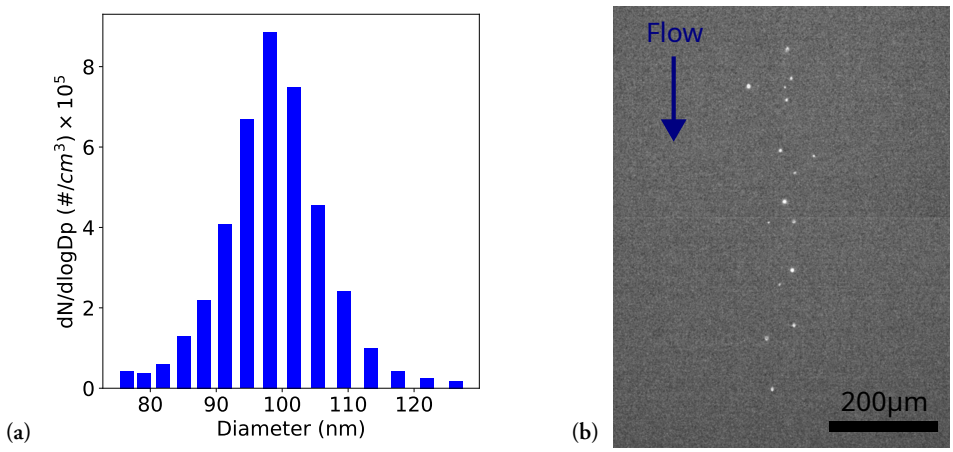

Figure 3.3: Characterization methods using the baseline configuration with sliver nano-cubes in ethanol buffer. (a) Particle distribution of 75 nm-side length silver nanocubes measured by SMPS, showing diagonal length. (b) A frame from the Rayleigh scattering setup showing particle flow into the interaction chamber.

be lost in the two skimmer stages as well as at the orifices inside the aerodynamic lens. To account for these losses, we performed Rayleigh scattering measurements to measure the absolute particle transmission through the whole sample delivery system. The particles exit the aerodynamic lens into a vacuum chamber at approximately $1 \times 10^{-4}\,\mathrm{mbar}$ where they intersect a λ=532 nm double-pulsed Nd:YAG laser producing 6.5 ns long pulses each with 100 mJ pulse energy. A plano-convex lens with a $150\,\mathrm{mm}$ focal length focused the laser beam to a $100\,\mu\mathrm{m}$ Full Width at Half Maximum (FWHM) spot at the intersection point with the particle beam. Scattering from aerosol particles was imaged with a microscope situated outside the vacuum chamber, comprised of an infinity-corrected objective lens, zoom lens, and scientific CMOS camera (Zyla 4.2 sCMOS).

Particle velocities $v = L/\tau$ were measured by illuminating each particle twice, with time separation τ, resulting in two particle detections separated by a distance L within the same camera exposure. Images obtained from the Rayleigh scattering were analyzed using an open-source Python code (https://github.com/safirafie /SPCounting) which calculates v, and position x, y for each detected particle.

Particle transmission, T was calculated as the ratio between the flux of particles exiting the aerodynamic lens to the theoretical flux generated by the electrospray:

$$T = \frac{v\mu}{\rho Q}, \tag{3.2}$$

where μ is the linear density of particles detected with Rayleigh scattering and ρ is the particle concentration in solution [108].

The sample utilized in this study was a commercial silver nano-cube with a side length of $75\,\mathrm{nm}$. The particles were suspended in an ethanol-based $80\,\mathrm{mM}$ ammonium acetate buffer at a concentration $\rho = 1.9E + 10$/ml.

3.3 Results And Discussion

3.3.1 Effects of Different Ionizers

We investigated the impact of two distinct ionization techniques on particle transmission efficiency in the ES process: the VUV ionizer (baseline configuration), as illustrated in Figure 3.4a, and the X-ray ionizer, as depicted in Figure 3.4b. In the absence of an ionizer, the electrospray process generates positively charged particles that are influenced by the electric field. Consequently, these particles tend to accumulate on grounded surfaces, such as the faces of the orifice plate and the internal surface

of the neutralization chamber. The accumulation of charged particles on these surfaces can lead to nearly complete losses in particle transmission, severely reducing the efficiency of the electrospray system.

Everything else being equal, the VUV ionizer configuration delivers approximately 7 times more particles than using the X-ray ionizer as measured by both Rayleigh scattering and SMPS (Figures 3.4c and 3.4d). Considering the calculated particle velocity of $28\,\mathrm{m\,s^{-1}}$, we obtain 35 % and 5 % transmission efficiency with the VUV and X-ray setup respectively.

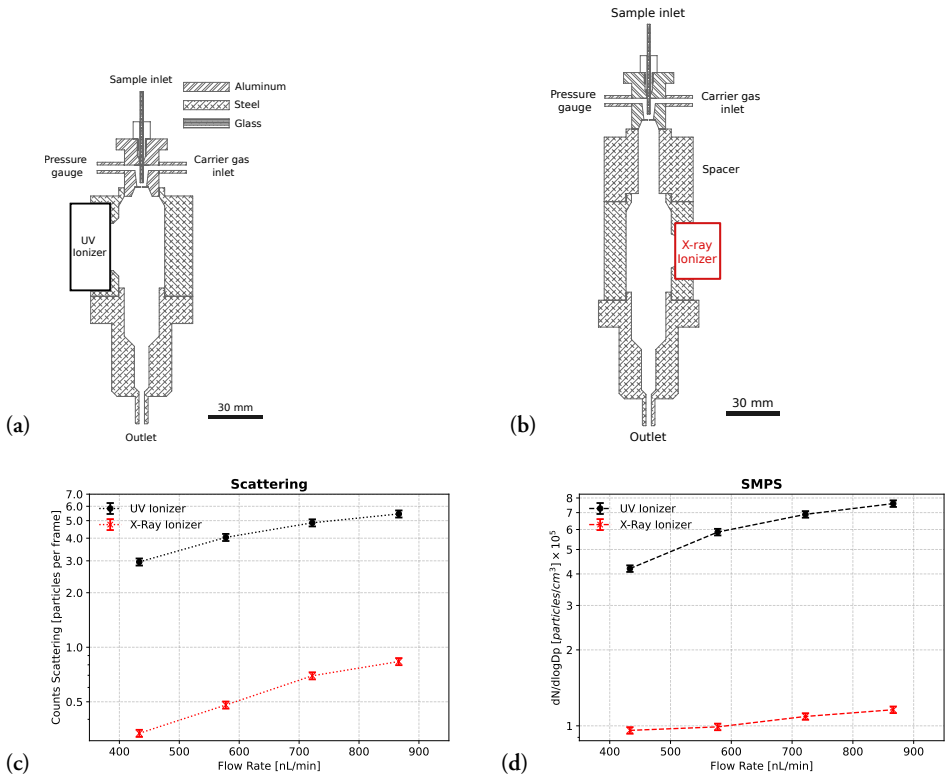

Figure 3.4: A comparison of the particle transmission efficiency in ES using X-ray and VUV ionizers for different sample flow rates. (a) and (b) schematic setup of the VUV and X-ray ionizers, respectively. (c) and (d) the particle counts in each of these setups were measured using Rayleigh scattering and SMPS, respectively. The results show that the VUV ionizer has higher particle transmission compared to the X-ray ionizer.

We mainly attribute the increased particle transmission to the fact that VUV photons are completely absorbed by the carrier gas in the direct vicinity of the emission window. In contrast, a majority of the X-ray photons do not interact with the carrier gas inside the neutralization chamber[115]. This leads to a higher number of produced charges, and hence more efficient neutralization, with the VUV source. For the same reason, the VUV source can be placed closer to the Taylor cone without disturbing

its operation, leading to a larger concentration of neutralizing charges close to the counter electrode orifice plate.

Another commonly used ionizer in electrospray applications is radioactive ^{210}Po α particle source. We installed a commercial ^{210}Po ionizer in a similar configuration to the baseline configuration. We found that the ^{210}Po ionizer outperformed the X-ray ionizer by approximately a factor of 3. However, it underperformed when compared to the VUV ionizer, by approximately a factor of 2.4.

3.3.2 Effects of Using An Auxiliary Electric Field

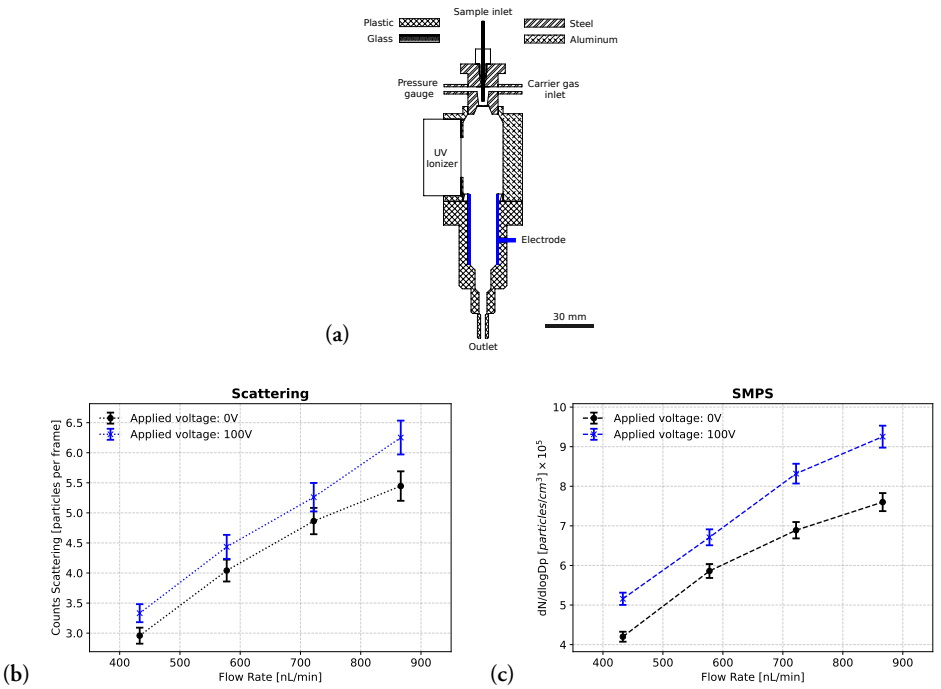

Figure 3.5: Electrospray transmission efficiency using a VUV ionizer with an auxiliary electrode operating at $0\,\mathrm{V}$ or $-100\,\mathrm{V}$. (a) Schematic of the setup with the opposing electrode highlighted in blue. Particle counts were measured with (b) the Rayleigh scattering setup or (c) SMPS. Applying $-100\,\mathrm{V}$ on the opposite electrode increased particle transmission marginally.

We hypothesized that the presence of the auxiliary electric field can assist in attracting positively charged particles away from the counter electrode (Figure 3.5). Applying $-100\,\mathrm{V}$ to the electrode resulted in an approximate increase of $11\,\%$ in particle transmission. At $-50\,\mathrm{V}$, $-200\,\mathrm{V}$, $-500\,\mathrm{V}$, and $-1000\,\mathrm{V}$ the transmission efficiency declined. For the circular electrode used in this study, there is an optimal electric field strength, which may arise from insufficient residence times in the ionization chamber or from radial components of the electric field.

3.3.3 Effects of Orifice Diameter

Particle transmission with orifice plates of $0.5\,\mathrm{mm}$, $1\,\mathrm{mm}$, and $2\,\mathrm{mm}$ in diameter were compared (Figure 3.6a). A $1\,\mathrm{mm}$ orifice plate gave approximately $17\,\%$ more particles compared to the $0.5\,\mathrm{mm}$ baseline configuration (Figure 3.6b), which translates to $41\,\%$ transmission efficiency. This is in agreement with the previous study by Fu *et al* [114], which also showed an improvement in transmission efficiency with the use of larger orifice sizes. However, in contrast a 2 mm orifice plate could not support a stable Taylor cone with our geometry and gas flow rates suitable for SPI experiments.

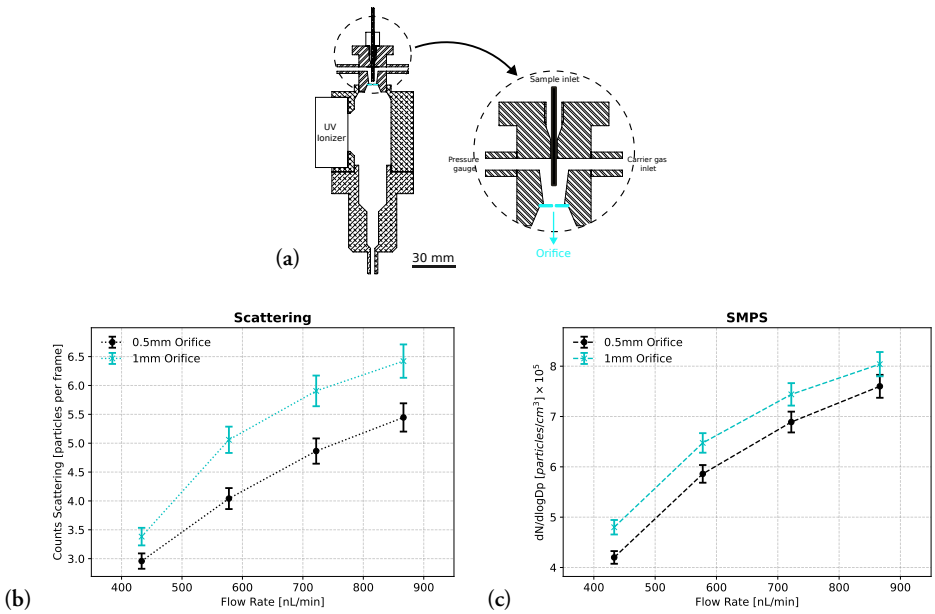

Figure 3.6: Particle transmission efficiency in ES using a VUV ionizer with $0.5\,\mathrm{mm}$ and $1\,\mathrm{mm}$ diameter orifices. (a) schematic setup of the VUV ionizer, with the orifice highlighted in cyan. (b) and (c) the particle counts in each of these setups were measured using Rayleigh scattering and SMPS, respectively.

3.3.4 Effects of Multi-Taylor Cone

We designed a 3D-printed nozzle 'twin nozzle' designed to generate dual Taylor cones in an attempt to increase the total number of transmitted particles compared to the single-capillary emitter (Figures 3.7). Particle delivery was approximately $28\,\%$ higher in comparison to the case where the grinded nozzle was used. Although the multi-Taylor cone configuration increased the number of particles delivered into the interaction chamber, the overall transmission efficiency was measured at $22\,\%$, which is significantly lower than the baseline efficiency. Optical imaging showed that the two

cones were not aligned with the orifice in the counter plate, resulting in a non-optimal angle and an extended travel distance for the particles from the cones to the orifice exit.

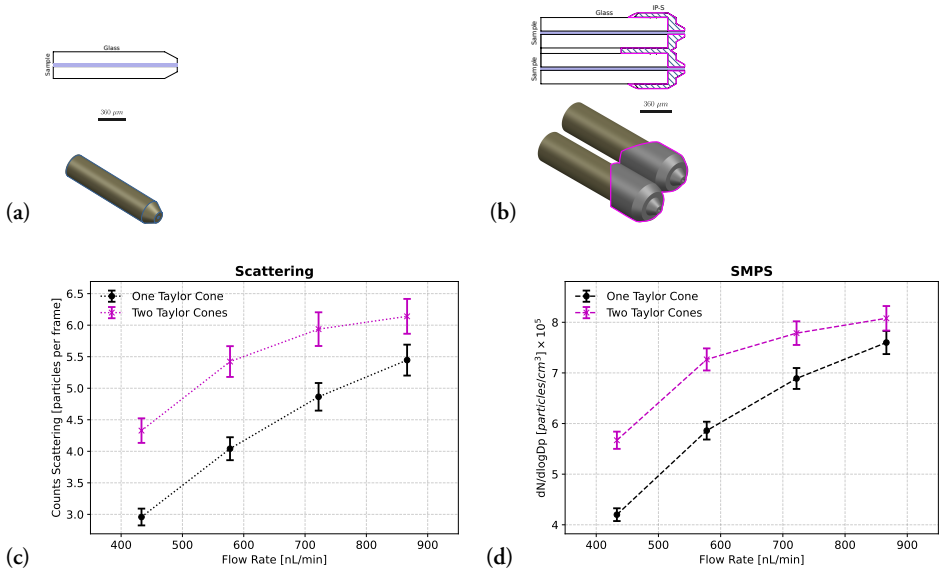

Figure 3.7: Particle transmission efficiency of ES using a VUV ionizer with different nozzle geometries: a grinded capillary that produces a single Taylor cone, and a 3D-printed 'twin nozzle' featuring two separate openings, each generating its own Taylor cone. (a) Schematic of the ground nozzle. (b) Schematic of the twin nozzle with dual openings. (c) Particle counts using Rayleigh scattering setup. (d) Particle counts using SMPS.

3.3.5 Comparison of Particle Transmission Efficiency

A comparison of the transmission efficiencies, calculated as the flow rate average, for all investigated configurations is shown in Figure 3.8. No significant correlation between transmission efficiency and sample flow rate was found. It is important to note that our ES aerosol generator is not the only source of particle losses in the aerosol sample delivery system. Particle losses can also occur in the two nozzle/skimmer stages and on the orifices used as aerodynamic lenses. This is especially true for lighter particles such as proteins or viruses, which closely follow the gas carrier streamlines. For such particles, Rayleigh scattering measurements require a tightly focused laser beam. On the other hand, the aerodynamic focusing is decreased, leading to a particle beam much larger than the required laser beam size. Thus, total transmission measurements become considerably more challenging with decreasing sample size.

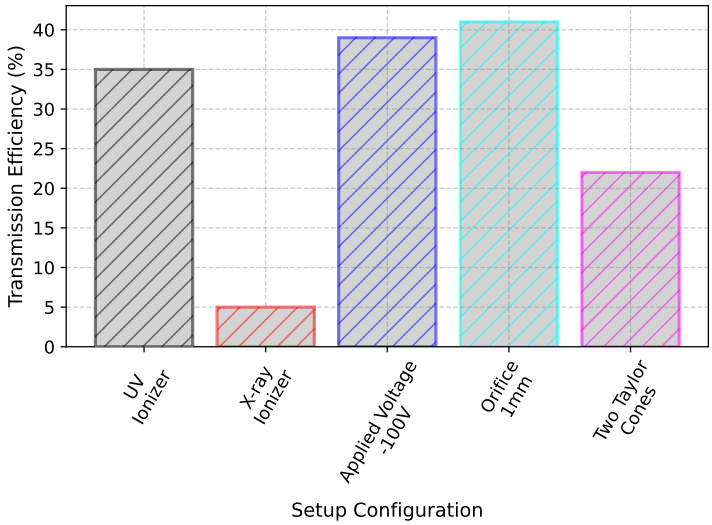

Figure 3.8: A comparison of particle transmission efficiency for various ES configurations demonstrates the influence of different factors such as ionizer type, orifice plate size, the presence of an additional auxiliary electric field, and the production of dual Taylor cones.

3.4 Conclusion

To improve single particle imaging experiments at FELs, five distinct aerosol sample delivery configurations were systematically compared for their transmission efficiency. Rayleigh scattering and SMPS results were consistent in quantifying the effect of each configuration. Most importantly, VUV ionization increased the particle transmission by a factor of 7 relative to X-ray ionization. An auxiliary electric field, or a larger orifice diameter of 1 mm each had a relatively minor positive effect on particle transmission. Employing a 3D-printed twin-nozzle generating two Taylor cones considerably improved particle number, while total transmission decreased. This highlights the potential of exploring innovative nozzle designs to improve overall performance.

Further studies can focus on investigating additional parameters that may influence the performance of ES particle generation systems. These may include electric field strength and distribution, different electrode configurations, and aerosolization chamber designs. Improved neutralization may be achieved with additional VUV ionizers, or refined ionizer geometry, in the neutralization chamber. While we achieved particle transmissions only a factor 2.5 away from ideal 100%, measuring and optimizing transmission for smaller ($<$20 nm) and lighter particles remains an unmet need for single particle imaging at free electron lasers.

Chapter 4

Helium-Electrospray Improves Sample Delivery in X-ray Single-Particle Imaging Experiments

This chapter is based on the publication: Varma Yenupuri, T.†, **Rafie-Zinedine, S.**†, Worbs, Heymann, M., Schulz, J. Bielecki, J., L., & Maia, F. R. N. C., "Helium-electrospray improves sample delivery in X-ray single-particle imaging experiments", *Scientific Reports*, **14**, 4401, (2024), Springer Nature [116]. Reproduced with permission from the Springer Nature.

† These authors contributed equally.

Contribution

I contributed to the development and construction of the instruments, demonstrated the initial proof of concept, conducted the numerical simulations, prepared figures for the manuscript, and co-wrote the manuscript with all authors.

Abstract

Imaging the structure and observing the dynamics of isolated proteins using single-particle X-ray diffractive imaging (SPI) is one of the potential applications of X-ray free-electron lasers (XFELs). Currently, SPI experiments on isolated proteins are limited by three factors: low signal strength, limited data and high background from gas scattering. The last two factors are largely due to the shortcomings of the aerosol sample delivery methods in use. Here we present our modified electrospray ionization (ESI) source, which we dubbed Helium-ESI (He-ESI). With it, we increased particle delivery into the interaction region by a factor of 10, for 26 nm-sized biological particles, and decreased the gas load in the interaction chamber corresponding to an 80% reduction in gas scattering when compared to the original ESI. These improvements have the potential to significantly increase the quality and quantity of SPI diffraction patterns in future experiments using He-ESI, resulting in higher-resolution structures.

4.1 Introduction

Current generation X-ray free electron lasers (XFELs) with their ability to produce highly intense X-ray pulses with durations of only a few tens of femtoseconds offer a powerful tool to image a wide variety of aerosolized particles at room temperature. Such high intensities on femtosecond time scales suggested that useful data could be collected from weakly scattering single proteins or viruses by outrunning radiation damage using the idea of "diffraction before destruction" [5]. Taking full advantage of this new capability of coherent diffractive X-ray imaging using single particles in the gas phase promises to not only deliver high-resolution structures but to extend the study towards ultrafast dynamics [117, 118], opening the door for pump-probe experiments on femto-and picosecond time scales. So far, single-particle imaging (SPI) experiments have been successfully performed by injecting the aerosolized sample into the X-ray interaction region using the "Uppsala"-injector [63] on large biological samples (70–2000 nm) using gas dynamic virtual nozzles (GDVN's) on viruses [31, 119–123], cell organelles [40], whole cells [124] and most recently on gold nanoparticles [125] using electrospray ionization (ESI).

Gas phase injection [86, 126] via an aerodynamic lens stack (ALS) has gained substantial attention for its high scattering contrast, low background scattering compared to liquid sample delivery, capacity for high-rate data collection and wide sample compatibility. A typical experimental SPI layout can be found in [61], and a modified experimental setup for He-ESI-based experiments is shown in Figure 4.1. Particularly, ESI as a sample aerosolization method has proven effective due to its ability to

produce small droplets, resulting in virtually contaminant-free sample delivery [44]. But even with the large pulse energies available at modern XFEL facilities, the diffraction patterns from small particles, such as single proteins or virus particles with sizes smaller than 50 nm have a very low signal-to-noise ratio preventing structure determination, despite computational efforts to reduce the noise [127]. A recent experiment on the GroEL complex from *E. coli* delivered using ESI highlights the challenge for small bioparticles: a high amount of background scattering from the N_2 and CO_2 in the interaction region [27]. The large gas background hampers the identification of signal from the sample of interest.

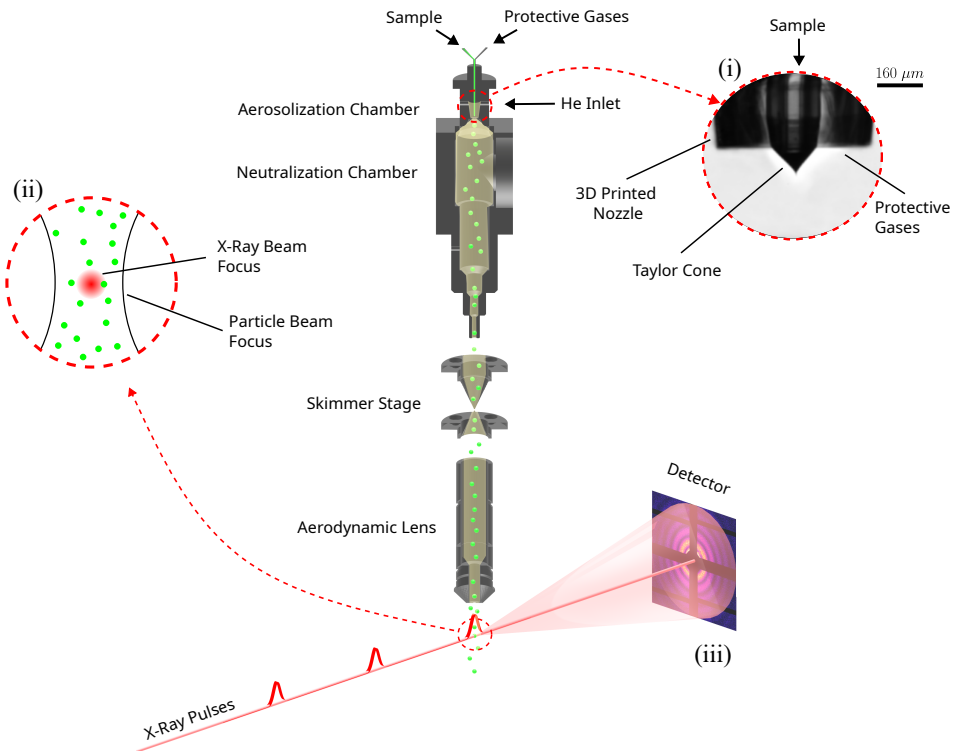

Figure 4.1: The schematic diagram details an experimental setup of a He-ESI-based aerosol injector designed for single particle imaging experiments at XFELs. This setup includes the He-ESI process illustrated at the top, which aerosolizes the sample. Subsequently, the aerosol beam is transported through the skimmer stages and the aerodynamic lens and eventually reaches the interaction chamber. Here, it intersects with the XFEL beam. The XFEL pulses scatter off the particles within the aerosol beam, generating diffraction patterns captured on the detector. (i) The Taylor cone, during standard operation of He-ESI. (ii) The interaction between a particle beam and an X-ray beam. (iii) Scattering pattern produced by a particle.

To obtain higher-resolution structures, a reduction of N_2 and CO_2 gas density in the interaction region to enhance the signal-to-noise ratio is necessary. In addition, improved particle throughput is needed to collect the several hundred thousand scatter-

ing patterns from identical particles needed to fill the 3D reciprocal space [12, 128, 129]. Therefore, improving sample delivery is one of the crucial factors in enabling high-resolution single-particle imaging at XFELs.

In this paper, we address these sample delivery challenges and present a modified ESI source, which we refer to as the Helium electrospray (He-ESI). The main change is the addition of a 3D-printed nozzle, designed to reduce the N_2 and CO_2 consumption compared to the earlier setup (original ESI) [44] while still maintaining stable sample delivery conditions. Helium (He) is introduced around the 3D-printed nozzle and serves as the main gas for particle transport. Our modifications lead to a lower N_2 and CO_2 use and a decrease of heavy gasses in the interaction region by 83%. We also demonstrate the successful use of the He-ESI with the "Uppsala"-injector and compare the performance with the original ESI in the injector setup. We observe an increase in injection yield which can be as high as a factor of 10 for the small biological particles.

Our He-ESI system shows great potential for SPI of small particles. The reduction in heavy-gas background effectively increases the signal-to-noise ratio. Furthermore, the use of He as the transport gas improves particle focusing in the "Uppsala"-injector, and enhances the throughput of particles into the interaction region. The ESI-setup developed here makes it possible to acquire millions of diffraction patterns with sufficiently low background, an important milestone on the way to high-resolution time-resolved 3D structures of isolated proteins and viruses using SPI.

4.2 Methods and Results

The experimental setup in this study consists of a modified version of the ESI introduced in [66], the "Uppsala"-injector [63] with a two-skimmer box setup, an optical scattering setup to detect the nanoparticles in the main chamber [130] and a residual gas analyzer (RGA) (Extorr Inc., XT100M) to analyze the gas composition inside the chamber.

4.2.1 Modified ESI source: He-ESI design

The modified ESI setup is shown in Figure 4.2. It includes a 3D printed nozzle (Uppsala nozzle) measuring 4.45 x 1.56 x 1.56 mm^3 printed via two-photon polymerization in a liquid resin (UpPhoto) within 35 minutes using the NanoOne 3D printing system (UpNano). After printing, the nozzle was glued to a stainless-steel tube with an inner diameter (ID) of 1.15 mm using a standard two-component epoxy glue (Loctite power

epoxy) and connected to the N_2 and CO_2 gas mixture line. To reduce the background scattering in SPI experiments, we replaced most of the N_2 and CO_2 used for particle transport with He. The gas inlet previously used for the N_2 and CO_2 gas mixture was used as the He inlet, as shown in Figure 4.2. The Uppsala nozzle is designed to hold the silica fused capillary of 360 µm outer diameter (OD) in the center of the nozzle as shown in Figure 4.2. We reduced the consumption of N_2 and CO_2 by placing a 3D-printed structure around the capillary generating an N_2 and CO_2 atmosphere between the capillary and the nozzle and filling the rest of the ESI head with He.

An alternative 3D-printed nozzle design, referred to as the EuXFEL nozzle, follows the same principle of gas replacement but does not require the use of a fused silica capillary inside. Instead, it is entirely printed using the Nanoscribe Photonic Professional GT with IP-S photoresist. This design incorporated two capillary inlets: one with an ID of 40 µm for the sample and another with an ID of 180 µm for protective gases (N_2 and CO_2). The dimensions of the EuXFEL nozzle are $1.4 \times 0.5 \times 1.2$ mm. Details on the EuXFEL nozzle can be found in the supplementary materials. Furthermore, the CAD models for both the Uppsala and EuXFEL nozzles are freely accessible and can be downloaded from our GitHub repository at (`https://github.com/ytejvarma/Helium-nozzle`) and (`https://github.com/safirafie/ESDesign`) respectively.

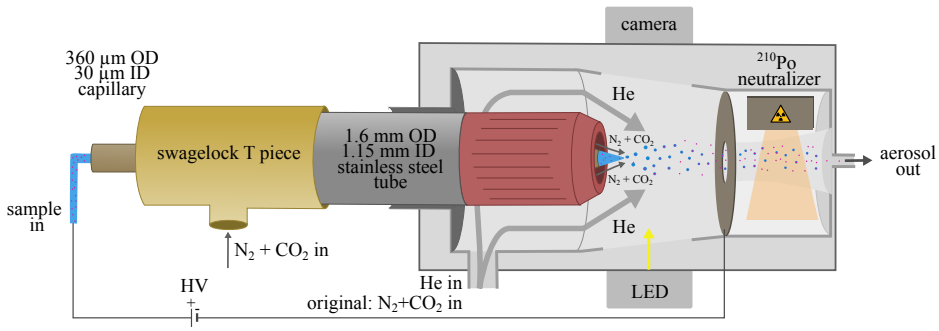

Figure 4.2: Schematic of the He-ESI. The modification of the ESI to operate with He includes a Swagelok T-piece, a stainless steel tube and the 3D-printed Uppsala nozzle. Liquid sample flows through the capillary and a stable Taylor cone is formed by applying a high voltage. In between the capillary and the inside of the nozzle a N_2 and CO_2 environment is formed with a combined flow rate of around 50 mL/min. Helium is introduced through the original gas inlet, surrounding the nozzle within the electrospray head and facilitating the flow of particles. The highly charged droplets pass through a Po-210 neutralizer. Then, the neutralized aerosol is exiting the electrospray head.

4.2.2 Simulations of Gas Flow Around the Taylor Cone

In the electrospray process, a high voltage applied between the nozzle and a grounded orifice plate creates a cone-jet meniscus, known as a Taylor cone, which is formed

when electric forces balance liquid surface tension [71, 77]. The non-uniform electric field at the tip of the Taylor cone can induce a corona discharge at a high enough voltage. The electrons released from the ionized gas molecules neutralize the positive charges on the liquid surface which causes a collapse of the Taylor cone. Therefore, preventing corona discharge, while also minimizing the presence of heavier gases that contribute to higher background X-ray scattering, is essential for stable sample delivery in SPI experiments.

Considering the required voltage for Taylor cone formation, and the geometry around the nozzle, using only light gases like helium or hydrogen to support the electrospray is not feasible due to their low electric field threshold for corona discharge. The lightest gas mixture where we achieved stable operating conditions with the nozzle design presented here was: He at 1.2 L/min, N_2 at 20 mL/min, and CO_2 at 15 mL/min. Helium was the preferred light gas, considering hydrogen's high flammability and explosive nature. N_2 alone proved insufficient to prevent corona discharge while adding minimal amounts of CO_2 insulates against the discharge.

Understanding the distribution of gas species around the Taylor cone in the He-ESI system is important for achieving stable sample delivery. Therefore, we performed finite element simulations using COMSOL Multiphysics [131]. We used the laminar flow interface and the transport of concentrated species interface and coupled these interfaces together through a multi-physics interface. The laminar flow interface allowed us to model the gas flow dynamics by computing the velocity and pressure fields of the gases. Concurrently, the transport of concentrated species interface was used to study gaseous mixtures by solving for the mass fractions of all participating species.

To monitor the risk of corona discharge around the Taylor cone, we calculated the fractional concentration of each gas, denoted as x_i and defined as:

$$x_i = \frac{c_i}{c_i + c_j + c_k}$$

where c_i symbolizes the molar concentration of the gas for which we are determining its fractional concentration, x_i. The c_j and c_k denote the molar concentrations of the remaining two gases in the mixture.

We compared the gas distribution between the original ESI and the He-ESI system, as displayed in Figures 4.3a, 4.3b, and 4.3c. In the original ESI system, a mixture of two gases was used. N_2 was utilized as the carrier gas at a flow rate of $1\,\mathrm{L/min}$, and CO_2 was employed as a protective gas, to shield the Taylor cone from corona discharge, with a flow rate of $150\,\mathrm{mL/min}$. The He-ESI system instead uses a mixture of three gases. He serves the role of the carrier gas with a flow rate of $1.2\,\mathrm{L/min}$, while N_2 and CO_2, with flow rates of $20\,\mathrm{mL/min}$ and $15\,\mathrm{mL/min}$ respectively, functioned

as protective gases. The simulation results illustrate how in the He-ESI system, the Taylor cone is effectively enveloped by CO_2, preventing corona discharge.

To study the influence of various CO_2 flow rates on the gas distribution around the Taylor cone in the He-ESI setup, we performed simulations at CO_2 flow rates of 10, 15, 30, and 50 mL/min, as depicted in Figures 4.3d and 4.3e. The He and N_2 flow rates were kept constant at 1.2 L/min and 20 mL/min, respectively. These simulations help estimate the minimal fractional concentration of gases necessary to sustain a stable Taylor cone, thus minimizing the potential for corona discharge. This provides important insights into the interactions and flow dynamics of the gases around the Taylor cone, which can further help us optimize the design and operating conditions of the electrospray system.

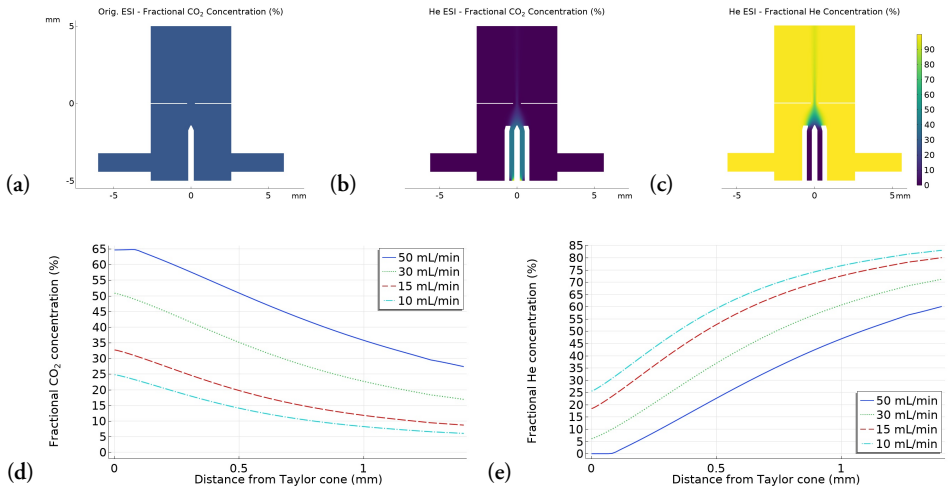

Figure 4.3: The fractional concentration of various gases in the vicinity of the Taylor cone, highlighting the effectiveness of gas shielding against corona discharge. a) The fractional concentration of CO_2 in the original ESI system. b) and c) The fractional concentration of CO_2 and He respectively in the He-ESI system. d) and e) The fractional concentration of CO_2 and He respectively in the He-ESI system under varying CO_2 flow rates while maintaining a constant He flow rate of 1.2 L/min and N_2 flow rate of 20 mL/min.

4.2.3 Operating Conditions for the He-ESI

The He-ESI with the Uppsala nozzle is stable under the following conditions: the tip of the angled capillary (conically ground at an angle of 30°) must be kept at the edge or slightly inside the nozzle, which is placed at a distance of 1.5 - 1.8 mm away from the grounded orifice of 0.5 mm diameter. The liquid sample flow rates must be 100 - 200 nL/min, the He flow rate in the ESI head should be 1.2-1.4 L/min, the N_2 flow rate 0.03-0.035 L/min, the CO_2 flow rate 0.015-0.02 L/min and the voltage between 2.2 - 2.6 kV. The stability of the He-ESI was monitored by measuring the current

(typically around 200 - 300 nA) and visually with a camera pointing at the Taylor cone. Under these conditions, the Taylor cone ejects positively charged droplets that are electrostatically trapped on the grounded counter electrode [114]. For the sample particles to reach the interaction chamber it is thus essential to neutralize them. To achieve this, we passed them through a Po-210 neutralizer which functions by ionizing nearby gas molecules into positive and negative ions. The charged droplets are subsequently neutralized by capturing ions of the opposite charge, after which the solvent evaporates and leaves behind neutral sample particles. The particles are then transported through conductive tubing to the inlet of the experimental setup.

4.2.4 Injector Setup: Operation using He-ESI

The He-ESI is coupled to the injector setup [44]. An extra helium inlet was added to the injector setup before the first skimmer stage to avoid the suction of the gas in the aerosolization and neutralization chamber of the ES due to the pumping in the skimmer stages and to protect the Taylor cone. Typically, 2.5-3 $\mathrm{L/min}$ He is added at the aerosol inlet. In total, $4.2\,\mathrm{L/min}$ He is required in the setup. The excess gas is skimmed away using scroll pumps at the two nozzle-skimmer stages. The particles enter the aerodynamic lens with a pressure of 1-1.2 mbar and exit the lens through a 1.5 mm aperture into the interaction region in the experimental chamber, which is kept at 10^{-5} mbar.

4.2.5 Gas Reduction in the Interaction Chamber

We used an RGA, mounted 25 cm away from the interaction region, to determine the composition of the gas in the interaction chamber. RGA spectra while using both types of ESI are shown in Figure 4.4. For the He-ESI (dashed red line), the largest contribution is He at 4 atomic mass units (amu) with a partial pressure, measured from the peak area, of 1.9×10^{-5} Torr, while N_2 and CO_2, shown in the spectrum at 28 and 44 amu, have partial pressures of 1.6×10^{-6} Torr and 3.1×10^{-7} Torr respectively. There's a further peak at 18 amu due to water contamination.

The relative composition of the input gases to the He-ESI is 1.22 % N_2 and 0.97 % CO_2, compared to 8 % N_2 and 1.5 % CO_2 measured in the interaction chamber. This discrepancy may be explained by the different pumping efficiency for He, N_2 and CO_2 based on Graham's law, which states that the rate of diffusion or effusion of gas is inversely proportional to its molecular weight. This implies, that N_2 and CO_2 diffuse much slower than He when passing through the nozzle in the two skimmer stages leading to He being skimmed away first and more efficiently.

The RGA spectrum of the original ESI, shown in black, shows much larger N_2 and CO_2 peaks, with partial pressures of 8.7×10^{-6} and 2.4×10^{-6} Torr respectively.

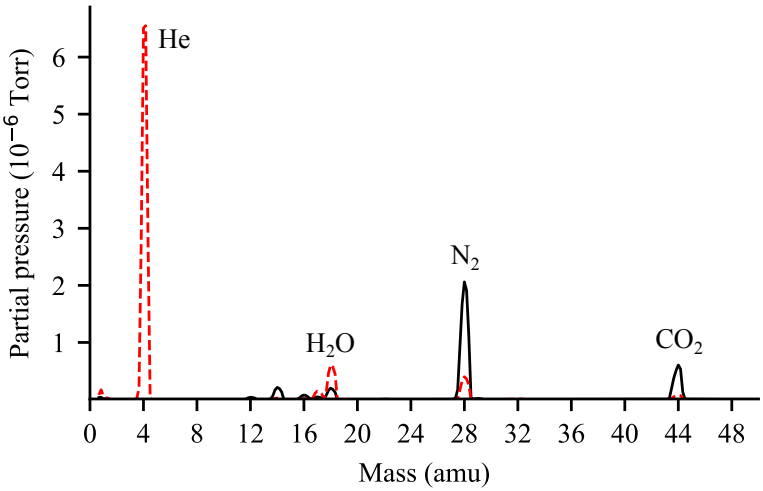

Figure 4.4: Residual gas analysis spectrum inside the interaction chamber. Measured for the He-ESI (dashed red) with flow rates of 4.2 L/min He, 0.03 L/min N2, 0.015 L/min CO2 and the original ESI (solid black) with flow rates of 1 L/min N2 and 0.2 L/min CO2.

While the gases in the interaction chamber will scatter both elastically and inelastically, the inelastically scattered photons can be filtered due to their different energy. But the elastically scattered ones are indistinguishable from those scattered by the sample and are the main contributors to background noise in SPI [27]. For the resolutions relevant to SPI, each gas molecule is well approximated as a point scatterer and the total scattering is then proportional to the square of the number of electrons. We can then estimate the elastic scattering from the gas as the weighted sum of the contributions of the different gas species, and with it calculate the expected elastic scattering by the gas when using the He-ESI relative to the original ESI (I_{rel}),

$$I_{rel} = \frac{p^{\text{new}}_{N_2} Z^2_{N_2} + p^{\text{new}}_{CO_2} Z^2_{CO_2} + p^{\text{new}}_{He} Z^2_{He}}{p^{\text{old}}_{N_2} Z^2_{N_2} + p^{\text{old}}_{CO_2} Z^2_{CO_2}},$$

where p^{new} are the partial pressures of the He-ESI setup, p^{old} of the original ESI and Z is the total number of electrons of each gas molecule. Using this equation with the partial pressures measured above we obtain an I_{rel} of 0.188 or an expected reduction of scattering intensity by ≈ 81 %.

4.2.6 Sample delivery performance with the He-ESI

To show that the He-ESI is working stable and generates aerosolized particles suitable for SPI experiments, we coupled the He-ESI to the "Uppsala"-injector. To detect the flow of particles into the interaction region we used a Rayleigh-scattering microscopy setup [130] and recorded particle intensities and beam evolution curves for 20-80 nm polystyrene spheres (PS) in a 20 mM ammonium acetate (AmAc) buffer solution. The beam-evolution curve is shown in the supplementary information Figure S2. At a given injector pressure, the particle-beam focus position moves away from the injector exit with increasing particle size. A similar behaviour has been observed in a previous study using the same injector and GDVN aerosolization, i.e. focusing with He, for PS with diameters larger than 40 nm [63]. For larger particles, the gas density in the focus is lower. In addition, the opening angle of the particle beam decreases with increasing particle size. The particle-beam parameters are summarized in Tab. S1. The data collection and analysis are discussed in a [130]. Next, we characterized the particle-beam density at the particle beam focus for different sizes of PS and Bacteriophage MS2 (MS2) and compared it to particle-beam density measurements using the original ESI for aerosolization, i.e. using N_2 as the main carrier gas. As a proxy for the particle-beam number density, we show the number of particles collected in 1000 frames. Each frame contains one laser pulse for particle detection. Table 4.1 shows the measured mean number of particles detected per 1000 frames in the particle-beam focus. For all particle sizes, the measured number of particles is higher using the He-ESI compared to the original ESI. While the improvement of the measured particle numbers is different for the used sizes, the highest improvement in particle throughput, by a factor of $\approx$ 11, is observed in the bioparticle MS2.

Table 4.1: Comparison between He-ESI and original ESI of the mean number of particles as a function of the sample diameter.

	Particles per 1000 frames	
Sample/DMA size (nm)	He-ESI	Original-ESI
Bacteriophage MS2/ 25.9	460	42
20 nm PS/ 18.9	1010	271
30 nm PS/ 28.9	2546	517
40 nm PS/ 42.9	2264	874
50 nm PS/ 59.4	1553	939
70 nm PS/ 76.4	1118	527
80 nm PS/ 88.2	1150	300

4.2.6.1 Exploration of Various Ionization Techniques in He-ESI

A comparative study was conducted to analyze the transmission efficiency between two different neutralization techniques used in He-ESI: a Polonium (Po-210) source, a radioactive alpha particle emitter, and a vacuum ultraviolet (VUV) ionizer, which is essentially a VUV deuterium lamp. Both neutralizers function by ionizing nearby gas molecules into positive and negative ions, enabling ES-generated charged particles to be neutralized by capturing ions of the opposite charge. The key difference lies in their ionization methods: the Po-210 source ionizes gas molecules through collisions with alpha particles, whereas the VUV ionizer employs photoionization to achieve the same effect. The target sample utilized for this experiment was cube-shaped silver nanoparticles, with a side length of 75 nm, suspended in ethanol. In both techniques, the gas flow rates were maintained at 1 L/min for He and 30 mL/min for CO_2. Particle detection was carried out in the interaction chamber using Rayleigh scattering [130]. The results from the number of particles detected showed that the Polonium source delivered approximately 5% more particles than the VUV ionizer to the interaction chamber.

Nonetheless, given that VUV light is more efficient at ionizing N_2 gas [61], we extended our experiment by adding 30 mL/min of N_2 through the He inlet. This introduction of N_2 enhanced the transmission efficiency of the VUV ionizer setup and outperformed the Polonium source setup by delivering approximately 30% more particles. This enhancement can be attributed to the improved neutralization of the particles, facilitated by the VUV ionizer's more effective in ionizing N_2. These findings suggest that the inclusion of N_2 gas in the VUV ionizer setup could be a potential strategy to enhance transmission efficiency in He-ESI. It is important to highlight, though, that the advantages gained from incorporating N_2 need to be balanced against its potential contribution to background noise.

4.3 Discussion and Outlook

Within this paper, we presented improvements in the sample aerosolization process by developing a He-ESI to reduce the background scattering due to gases in SPI experiments. We used 3D printed nozzles to reduce the amount of N_2 and CO_2 and kept modifications of the previously used ESI setup to a minimum. With the He-ESI, the main particle transport gas into the interaction chamber is He. In the interaction chamber and based on RGA measurements using the He-ESI with the Uppsala-nozzle, the amount of N_2 was reduced by 82 % and for CO_2 by 87.7 %. While the large reduction of the heavy gasses in the initial gas mixture could not be observed to the same extent in the interaction region, presumably due to different pumping efficiencies,

an optimization of the skimmer assembly may improve the ratio in the interaction region further. Nonetheless, assuming the ratio of the gasses measured in the RGA translates into the ratio of contribution to background scattering, we reduced the gas background scattering off the gas by 81 %.

Additionally, through simulations conducted using COMSOL Multiphysics, our study has deepened the understanding of gas flow dynamics around the Taylor cone in a He-ESI system. This allowed us to model the behaviour of different gas mixtures, examining their respective impacts on protecting the Taylor cone from corona discharge. Given our optimal operational conditions with a water-based buffer our simulations suggest that to maintain a stable Taylor cone, the He percentage should not exceed 20% at the cone's tip. Further computational analysis of the gas distribution and breakdown voltage can aid in determining the minimum fractional concentration necessary to maintain a stable cone before corona discharge occurs.

Our modification of the ESI not only demonstrates a decreased use of heavy gasses for sample injection but also an increased throughput of particles into the interaction region. The highest increase in transmission of particles was observed while injecting small bioparticles: approximately by a factor of 11 for MS2 particles. Whereas, while delivering PS into the interaction region, we measure an increase in the transmission of particles by a factor of 2 to 5 depending on the particle size.

To further enhance particle transmission, we conducted a comparative analysis of the transmission efficiency between Po-210 sources and VUV ionizer techniques within He-ESI systems. Our results demonstrated that by adding 30 mL/min of N_2 gas along with He at the He inlet, the VUV ionizer's performance was enhanced, surpassing the Po-210 source by approximately 30%. For a more comprehensive understanding of their impact on transmission efficiency, future studies could investigate the simultaneous utilization of both the Po-210 source and the VUV ionizer in He-ESI systems.

Although this is not the first adaptation of ES injection for X-ray diffractive imaging, the presented modification is a much-required leap towards single protein imaging by aiming at lower background scattering from the injection gases, allowing us to recognize lower scattering signals from the sample in the diffraction data. We expect the He-ESI to improve the quality of collected data and provide better experimental conditions for X-ray imaging of small nanoparticles not only due to the lowered background but also because of a higher particle transmission through the injector. Together, higher quality and quantity of diffraction patterns can be collected in the future using a He-ESI for sample aerosolization.

4.4 Supplementary Materials

4.4.1 He-ESI Design: the EuXFEL Nozzle

The EuXFEL nozzle was engineered using Siemens' NX software and was designed with three capillary inlets suitable for 360 µm outer diameter (OD) fused silica capillaries for fluid feed, along with two outlets as shown in Figure 4.5. The inlet ports comprised one for a sample with an inner diameter (ID) of 40 µm, another for gas with an ID of 180 µm, and a dummy one which aids in centering the sample capillary. The outlet ports included one designated for the sample, with an ID of 40 µm and an angle of approximately 10°, and another, concentric with the first, designated for gas, with an ID of 410 µm and an angle of approximately 7°.

The nozzle design was outputted in STL formats. The conversion of these STL-based 3D designs into print-job instructions, or GWL, was executed using Nanoscribe's DeScribe software. For better structural stability of the fabricated devices, we adopted a solid volume printing strategy with slicing of 1 µm and hatching of 0.5 µm. The devices were then printed using the Nanoscribe Photonic Professional GT with IP-S photoresist as the printing material. The process utilized a 25x objective lens from Zeiss, full laser power, and a printing velocity of 100.000 $\mu m\,s^{-1}$. Under these conditions, the printing duration for a single device was approximately one hour.

Following the printing process, the glass slide with the cured photoresist was submerged in a beaker of propylene glycol methyl ether acetate (PGMEA) for one or two days to dissolve any remaining uncured parts, a process known as development. Post-development, the devices were transferred to a beaker of isopropanol for about 30 min, then relocated to another beaker filled with fresh isopropanol. Finally, the devices were left on a cleanroom cloth to dry under ambient conditions.

The nozzles were assembled on clean polydimethylsiloxane (PDMS) sheet, with the process monitored under an optical microscope. To secure the devices, an additional piece of PDMS was applied over them. Following this, three fused silica capillaries, each with an OD of 360 µm, were inserted into their designated fluid inlets on the nozzle and secured with a 5-minute epoxy glue from Devcom. These capillaries were then guided through hollow stainless-steel tubing with an OD of 1/16 inch (IDEX U-145 with an ID of 0.046 inches) and glued between the nozzle material and steel.

4.4.2 Operating Conditions for the EuXFEL Nozzle

The operating stability of the He-ESI system is influenced by factors such as the buffer type, the buffer conductivity, and the geometry of the aerosolization chamber. To

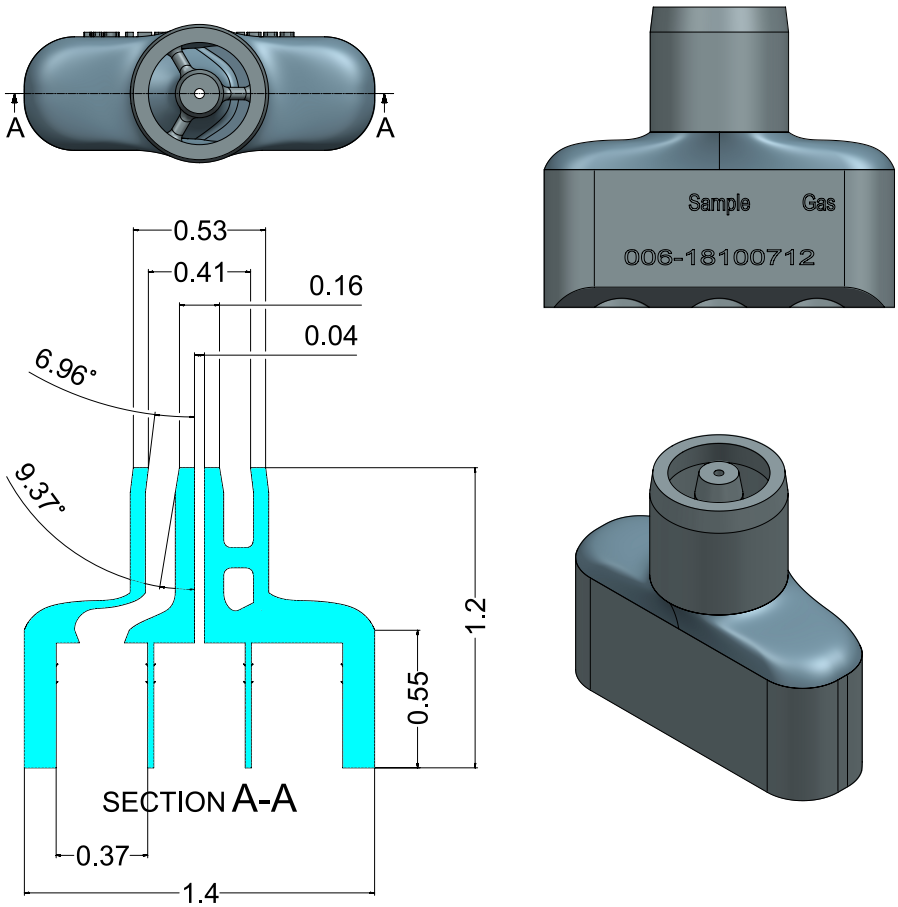

Figure 4.5: Schematic drawings of the EuXFEL nozzle illustrate the dimensions and depict the inlets and outlets of the nozzle.

minimize the presence of heavier gases and maintain a stable Taylor cone, the operating conditions were carefully optimized. Experiments were conducted using the EuXFEL nozzle with two different buffers: water (with conductivities ranging from 900 to 1600 μS/cm) and ethanol (with conductivities ranging from 800 to 1300 μS/cm). With the water buffer, we used a He flow rate of $1 - 1.5$ L/min, a N_2 flow rate of $20 - 30$ mL/min, and a CO_2 flow rate of $15 - 25$ mL/min. With the ethanol buffer, the He flow rate was adjusted to $1 - 1.6$ L/min, while the CO_2 flow rate was set at $10 - 20$ mL/min, without any N_2 flow. The nozzle was tested with two different ionizers: a Po-210 source and a UV ionizer, before transporting the particles to the Uppsala injector.

4.4.3 PS particle-beam parameters

The particle-beam width depending on the distance from the injector exit was measured for different sizes of PS. A Gaussian beam evolution fit was used to determine the focus width and the focus position. The particle-beam evolution curves are shown in Figure 4.6 and the focus values are summarized in Table 4.2. A clear shift of the particle-beam focus towards the injector exit with decreasing particle size is observed and the particle-beam focus width increases as the particle size decreases.

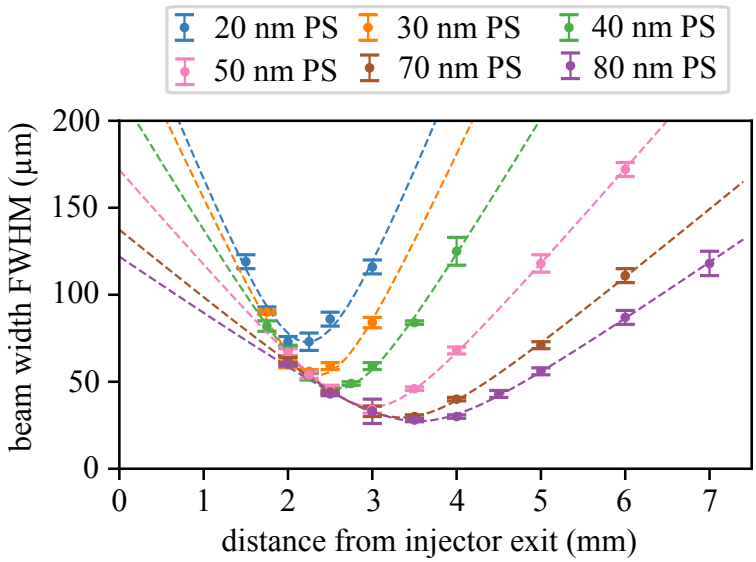

Figure 4.6: Particle-beam evolution curves for 20 - 80 nm PS at 1.0 mbar injector pressure using the He-ESI with Uppsala nozzle for aerosolization. The main focussing gas is He.

Table 4.2: Experimental particle-beam parameters (focus position and width) for different sizes of PS. The particles were aerosolized using the He-ESI and the injector pressure was kept constant at 1.1 mbar.

Sample/DMA size (nm)	focus position (mm)	focus width FWHM (µm)
20 nm PS/ 18.9	2.23	73
30 nm PS/ 28.9	2.37	54
40 nm PS/ 42.9	2.59	46
50 nm PS/ 59.4	2.99	36
70 nm PS/ 76.4	3.35	29
80 nm PS/ 88.2	3.55	27

Chapter 5

Coaxial Helium Electrospray for Single-Particle Imaging at X-ray Free Electron Lasers

This chapter is based on the publication: **Rafie-Zinedine, S.**, Bielecki, J., Schulz, J., & Heymann, M., "Coaxial Helium Electrospray for Single-Particle Imaging at X-ray Free Electron Lasers", Submitted to Journal of Synchrotron Radiation.

Contribution

I contributed to the conception of the idea, development and construction of the setup, data recording and data analysis, preparation of figures for the manuscript, writing of the initial draft, and updating the manuscript in collaboration with all co-authors.

Abstract

Single particle imaging at X-ray free electron lasers relies on suitable sample injection of nanoscale macromolecules and particles into the gas phase at room temperature. A liquid-sheet strategy considerably extended the range of suitable samples to include zero and high conductivities, of up to 40,000 μS/cm - a more then $\sim$8 fold increased range compared to conventional electrosprays. A helium chamber atmosphere in combination with a protective gas-sheet reduced background noise more

then three-fold. These developments suggests new avenues to study ever more demanding biological and material science samples in the future.

5.1 Introduction

The brilliance of X-ray free electron lasers (XFELs) paved the way for single particle imaging (SPI) to capture room temperature diffraction patterns of nanoscopic particles at high-resolution, including biological samples [12, 13]. Their short pulse duration of ≈10 fs is invaluable to resolve ultrafast structural dynamics but also for outrunning conventional radiation damage via 'diffraction-before-destruction' imaging [5]. While diffraction patterns generally provide only a 2D image plane of the 3D particle, a complete 3D structure can be reconstructed from combing multiple individual diffraction patterns into a 3D dataset in reciprocal space. Phase retrieval algorithms can then reconstruct the 3D particle structure [17]. To do so requires individual particles to be as homogeneous and to be delivered as reproducibly as possible, which promoted a continuous evolution in liquid jet and gas phase injection technologies [44, 46].

Electrospray (ES) has proven especially effective for single particle imaging [44]. In this injection, electrical forces counterbalance liquid surface tension to form a cone-jet meniscus called Taylor cone [66, 71, 114] that subsequently breaks into a monodisperse stream of nano- to micrometer-sized droplets (Figure 1) [61]. Particles are then neutralized to prevent their capture on grounded surfaces and focused to a particle beam into the X-ray interaction region via an aerosol lens stack [108, 110, 111]. Aerodynamic lensing can accelerate particles to hundreds of meters per second [44, 108]. This delivery modality is hence particularly well-suited to prevent multiple exposures of the same particle at fast megahertz pulse rates, such as those achieved at the European XFEL, which emits X-ray trains at 10 Hz, each comprising up to 2700 pulses with 220 ns spacing [14]. While traveling to the X-ray interaction region, solvent evaporates from these droplets to yield virtually contaminant free particles in the gas phase [44] for high scattering contrast and lower background signal of recorded diffraction patterns in the 2D detector. To date a broad range of samples, including cells [29], cell organelles [40], viruses [30–39], proteins [27], and inorganic nanoparticles [42, 43] were already imaged using this approach.

While providing encouraging proof-of principle results, many biological samples continue to be difficult to electrospray for single particle imaging. Firstly, the optimal salt concentration for the sample may be too far away from the one required for a stable Taylor cone, forcing non-ideal trade-offs. Especially, low salt regimes fail to sufficiently suppress surface tension forces for reliable injection. A co-flow regime, where

the low conductivity sample is surrounded by a suitable electrospray buffer could provide the best conditions for both sample stability and Taylor cone formation. A similar double-flow focusing strategy has already been demonstrated for gas dynamic virtual nozzles to inject microcrystal slurry [46, 56]. Also, non-conductive olive oil, which alone cannot electrospray [66] could be aerosolized by co-injection with a conductive water solution in a coaxial electrospray [132]. Here, a Taylor cone formed by the water solution was coated with a thin layer of olive oil to produce a core-shell capsule aerosol. Secondly, background scattering from heavy cases like N_2 and CO_2 used in the electrospray chamber result in too low signal-to-noise ratios for structure determination [27], especially for smaller particles like single proteins or viruses below 50 nm diameter. A recently proposed Helium Electrospray (HeES) method introduced helium as the main gas for particle transport, while restricting N_2 and CO_2 to a narrow region around the Taylor cone to protect it from corona discharge, thereby decreasing background noise significantly [116].

While conceptually simple, realizing such filigree sheet flows for both the liquid and the gas stream experimentally requires precisely microfabricated injectors. Cutting edge two-photon polymerization has been shown to be capable to realize complex 3D fluidic devices with submicron precision, which has been readily exploited for advanced microfluidic nozzles, offering improved performance, miniaturization, and customization [46, 53].

We present a Coaxial Helium Electrospray (CHeES) nozzle for single particle imaging experiments at XFELs, which can inject a broader range of sample conductivities at lower background noise then conventional electrospray injectors. CHeES uses an ultracompact 3D nozzle design to simultaneously flow two coaxial liquids and a coaxial gas to ensure stable sample delivery. It can spray a wide range of samples, from non-conductive to relatively high conductivities (up to 40,000 μS/cm), while simultaneously reducing N_2 and CO_2 gases in the interaction region by factors of 3.5 and 2.2, respectively. CHeES readily integrates with existing injector setups, including the 'Uppsala' injector at the SPB/SFX instrument of the European XFEL, highlighting its practical utility in current XFEL facilities. CHeES experimentally realized a more then threefold reduction in background noise without compromising the injection yield when compared to a conventional electroscopes injectors, which we demonstrate by collecting high quality diffraction patterns from cube-shaped silver nanoparticles with a 55 nm side length. This may pave the way to explore structures that were previously challenging or impossible to study in single particle imaging.

5.2 Methods

5.2.1 Experimental Setup

Our single particle imaging set-up at the European XFEL features a modified electrospray aerosol generator, consisting of an aerosolization chamber with a 3D-printed CHeES nozzle and a neutralization chamber, separated by an orifice disk plate (Figure 5.1). It is building on a previous instrument [61]. In brief: The CHeES nozzle aerosolizes a sample solution into positively charged droplets. Solvent evaporation reduces these in positively charged particles, which enter a 25.2 mm diameter neutralization chamber with vacuum ultraviolet ionizer (Hamamatsu L12542). The ionizer radiation creates bipolar gas ions that neutralize the charged particles to prevent their adhesion to the grounded chamber surfaces. Neutralized particles then pass through the 'Uppsala' injector [63], which includes a two-skimmer box for excess gas removal and an aerosol lens stack for particle focusing. These particles intersect with a pulsed X-ray beam, with a downstream detector capturing diffraction patterns. Additionally, a residual gas analyzer can monitor gas composition inside the interaction chamber in real time [133].

To achieve a defined CO_2 gas sheet around the Taylor cone, the CHeES aerosol generator and used a three way gas flow control circuit (Figure 5.2). This configuration can utilize nitrogen or helium mode to prevent corona discharge (Table 5.1). Mass flow controllers (Bronkhorst model F-201CV) regulate each gas flow rate independently. Differential pressure meters (Bronkhorst model P-506C) with control valves (model F-001) maintained a constant pressure difference ΔP across the capillaries to regulate sample and sheet-liquid flow rates independently. A microscope comprising a fiber-coupled LED, infinity-corrected objectives (5X Mitutoyo Plan Apo f=200), a tube lens (Thorlabs TTL200-A), and a CCD camera (Basler acA2440-20gm) was used to image the Taylor cone. To induce Taylor cone formation, a high voltage was applied to the sheet-liquid reservoir, while the orifice plate, aerosolization, and neutralization chambers were set to ground. The CHeES nozzle tip and the grounded orifice plate were placed approximately 1 mm apart. Droplet sizes were characterized using a scanning mobility particle sizer (SMPS) (TSI 3082 Electrostatic classifier, TSI 3788 N-WCPC), linked to the generator's outlet for size distribution recording.

Each experimental data point, sampled liquid-sheet and sample flow rates repeatedly, including over various independent replicates using different 3D-printed CHeES nozzles of the same design. Real-time microscopy was used to to monitor Taylor cone stability during data collection, which was essential to obtain reproducible data. Gas mass flows were limited to not exceed 2×10^{-4} mbar chamber pressures to ensure save operation of the AGIPD X-ray detector. Other applications, not limited in this

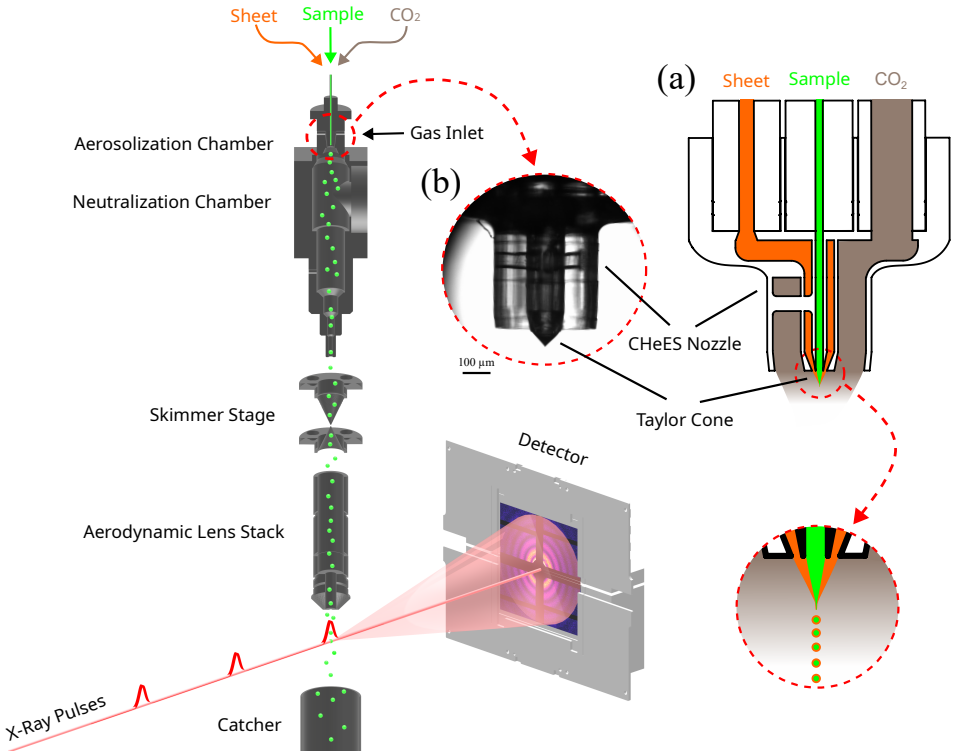

Figure 5.1: Schematic diagram of the coaxial helium electrospray (CHeES) aerosol injector. After aerosolization in the CHeES nozzle the resulting particle beam is neutralized, passes a skimmer stage and is focused by aerodynamic lens stack into the X-ray interaction chamber to collect diffraction patterns. (a) The CHeES nozzle is designed to initiate a co-axial sample and electrospray buffer flow in the Taylor cone protected by a CO_2 gas sheet to form core-shell droplets.

regard are expected to achieve higher transmission rates for increased gas flows.

Core-shell droplet size quantification experiments used a reference sample solution containing 1% (v/v) sucrose, 20 mM ammonium acetate in water. Conductivity samples ranged between 0 mM (0 μS/cm) to 550 mM ammonium acetate (~44,000 μS/cm). Buffer conductivities were confirmed with a conductivity meter (SevenExcellence Cond meter). The droplet sizes were calculated from measured SMPS particle sizes as previously reported [44]. For this, sucrose is used as a non-volatile additive to determine the droplet size as:

$$D_{\text{droplet}} = D_{\text{particle}} \quad C^{-1/3} \tag{5.1}$$

where C is the volume-to-volume (v/v) concentration of sucrose.

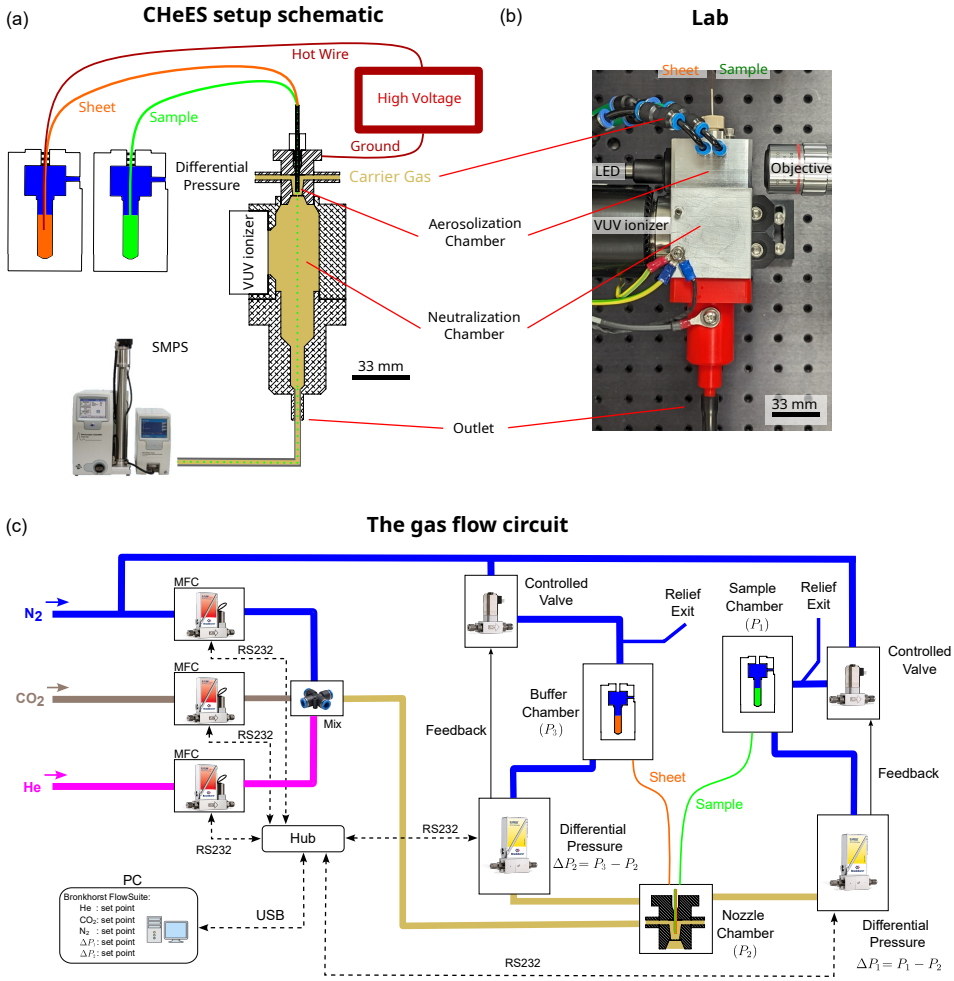

Figure 5.2: CHeES aerosol generator set-up. (a) A detailed illustration of the CHeES system configuration illustrates liquid lines, along with the high voltage and carrier gas connections. Sheet (outer liquid) and sample (inner liquid) aerosolize through Taylor cone formation and fly to the neutralization chamber to be neutralized by a vacuum ultraviolet neutralizer before exiting into an SMPS for droplet sizing. (b) Photograph of the physical configuration of the CHeES aerosolizer in the lab. (c) Schematic of the gas flow circuit design with an emphasis on the integration of mass flow controller and differential pressure meters coupled with control valves to regulate flow rates of sample and sheet-liquid and carrier gases.

5.2.2 CHeES Design

The CHeES nozzle was designed using Siemens' NX CAD software and exported to .STL file format. The design is available at the GitHub repository: `https://github.com/safirafie/ESDesign`. Nozzles were 3D printed as previously reported [46, 53]. In brief, IP-S photoresist was exposed on a Photonic Professional GT equipped with a 25x objective using solid-volume settings with 1 μm slicing and

Table 5.1: Gas-sheet and liquid-sheet combinations for helium and nitrogen mode operation.

Parameter	Helium-mode		Nitrogen-mode
liquid-sheet	water-based	ethanol-based	ethanol-based
He flow [L/min]	3	3	–
N_2 flow [L/min]	0.08	0.06	1
CO_2 flow [L/min]	0.06	0.03	0.13
applied Voltage [V]	3900 – 4400	1650 – 1950	1800 – 2100
liquid flow [nL/min]	≥357	≥433	≥433
liquid conductivity [μS/cm]	503	659	659
ammonium acetate [mM]	5	80	80

0.5 μm hatching when configuring the print job in DeScribe (all Nanoscribe). Excess resin was developed away by incubating in propylene glycol methyl ether acetate (PGMEA) for about one day, followed by three 30-minute wash steps in isopropanol and subsequent air-drying on a cleanroom cloth. Nozzles where then placed on a flat polydimethylsiloxane (PDMS) sheet to inserted three fused silica capillaries (Polymicro), each with a 360 μm outer diameter (OD) and inner diameters (IDs) of 40 μm for the sample, a 75 μm for the buffer, and 220 μm for CO_2 gas with a length of about 40 cm for lab testing and about 2 m for XFEL experiments. Devcon 5-minute epoxy was then used to glue all inlet capillaries into the 3D printed nozzle and subsequently into a hollow stainless-steel tubing (IDEX U-145, ID 0.046 inches, OD 1/16 inches).

5.2.3 Simulations of Gas Flow Around the Taylor Cone

To track the gas distribution surrounding the Taylor cone, the fractional concentration of each gas, represented as x_i, was calculated using finite element modeling (COMSOL Multiphysics 2022), as previously reported [116]. In brief, a laminar flow interface modeled gas flow dynamics, calculating velocity and pressure in the aerosolization chamber, while a transport interface analyzed the behavior of the gaseous mixtures by determining mass fractions. Gas mass fractional concentration was defined as:

$$x_i = \frac{c_i}{c_i + c_j + c_k}$$

where c_i represents the molar concentration of the specific gas whose fractional concentration, x_i and the other two gases (c_j and c_k) present in the mixture. Complete details for the finite element model are provided in (SI Figures 5.10, 5.11, 5.12).

5.2.4 CHeES operating conditions

While sample flow rates ranged between 32 and 877 nL/min, the buffer flow was set between 401 to 602 nL/min. These flow rates (Q) were regulated by adjusting the pressure difference (ΔP) across the capillaries, in accordance with the Hagen-Poiseuille equation:

$$Q = \frac{\pi(ID/2)^4 \Delta P}{8\eta L} \tag{5.2}$$

with η as the fluid viscosity and the inlet dimensions as L = 40 cm and ID's of 40 μm for sample and 75 μm for buffer. A voltage in the range of 2 to 4 kilovolts (kV) relative to the counter electrode was applied to the buffer solution to induce and stabilize the Taylor cone. Formation and Stability of the Taylor cone was observed visually via the in-line microscope and by tracking the applied electric current and the voltage adjusted as needed. Note that a stable Taylor cone constitutes an equilibrium between electrostatic forces and liquid surface tension at the interface [71, 77]. Also, the CHeES configuration does not require an electrode to apply a voltage on the sample inlet. Under these conditions, the Taylor cone is formed by the outer buffer liquid, which envelops the inner sample liquid stream. This results in the ejection of positively charged core-shell droplets, consisting of a buffer liquid shell and a sample solution core, as illustrated in Figure 5.1. After droplet ejection, all volatile components from both liquids streams evaporate, leaving behind sample particles in the gas phase.

For stable injection the helium mode light gas mixture called was slightly adjusted for water or ethanol liquid-sheets (Table 5.1). Helium was preferred over the highly flammable hydrogen. Alternatively, the injector can also be operated with the conventional carrier gas environment (nitrogen mode). While a pure nitrogen atmosphere could not prevent corona discharge, inclusion of minimal quantities of CO_2 sufficed to maintain stable electrosprays.

5.3 Results And Discussion

5.3.1 Multiphysics modeling of gas sheet for corona discharge protection

The high required voltages for Taylor cone formation and the specific geometric considerations surrounding the nozzle pose a risk for corona discharge. If the break through voltage is exceeded, gas molecules can ionize and then neutralize the positively charged liquid surface to destabilize the cone. Worse, arching inside the experimental chamber can damage sensitive electrical devices, such as the detector irreparably.

While light gases such as helium or hydrogen show lower X-ray background scattering then heavier gases such as nitrogen and carbon dioxide, their lower electric field thresholds [134] have so far been deemed to risky for electrospray based single particle imaging.

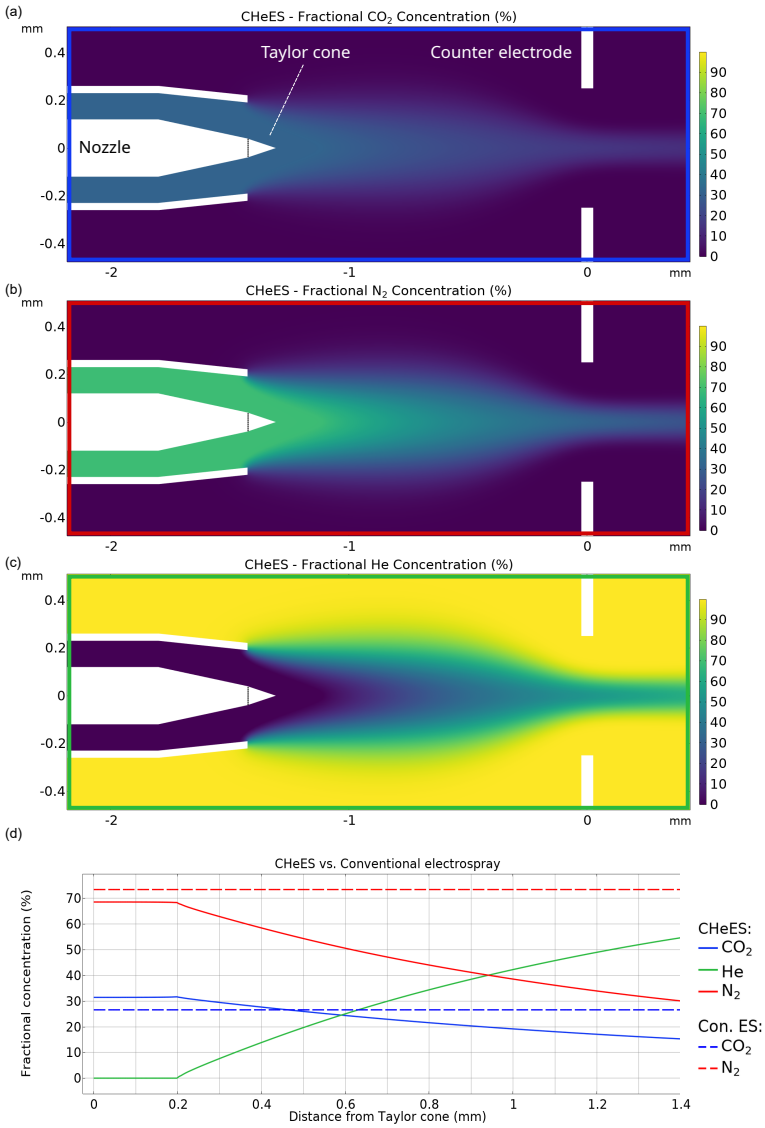

Figure 5.3: Finite element modeling of gas flows around the Taylor cone in the CHeES nozzle underscore the effectiveness of gas shielding to prevent corona discharge. Fractional gas concentrations of (a) CO_2, (b) N_2, and (c) helium indicate that a large protective CO_2 sheet can form around the Taylor cone. A safe gas atmosphere composition similar to the conventional electrospray extends about halfway from the tip of the Taylor cone to the counter electrode (d).

We considered the conventional nitrogen chamber atmosphere comprising 73% N_2 and 27% CO_2 around the Taylor cone as a safe reference (Table 5.1). Finite element modeling confirmed that a comparable gas atmosphere can be maintained to about half a millimeter away from the Taylor cone by perfusing a narrow gas-sheet of 30 mL/min CO_2 directly around the Taylor cone at the CHeES orifice to protect against corona discharge (Figure 5.3). With steady state injection of 3 L/min helium and 60 mL/min nitrogen, this would induce a 65% helium atmosphere into the X-ray interaction region for minimal background scattering.

5.3.2 CHeES nozzle design and characterization

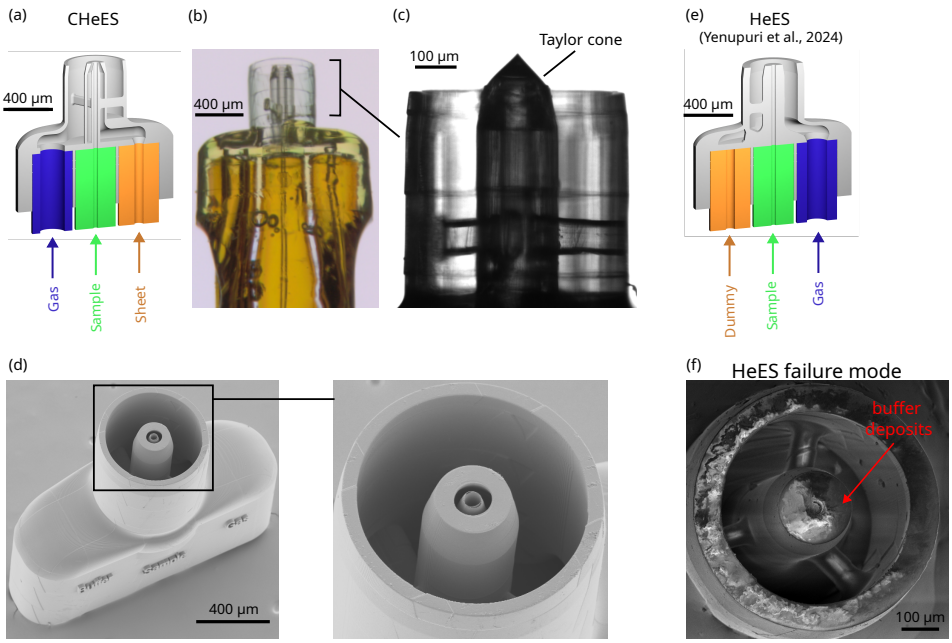

Figure 5.4: Design and Assembly of the CHeES Nozzle. Narrow 40 μm and 75 μm inner diameter lines minimize inner sample and outer sheet-liquid dead volumes. CAD design (a) with color coded inlet capillaries and stereomicrograph (b) of an assembled nozzle. Bright field microscopy image (c) of a CHeES nozzle in operation, forming a Taylor cone at the nozzle orifice. Scanning electron microscopy (d) confirmed accurate fabrication of the fine features of the nozzle orifice used to form a conductive liquid sheet around the sample stream in the Taylor cone, giving CHeES more stable operating characteristics compared to conventional electrospray nozzles (e), which are prone to clogging when non-volatile solutes deposit on the orifice over time. Scanning electron mircographs revealed extensive sucrose deposits (f) on the orifice after clogging from spraying 1% v/v sucrose buffer for about an hour.

Considering these simulation results, we designed a nozzle of about 1.4 x 0.6 x 1.25 mm in size (Figure 5.4). The design features three capillary inlets for 360 μm OD

fused silica capillaries that propagate into the previously simulated coaxial hydrodynamic flow focusing geometry. It was readily microfabricated using established 2photon stereolithography and assembly techniques [46, 53] and operated a stable cone-jet when spraying buffer of 80 mM ammonium acetate in ethanol or 20 mM ammonium acetate in water (Figure 5.4c). The liquid sheet completely eradicated nozzle clogging artifacts from solute crust formation at the at the liquid-gas interface, which pose a common failure mode in conventional electrosprays such as the related HeES nozzle [116] (Figure 5.4ef) .

5.3.3 Liquid sheet formation and conductivity range quantification

An ideal liquid-sheet combines a low surface tension with a suitably large conductivity to form a stable Taylor cone at low electric fields. This in turn allows for lower applied voltages and hence overall lower gas-sheet flows around the Taylor cone, as the critical breakdown voltage decreases according to Paschen's law. Following the original double flow-focusing concept [56], we explored ammonium acetate in ethanol as a low surface tension sheet buffer by testing against a 1% v/v sucrose solution in water as the inner liquid. We identified 401 nL/min sheet of 80 mM ammonium acetate in ethanol with a conductivity of 659 μS/cm to show best Taylor cone stability and aerosol generation from the tested range between 20 - 120 mM ammonium acetate (SI Movie 5.9). Helium mode (Table 5.1) was defined to stably jet with this ideal sheet liquid. For comparison, a 5 mM ammonium acetate in water with a comparable conductivity of 503 μS/cm liquid-sheet flown at 357 nL/min required a much higher 4200 V for stable jetting. Accordingly, a heavy gas flows were increased to 80 mL/min of N_2 and 60 mL/min of CO_2 gas-sheet in helium mode for water based liquid-sheets (Table 5.1).

To test our hypothesis for liquid sheet assisted Taylor cone formation, we titrated a range of inner samples with different conductivities against a reference outer liquid-sheet of 80 mM ammonium acetate in ethanol. The inner liquid contained 1% sucrose in water and 0 to 550 mM ammonium acetate, corresponding to conductivities of 0 to ~44,000 μS/cm. We then quantified the minimum and maximum inner flow rate limits for stable Taylor cone formation at fixed outer flow rates of 401 or 602 nL/min (Figure 5.5). The CHeES nozzle successfully sprayed samples ranging from non-conductive to relatively highly conductivities of up to 40,000 μS/cm. In contrast, the conventional electrospray nozzle achieved stable Taylor cones only for the much narrower window between 100 - 6,000 μS/cm, as unsuitably low or excessively high surface charge densities impede cone-jet stability. We can hence deduce that the sheet flow hypothesis holds to the extend that the range of acceptable sample buffers could be noticeably improved.

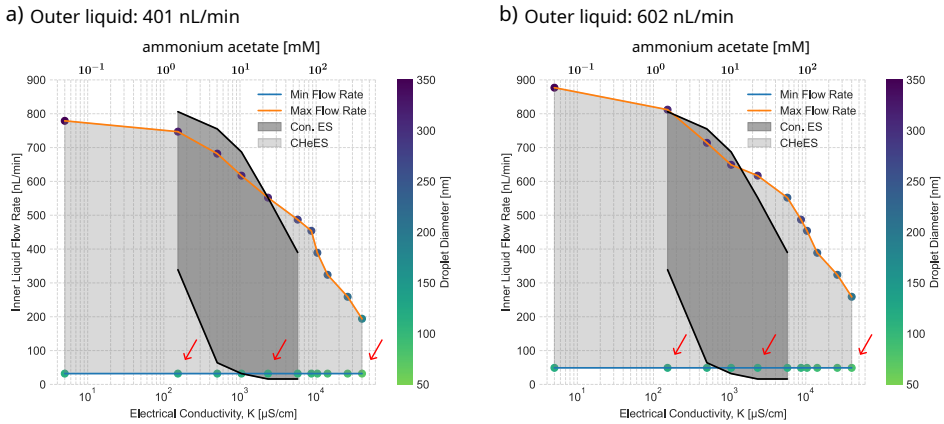

Figure 5.5: Conductivity range for effective aerosol generation by the CHeES injector. A wide spectrum of sample conductivities from 0 to 40000 μS/cm could be injected, exceeding the conventional electrospray system. Adjusting the outer liquid flow rates from (a) 401 nL/min to (b) 602 nL/min affected minimal and maximal flow rates for the inner fluid only marginally. Inner droplet sizes of 60-340 nm diameter were aerosolized in both cases, with an inverse correlation against sample conductivity. Three conditions covering low, mid and high conductivity regimes, here indicated by red arrows, were selected for a detailed core-shell analysis for both outer flow rates tested.

Droplet size quantification from SMPS measurements and equation 5.1 implicated inner liquid flows to contribute droplet volumes ranging from 60-340 nm in diameter, which are well suited for single particle imaging. Notably, identical liquid flows for more conductive samples yielded overall smaller droplets. This is consistent with the required between liquid surface tension and electric forces for Taylor cone stability, which necessitates a sufficiently large surface charge density that itself is compounded by the liquids conductivity.

Overall, the minimum inner liquid flow rate remained insensitive to a wide range of outer sheet liquid conductivities while being more sensitive to the outer liquid flow rates. We expect this to be due to threshold low inner liquid flow rate, below which the the outer liquid's pressure induces the inner liquid to flow backwards into the reservoir.

5.3.4 Core-shell analysis

We next set out to quantify contributions of inner and outer liquid jet to the generated aerosols by CHeES (Figure 5.6). For this, we focused on six conditions on the lower stable jetting limit - three each for the 401 and 602 nL/min outer liquid flow rate regime previously tested (Figure 5.5). For each combination of conductivity and flow

rate, we performed SMPS sucrose particle sizing after complete solvent evaporation. A 1% v/v sucrose solution was introduced in the inner liquid only (1), the outer liquid only (2) or into both (3) (See SI Table 5.3 for a complete list of conditions). From this the core diameter (1), the shell thickness (2) or the complete core-shell droplet (3) could be accessed. The smallest droplet diameter produced by CHeES was approximately 149 nm, with a core diameter of about 72 nm and a shell thickness of roughly 37 nm. Size dispersion for each experiment stayed below 5%. Furthermore, we noticed a good agreement between directly measured (3) and inferred (sum of 1 and 2) overall diameters (Figure 5.6c), confirming the stability and repeatability of the experiments.

a)

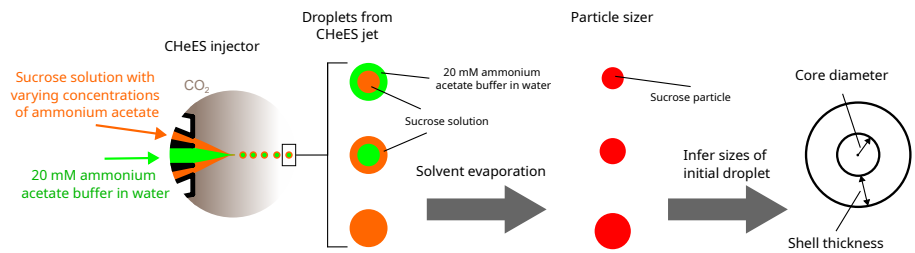

b)

Liquid flow rate (Inner/Outer) [nL/min]	Ammonium Acetate buffer background	Inferred initial droplet structure		
		Core diameter [nm]	Shell thickness [nm]	core-shell diameter [nm]
32/401	2 mM	116 ± 1.8	57 ± 2.1	237 ± 4.6
	20 mM	111 ± 1.6	54 ± 3.7	214 ± 4.3
	500 mM	72 ± 1	37 ± 2.3	149 ± 3.2
49/602	2 mM	120 ± 2.3	106 ± 7	334 ± 7.9
	20 mM	116 ± 2.3	98 ± 6	297 ± 6
	500 mM	83 ± 2.1	63 ± 4.6	208 ± 5.1

c)

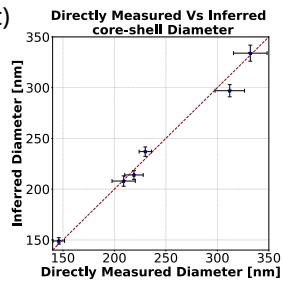

Figure 5.6: Detailed quantification of droplet structure produced by CHeES: (a) Three independent experiments were used to quantify a condition. Either, the inner core (top), outer sheet (middle) or both (bottom) portions of the jet are supplemented with sucrose for SMPS particle sizing after solvent evaporation. (b) For the six conditions tested, higher surface charge at the Taylor cone produces smaller droplets and thus smaller particles (see Table 5.3 in SI for additional experimental details). (c) Core-shell diameter quantified from separate experiments (inferred) or directly quantified showed very good agreement with each other.

5.3.5 Background Noise Reduction

Based on the previous CHeES injector characterization, we set out to quantify the achievable background noise reduction from a combined liquid-sheet plus gas-sheet configuration at the SPB/SFX instrument of the European XFEL. For simplicity, we prioritized to relate detector background noise between helium mode in a CHeES nozzle and nitrogen mode used with conventional electrospray nozzles (Table 5.1). The ideal liquid-sheet solution of 80 mM ammonium acetate in ethanol was used

to help deliver 55 nm silver nanocubes suspended in ethanol at a concentration of 1.16×10^{11} particles/mL. Due to a lack of charge carriers, this inner sample would fail to inject in a conventional electrospray nozzle [61], including our HeES injector [116] which features a similar sheet-gas, but lacks a sheet-liquid. The injected sample for the conventional ES hence combined ammonium acetate and silver cube concentrations distributed into both CHeES liquid lines into a single ethanol solution.

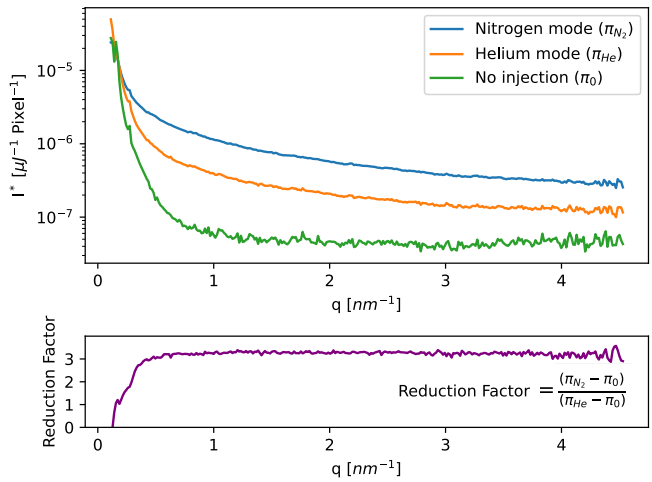

Figure 5.7: Comparative analysis of diffraction background radial profiles at the European XFEL SPB/SFX instrument. Throughout the varying scattering vectors (q), photon counts per μJ per pixel for helium mode (π_{He}) were lower then in nitrogen mode (π_{N_2}), but still noticeably higher then at steady state without injection (π_0). The background noise reduction for helium compared to nitrogen was quantified as I_{rel} = 3.244 $\pm$ 0.075.

The residual gas analyzer in the SPB/SFX chamber measured concentrations of heavier gases to reduce 3.5 fold for N_2 and 2.2 fold for CO_2 in helium mode with the respective gas-sheet flow. Further more, radial profiles of background scattering patterns measured a background noise reduction factor I_{rel} = 3.244 $\pm$ 0.075 (Figure 5.7). This decrease is consistent with the reduced gas scattering cross-section expected in helium (new) over nitrogen (old) mode. Elastic scattering from a gas molecule is proportional to the square of its number of electrons, Z. The chamber atmosphere can then be considered to be the weighted sum over all gas species in the mixture and the background noise reduction factor can be estimated as:

$$I_{rel} \sim \frac{p^{\text{new}}_{He} Z^2_{He} + p^{\text{new}}_{N_2} Z^2_{N_2} + p^{\text{new}}_{CO_2} Z^2_{CO_2}}{p^{\text{old}}_{N_2} Z^2_{N_2} + p^{\text{old}}_{CO_2} Z^2_{CO_2}}, \tag{5.3}$$

with SPB/SFX chamber partial gas pressures, p_gas, of 2.4×10^{-6}, 2×10^{-6}, $7.7 \times$

10^{-7} Torr for He, N_2, CO_2 in helium mode and 7.1×10^{-6}, 1.7×10^{-6} Torr for N_2, CO_2 respectively in conventional ES, we approximate $I_{rel} \sim 0.3$ corroborating our earlier diffraction pattern based background reduction measurement.

Both, configurations achieved a hit rate of approximately 4%, indicating that the CHeES system can match the conventional ES system in particle transmission efficiency to the interaction chamber. However, an accurate experimental comparison in this regard is inherently difficult, as smallest alignment and focus drifts of the nanometer X-ray beam or minute gas flow obstructions from sample depositions along the injection system can quickly deteriorate signal. A detailed analysis of collected silver cube diffraction signal quality will be reported elsewhere.

5.4 Conclusion

We combined a coaxial liquid-sheet and gas-sheet into an electrospray nozzle, called CHeES. Implemented as a precision 3D printed part, the potential for CHeES to improve SPI in several ways could be demonstrated experimentally. Over all, CHeES could form core-shell droplets as small as ∼149 nm in dimeter, consisting of a core of ∼72 nm and a shell thickness of ∼37 nm, which are suitable for SPI and comparable to the smallest droplet diameter generated by conventional ES [44].

The previously explored helium gas-sheet injection concept [116], could for the first time be validated in diffraction experiments to realize a diffraction background reduction and hence signal-to-noise improvement by a factor of more then tree fold. Further optimizing the gas-sheet in the future may help reduce parasitic gas loads in the experimental chamber. For instances, a Laval nozzle taper may help reduce radial dissipation of the gas sheet to further reduce heavy gas injection [135].

Even more fascinating is the prospect of de-coupling liquid sample buffer composition from the electro spray ionization process, afforded by the liquid-sheet. Samples ranging in conductivity from zero up to 40,000 μS/cm were readily injected without compromising the stability of the Taylor cone. Consequently many more samples can now qualify for electrospray based SPI, such as biological macromolecules that are only stable at very low or high ionic strength outside of the conventional electrospray parameter space. Also, organic and inorganic samples with narrow non-polar solvent requirements can now be explored, such as for instances select perovskites [136].

Future work should analyze mixing between both liquids forming the Taylor cone in more detail. Considering the volume of the Taylor cone and the applied flow rates, we estimate the average residence time of liquid in the cone to be of order 0.1-0.4 ms and

hence comparable to the sheet jet formation in the double flow focusing nozzles [56]. Ammonium acetate or ethanol with a diffusion coefficient in water of order 10^{-9} m^2/s diffuses a distance of 0.5-1 μm during this time span [137]. Accordingly, significant mixing can be expected in submicron diameter jets. Furthermore, circulation eddies have been reported to occur in the Taylor cone tip [138], possibly resulting in more complex mixing patterns.

Qualification of new samples for CHeES will hence likely require extensive prior testing to identify optimal sample buffer and liquid-sheet conditions. For example, when a biological macromolecules is sensitive to ethanol, an optimal low-ethanol or even ethanol-free sheet-liquid has to be identified first. Such validation work should confirm sample integrity via transmission electron microscopy after spraying [44, 139]. In turn, time-resolved mixing experiments may benefit from increased mixing through dedicated 3D micromixer structures [46]. With these aspects CHeES may also help advance other imaging modalities, such as for instances electrospray assisted electron microscopy [139].

5.5 Acknowledgements

We thank Agnieszka Wrona for assistance with nozzle assembly and Vasilii Bazhenov for support and discussions on sample preparation. We acknowledge the support of the SPB/SFX staff at the European XFEL in operating the instrument during proposal 6056, where the gas background was collected.

5.6 Supplementary Materials

5.7 Sample and Buffer Preparation

To prepare the ethanol-based buffer, we first made a 500 mL stock solution with 0.5 M ammonium acetate. This stock was then diluted with ethanol to achieve ammonium acetate concentrations ranging from 20 to 120 mM. For the water-based buffer, we prepared a 500 mL stock solution with 1 M ammonium acetate and diluted it with water to create concentrations ranging from 2 to 500 mM. Each concentration of the water-based buffer was then split in two: one portion was left unmodified, while the other had 1% (v/v) sucrose added to create sucrose-containing samples across the same concentration range. Additionally, we prepared a 1% sucrose solution in ultrapure water without ammonium acetate.

5.8 Experimental Setup

Table 5.2: He-mode and N_2-mode operations for CHeES and HeES systems.

	CHeES		HeES	
Parameter	He-mode	N_2-mode	He-mode	N_2-mode
He flow rate (L/min)	3	–	4.2	–
N_2 flow rate (L/min)	0.06	1	0.03	1
CO_2 flow rate (L/min)	0.03	0.13	0.015	0.2
Voltage range (V)	1650 – 1950	1800 – 2100	2200 - 2600	NA
Buffer flow rate (nL/min)	≈433	≈433	100 - 200	100 - 200

5.9 CHeES Design

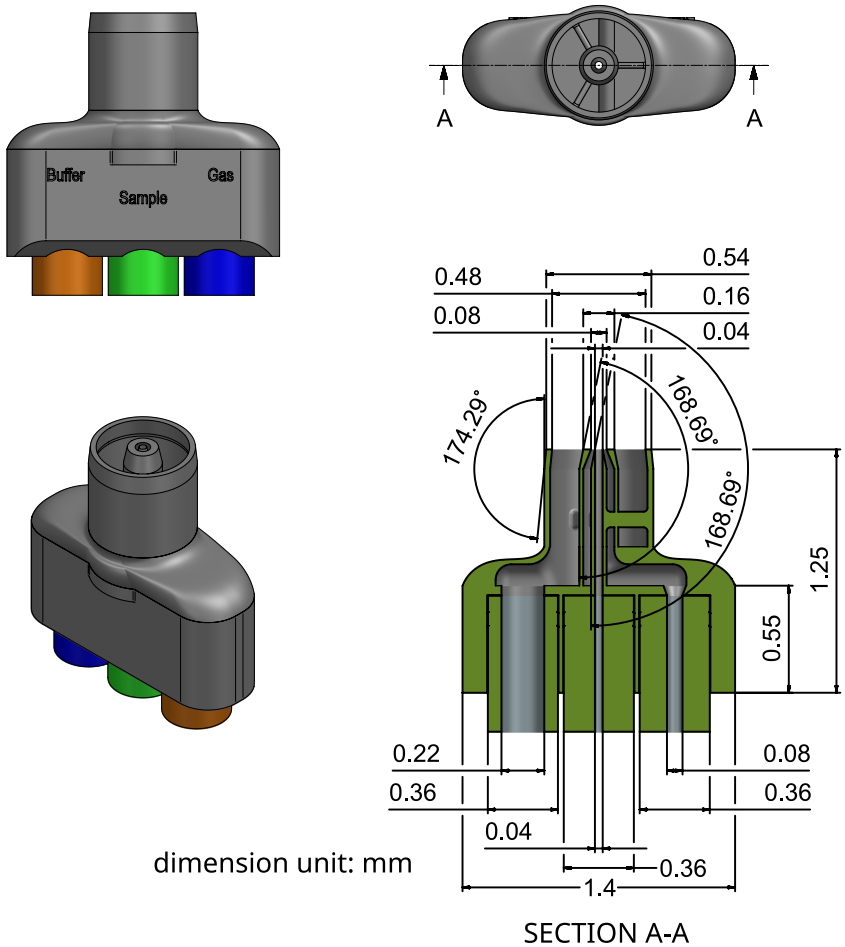

Figure 5.8: CHeES nozzle design. Renderings and technical drawing to nozzle dimensions, inlets, and outlets. Dimensions in milimeter.

5.10 Liquid sheet formation and conductivity range quantification

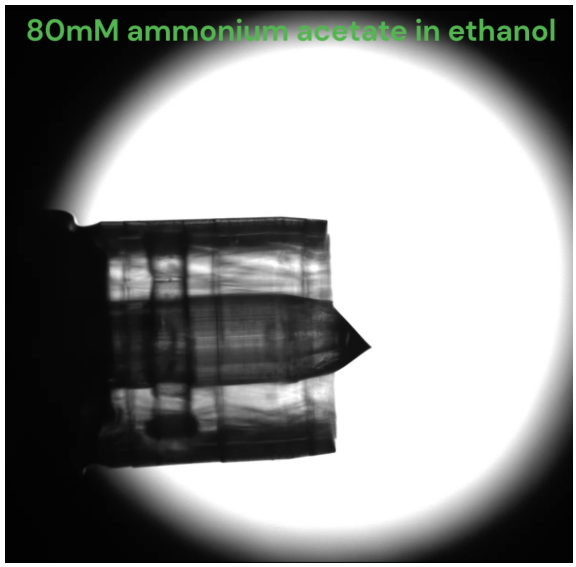

Figure 5.9: SI Movie 1: Taylor cone stability using a 401 nL/min flow of ammonium acetate in ethanol at concentrations of 20, 80, and 120 mM. The 80 mM sheet demonstrated the highest stability and most effective aerosol generation.

5.11 Simulations of Gas Flow Around the Taylor Cone

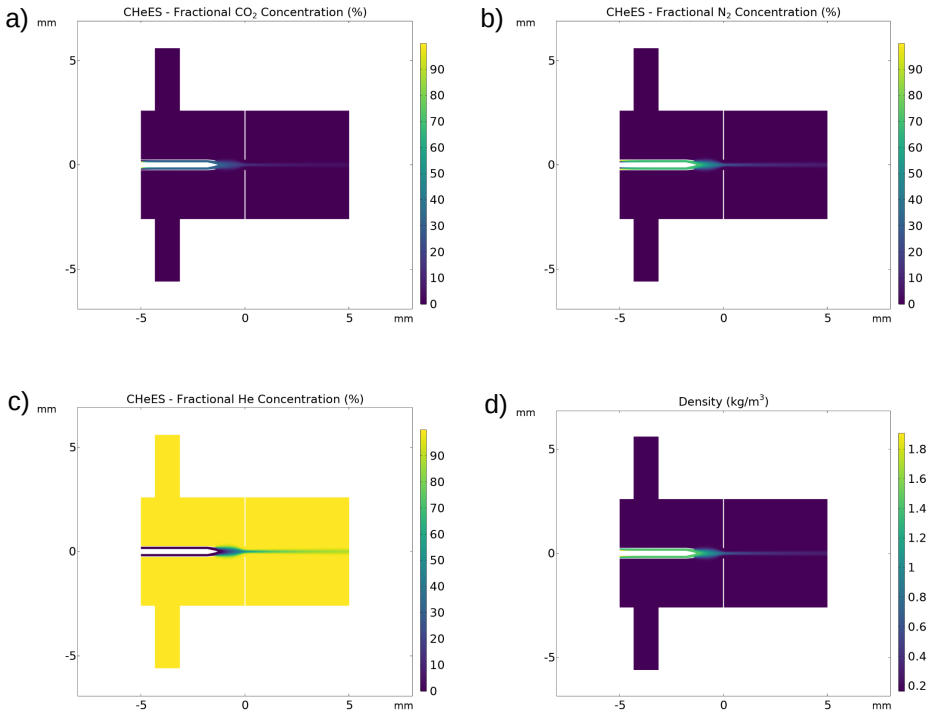

Figure 5.10: The fractional gas concentrations in the aerosolization and neutralization chambers within the CHeES system. a) The fractional concentration of CO2, b) N2, and c) He, respectively, while d) is the gas density.

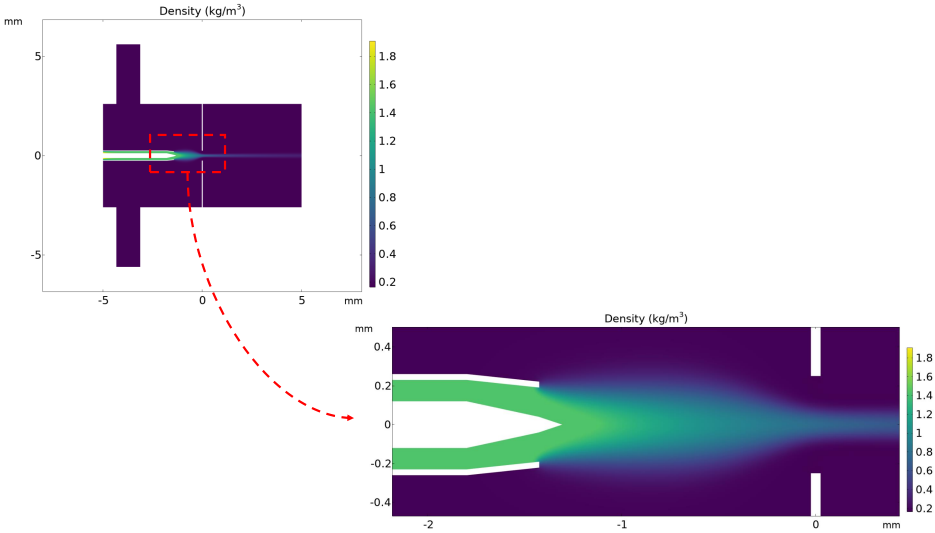

Figure 5.11: The gas density in the aerosolization and neutralization chambers within the CHeES system, with a zoom-in on the area around the Taylor cone.

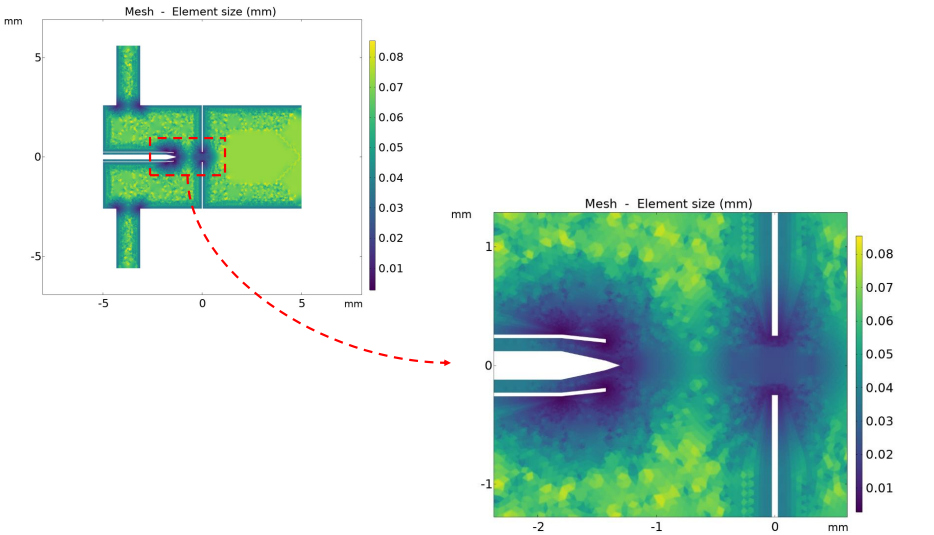

Figure 5.12: The element size of the mesh in the aerosolization and neutralization chambers within the CHeES system, with a zoom-in on the area around the Taylor cone.

5.12 Conductivity range quantification

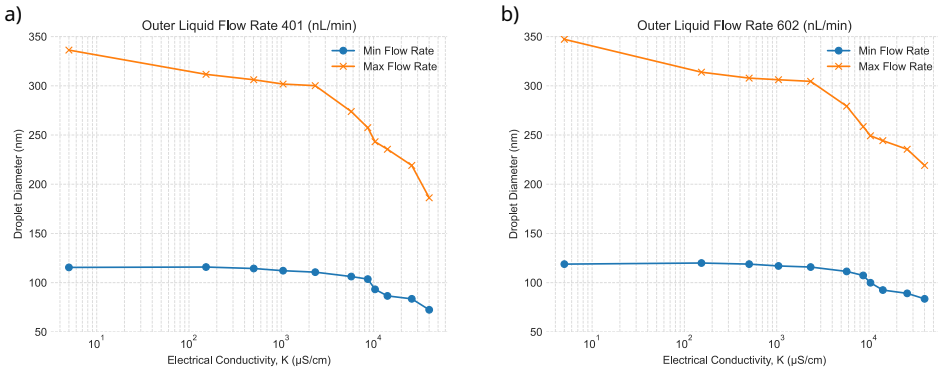

Figure 5.13: Droplet size as a function of conductivity, showing a decrease in droplet size with increasing conductivity: (a) with an outer liquid flow of 401 nL/min, and (b) with an outer liquid flow of 602 nL/min.

5.13 Core-shell Analysis

Table 5.3: Inference of droplet structure produced by the CHeES system following the procedure of the core-shell analysis from Figure 5.6 Using the six marked conditions from Figure 5.5, we infer the core diameter, shell thickness, and core + shell diameter of the droplets. The table shows that higher surface charge at the Taylor cone produces smaller droplets and thus smaller particles.

Ammonium Acetate	Inner liquid		Outer liquid		Measured particle	Inferred particle diameter [nm]		
buffer background	Sucrose	Flow rate [nL/min]	Sucrose	Flow rate [nL/min]	diameter [nm]	Core diameter [nm]	Shell thickness [nm]	Entire droplet diameter [nm]
	1 wt%		—		25 ± 0.38	116 ± 1.8	—	—
2 mM	—	32	1 wt%	401	47.6 ± 0.45	—	57 ± 2.1	—
	1 wt%		1 wt%		51.1 ± 1	—	—	237 ± 4.6
	1 wt%		—		23.8 ± 0.35	111 ± 1.6	—	—
20 mM	—	32	1 wt%	401	45.2 ± 0.8	—	54 ± 3.7	—
	1 wt%		1 wt%		48.4 ± 0.93	—	—	214 ± 4.3
	1 wt%		—		15.6 ± 0.22	72 ± 1	—	—
500 mM	—	32	1 wt%	401	30.4 ± 0.5	—	37 ± 2.3	—
	1 wt%		1 wt%		32.1 ± 0.7	—	—	149 ± 3.2
	1 wt%		—		25.8 ± 0.5	120 ± 2.3	—	—
2 mM	—	49	1 wt%	602	70.3 ± 1.5	—	106 ± 7	—
	1 wt%		1 wt%		72.9 ± 1.7	—	—	334 ± 7.9
	1 wt%		—		25 ± 0.5	116 ± 2.3	—	—
20 mM	—	49	1 wt%	602	66.1 ± 1.3	—	98 ± 6	—
	1 wt%		1 wt%		68.6 ± 1.3	—	—	297 ± 6
	1 wt%		—		18 ± 0.45	83 ± 2.1	—	—
500 mM	—	49	1 wt%	602	44.2 ± 1	—	63 ± 4.6	—
	1 wt%		1 wt%		46.5 ± 1.1	—	—	208 ± 5.1

Chapter 6

Looking Back, Moving Forward: Achievements and Future Opportunities

6.1 Achievements

A significant bottleneck in the ES-based gas phase injection system, as previously discussed in the Introduction, includes low particle transmission, considerable background noise from gas scattering, and limitations in the range of sample conductivities that can be effectively sprayed [13]. These limitations have consequentially impeded the resolution, quality, and volume of data attainable in single-particle imaging at XFEL facilities. The work presented in this thesis has addressed these challenges by developing new methodologies and technologies to improve the performance of ES-based gas phase injector systems. It proposes solutions to increase particle transmission efficiency [61], reduce background noise [116], and broaden the sample conductivity range.

Moreover, the contributions of this thesis are not limited to the technical improvements of injection systems. They also extend to the broader scientific community engaged in the quest to unravel the complex structures of biological entities. We anticipate that these contributions will significantly enhance the accurate and high-resolution imaging of nanoparticles and biomolecules, including proteins, by leveraging the unparalleled capabilities of XFELs [27, 37]. This advancement is expected to pave the way for groundbreaking research opportunities, fostering a deeper understanding of the microscopic entities in terms of their structural and functional prop-

erties. This understanding is crucial for scientific advancements in various scientific domains, including but not limited to, biochemistry, pharmacology, and materials science [12].

The following sections summarize the approach to the previous challenges, highlight the key findings and contributions of this work, and discuss their implications for the field of single-particle imaging and related research areas.

6.1.1 Optimizing Efficiency in Particle Transmission

The current ES-based system's inefficiencies stem mainly from the charged nature of the particles it produces, leading to significant losses. These particles, repelling each other due to their like charges and being attracted to the system's grounded surfaces, often fail to effectively traverse the system. Instead, they are deposited on the counter electrode's orifice plate [66].

To address this issue, our investigation embarked on a methodical examination of various factors affecting the performance of ES-based systems. Recognizing the pivotal role of neutralizers in particle neutralization, we explored the efficacy of different types, including VUV, soft X-ray, and polonium-210 (^{210}Po), in enhancing particle transmission efficiency [83, 114]. Concurrently, we delved into the impact of altering the geometry of the ES setup, aiming to identify configurations that could minimize particle loss. This exploration, however, was not without its constraints. The limitations imposed by gas flow rates, particularly critical in the context of SPI experiments, necessitated a balanced approach. Our endeavors to optimize the system were thus guided by a dual focus: achieving a high level of efficiency while ensuring the practical applicability of our solutions for SPI experiments [44].

Our experiments across various system configurations revealed the VUV ionizer as a superior alternative to the traditionally used soft X-ray ionizer, achieving a sevenfold increase in transmission efficiency over previous setups. Additionally, optimizing the orifice size on the counter electrode, in combination with the VUV ionizer, led to a more than 40% particle transmission efficiency from solution to the X-ray interaction region.

These advancements significantly enhance data collection for high-resolution structural determination. The notable increase in transmission efficiency translates into a higher quantity of high-quality diffraction patterns. Such an abundance of data is crucial for achieving high-resolution structural determinations, meeting the primary goal of facilitating statistically significant data collection from individual nanoparticles, including biomolecules [17, 122, 129]. Improved transmission efficiency not only

boosts the quality of the final 3D reconstructions but also optimizes the use of experimental resources and time. This makes the research process more efficient and cost-effective. Moreover, the successful implementation of the VUV ionizer increases its availability to the research community. It does so by mitigating the safety concerns associated with the use of polonium-210 (^{210}Po) sources or soft X-ray ionizers, thereby making the system more accessible and user-friendly for implementation in XFEL facilities worldwide.

6.1.2 Minimizing Gas Scattering-Induced Background Noise

The challenge of high background noise caused by the scattering of gases (N_2 and CO_2), which leads to low-quality diffraction patterns, can be addressed by using lighter gas such as He as the primary gas for particle transport [27]. He, with its notably low atomic number, is preferred over hydrogen (H_2) for safety considerations. However, employing He alone in the aerosolization chamber can induce corona discharge and potentially collapse the Taylor cone. To mitigate the risk of corona discharge and safeguard the Taylor cone, a controlled mixture of N_2 and CO_2 gases can be utilized [66].

To overcome this challenge, we introduced the He-ESI system. At the heart of this innovation is a 3D-printed nozzle, which is designed to reduce the presence of N_2 and CO_2 by approximately 83% compared to traditional ES while maintaining a stable Taylor cone. Moreover, the successful integration of the He-ESI system with the "Uppsala" injector marks a significant enhancement in injection yield, especially for small biological particles, by approximately a tenfold increase.

These advancements significantly enhance our research objectives, opening new research directions and applications. This is particularly relevant for samples previously characterized by low signal-to-noise ratios [12]. The ability to generate high-quality diffraction patterns now facilitates high-resolution 3D reconstruction of small nanoparticles, especially those of small biomolecules (below 50 nm). This capability unveils novel avenues for scientific investigation, enabling researchers to explore the structural and functional properties of a broader range of biological systems with unprecedented detail. Such insights hold wide-ranging implications, potentially driving progress in diverse fields such as pharmacology, materials science, and energy. For example, a deeper understanding of material structures at the atomic level could catalyze the development of more efficient technologies for energy storage and conversion [2, 15].

6.1.3 Broadening the Sample Conductivity Spectrum

One of the primary challenges is the narrow range of sample conductivities suitable for efficient ES [66], compounded by the need to minimize background noise. This constraint stems from the fundamental principle of ES, in which sample conductivity is critical to the formation of the Taylor cone—a state where electrostatic forces on the liquid surface outweigh its surface tension [76, 77]. A potential solution is to create the Taylor cone using a separate conductive buffer solution, then introduce the sample to be sprayed from this Taylor cone [132].

We developed a CHeES system for SPI at XFELs, capable of handling a wide range of sample conductivities. CHeES combines He-ES with coaxial electrospray technology to improve sample delivery, ensuring stable delivery and optimal droplet size for SPI at XFELs. It significantly reduces background noise by lowering N_2 and CO_2 levels in the interaction area, decreasing them by factors of 3.5 and 2.2, respectively. CHeES can spray samples from non-conductive to highly conductive (up to 40000 µS/cm), enhancing the range of samples that can be analyzed. Its application with the "Uppsala" injector at the EuXFEL's SPB instrument demonstrates that its injection yield is on par with traditional electrospray systems [44].

These advancements significantly contribute to the research's overarching goals by broadening the spectrum of analyzable samples and enhancing data quality. The novel sample delivery system is capable of handling a wider variety of sample types, including biological samples and inorganic nanoparticles. This increased versatility allows for an expanded range of sample types to be effectively studied, with minimal modifications required to preserve their structural integrity. When combined with enhanced transmission efficiency techniques, these optimized delivery systems can notably improve both the quality and quantity of data collected during XFEL experiments. Such advancements are not merely technical; they also provide substantial benefits to the scientific community, thereby expanding the scope of research and potential discoveries within structural biology and related fields [12].

6.2 Future Opportunities

While we have achieved significant improvements in the system's performance, several limitations still need to be addressed in future research. Notably, although we have enhanced the particle transmission efficiency, the system exhibits lower transmission efficiency for lighter and smaller particles. This issue may stem from increased losses at the skimmer stages for these smaller and lighter particles. To address this, future work could focus on a deep dive into the mechanics of particle loss at these

stages [140]. By harnessing Computational Fluid Dynamics (CFD) and advanced simulation techniques, researchers can explore new geometries for the skimmer that minimize turbulence and optimize the flow path for these smaller particles, thereby enhancing transmission efficiency [141]. This could involve the development of adaptive skimmer designs that dynamically adjust based on the particle size distribution of the sample.

In the He-ES system, laboratory results demonstrated a notable reduction in the heavier gas load entering the interaction chamber—approximately 81%. However, initial tests at the SPB endstation at XFEL reported a lesser reduction, around 66%, and a background noise reduction by roughly threefold. This discrepancy could be attributed to differences in the experimental setups, possibly exacerbated by leaks that increased the gas scattering background more than expected. Such a reduction may still not suffice for experiments requiring extremely low background noise, like those involving small, light biological particles, to obtain high-resolution structures [27]. To address this challenge, further refinement in both the nozzle designs and the overall system setup, coupled with baking the interaction chamber to eliminate heavier gases, can reduce background noise further. The proposed baking process, followed by filling the chamber with He, serves a dual purpose: it purges the chamber of contaminants and optimizes the environment for lighter, small biological particles [142]. Additionally, refining the catcher geometry could ensure the efficient capture of heavier gases upon injection, thereby reducing the potential for noise-inducing interactions [3].

In the CHeES system, droplet size was larger than in traditional electrospray systems within certain conductivity ranges due to the minimum inner flow limit before the outer flow completely blocks it. This limit results in larger droplets for specific conductivity ranges, potentially increasing contamination risk for samples [44]. To address this, the nozzle design can be refined to operate with a lower inner flow rate, producing smaller droplets. This approach minimizes the sample's exposure to potential contaminants, thereby preserving its integrity for high-precision experiments.

Future opportunities, such as addressing sample degradation during experiments, implementing periodic sonication to maintain sample conditions, and increasing the hit rate by raising particle density at the intersection with the X-ray, will be discussed in more detail below. Additionally, integrated systems to address these opportunities will be proposed.

6.2.1 In-situ In-line Monitoring System

To address sample degradation during experiments, it is essential to incorporate optical techniques, sensor technology, and real-time data analytics into a in-situ, in-line

monitoring system. A practical approach includes an inline Rayleigh scattering setup, similar to the method introduced by [63], positioned after the skimmer stages. This system offers instant feedback on sample quality and transmission efficiency through the monitoring of particle physical characteristics. By measuring the intensity of scattered light, it detects variations in particle number, size, or composition that signal degradation.

Developing this system involves:

- Understanding Rayleigh Scattering: This phenomenon, where light scatters off particles smaller than the light wavelength, is sensitive to particle size, concentration, and refractive index, making it suitable for sample integrity monitoring [143].
- Designing the Inline Setup: Incorporates a pulsed laser, optical components to direct and focus the laser beam through the sample stream, and detectors to capture scattered light. Considerations include a stable, fiber-coupled nanosecond pulsed laser; an optical path designed to intersect the particle beam with minimal stray light; and high-sensitivity detectors, like CMOS cameras, for capturing low-intensity light.
- Integration with Skimmers: The setup must be compact and compatible with existing skimmer stages to minimize disruption.
- Data Acquisition and Analysis: Requires developing real-time systems for processing detector signals and analyzing data using algorithms or statistical models to detect sample degradation signs [144].
- Feedback Loop for Quality Management: Enables immediate corrective actions through automatic adjustments or operator alerts, such as modifying the sample flow rate or applying sonication to prevent aggregation.

Combining a compact design with a sufficient signal-to-noise ratio poses significant challenges, especially for detecting small particles. A monitoring system with broad applicability requires a compact, portable, and easy-to-set-up design, necessitating the delivery of a laser beam through an optical fiber. This requirement can limit the laser intensity and, consequently, the signal-to-noise ratio. Selecting the appropriate optical fiber involves a trade-off: single-mode fibers can deliver a high-quality beam with excellent focus but at lower power, while multimode fibers can deliver higher power but produce a beam of lower quality that is challenging to focus accurately [145]. Additionally, stray light poses another challenge, potentially impacting the signal-to-noise ratio and necessitating meticulous measures to minimize its effects. The integration

of a compact infinity-corrected objective lens and a camera as the detector can constrain the system's resolution and sensitivity, thereby limiting the detection of the smallest particle sizes. Furthermore, physical integration presents spatial arrangement challenges and necessitates ensuring that the system's addition does not introduce unwanted perturbations to the sample flow or alter the overall experimental procedure.

6.2.2 Piezo-based Sonication System

The necessity for periodic sonication to maintain sample condition introduces complexities in the operation of sample delivery and can impact the overall throughput of experiments by consuming valuable time for periodic sample maintenance. Integrating a piezo-based sonication system directly into the sample delivery setup, where the samples are held in Eppendorf tubes, offers a seamless solution to this challenge. This approach not only streamlines the sample delivery process but also ensures that the sample remains in optimal condition, preventing particle aggregation and ensuring uniformity throughout the experiment. Additionally, it enables remote control and adjustment of the sonication parameters as needed.

This guide outlines integrating a sonication system:

- Piezoelectric Transducers: The core of the sonication system consists of piezoelectric transducers that are capable of converting electrical signals into mechanical vibrations, thereby producing ultrasonic waves. A wide range of transducers is available that can generate the required frequency and intensity of ultrasonic waves for effective sonication of the samples, typically using frequencies between 30kHz to 80kHz for sonication applications [146].

- Sample Holder Adaptation: The sample holder, designed to accommodate Eppendorf tubes, should be modified to ensure efficient transmission of ultrasonic waves. This may involve incorporating materials that efficiently conduct ultrasonic vibrations while ensuring compatibility with the existing experimental setup.

- Medium for Ultrasonic Wave Transmission: A crucial aspect of the design is selecting a medium capable of effectively transmitting ultrasonic waves from the transducers to the samples. While water is commonly used due to its excellent transmission properties, a gel-based medium, such as a sonication gel, may be more appropriate for Eppendorf tube applications. This medium should encapsulate the lower part of the Eppendorf tube, ensuring direct contact with the tube without requiring the samples to be immersed in a liquid that could potentially contaminate them [146].

- Remote Control and Adjustment: Implementing a control system that allows for the remote adjustment of sonication parameters (frequency, duration, and intensity) is critical. This flexibility ensures that the sonication can be tailored to the specific needs of different samples, improving the system's utility across a wide range of experiments.

However, challenges including sample integrity are paramount; the sonication process must avoid overheating or negatively impacting delicate samples [147]. The sonication system also needs to integrate seamlessly with current experimental setups, including operational workflows. Additionally, if an in-situ inline monitoring system is available, it can offer real-time feedback on sonication effectiveness, permitting necessary adjustments.

6.2.3 Piezo-based Acoustic Levitation System

For the manipulation of lighter and smaller particles, the development of a piezo-based system—utilizing acoustic levitation to convert a particle beam into a bunched particle beam—emerges as an innovative solution [148]. This method holds the potential to significantly increase particle density at the interaction point with the XFEL beam, thereby enhancing hit rates. By leveraging the precise control afforded by acoustic levitation, the system can synchronize particle delivery with the XFEL beam, optimizing their interaction and maximizing data collection. The following is a detailed exploration of how such a system can be realized and implemented, with a particular focus on integration with the aerodynamic lens stack.

Acoustic levitation, the foundational principle, employs sound waves to suspend particles in air or gas, countering other forces with a pressure field generated by the sound waves [149]. This field creates nodes, where there is no movement, allowing particles to be trapped and held in place. By finely modulating these sound waves, the system can manipulate the position and density of particles with great precision. A piezo-based system utilizes piezoelectric materials, which deform under electric voltage, to produce exact sound waves necessary for effective acoustic levitation and particle manipulation.

The system's design includes:

- Piezoelectric Transducers: Convert electrical signals into mechanical vibrations for levitation, tailored for specific particle sizes [146].
- Acoustic Chamber: Precisely controls the acoustic field for effective particle bunching, aligned with the aerodynamic lens stack for synchronized delivery

with the XFEL beam.

- Control System: Modulates transducers for real-time beam density and distribution adjustments.

However, challenges such as varying particle size and composition affect levitation effectiveness, necessitating tailored system adjustments. Fortunately, acoustic levitation is highly effective for levitating smaller, lighter particles, making it an ideal solution for our needs. Smaller objects are more easily levitated due to their lower weight requiring less force for levitation. As objects increase in size and weight, the power and precision needed for levitation also significantly increase [149]. Minimizing beam dispersion and ensuring the piezo-system's compatibility with the experimental setup, especially the aerodynamic lens stack and XFEL beam pathway, are crucial considerations.

6.2.4 Electrostatic Particle Bunching System

To enhance the sample delivery of smaller and lighter particles, a system utilizing electrostatic particle bunching can be developed to manipulate slightly charged particles [83]. This system leverages electrostatic forces to bunch particles into a dense particle pulse, enhancing interaction rates with an XFEL beam. Here, we outline the concept, development, and integration of this system, with a focus on its compatibility with existing delivery systems and experimental setups.

The core principle of this system, electrostatic levitation, employs electric fields to manipulate and suspend charged particles [150]. By applying variable electric potentials, it can create electric fields that adjust the position of charged particles and bunch them effectively. The key components of the system include:

- Electrostatic Generators: Create and control electric fields necessary for levitation and manipulation of charged particles.
- Bunching Chamber: Manages the electrostatic fields to cluster particles effectively, ensuring their precise delivery aligned with XFEL beam timing [150].
- Control System: Dynamically adjusts electric fields in real-time to optimize particle density and distribution for interaction with the XFEL beam.

However, several challenges arise, including the system's dependence on particle charge and the need for precise voltage control, which may complicate system calibration.

Furthermore, the effectiveness of electrostatic levitation decreases as particle size increases, requiring stronger electric fields for effective manipulation. Nevertheless, the system offers significant advantages for manipulating mono-disperse, smaller, lighter, like-charged particles.

6.2.5 Long-Term Development Prospects

The exploration of entirely new delivery concepts, such as a hybrid system that combines electrospray with optical tweezers, presents an exciting frontier for particle delivery mechanisms. This system not only focuses the particle beam but also controls the orientation of particles. Incorporating optical tweezers involves employing a highly focused laser beam to trap and manipulate particles [151–153]. The force exerted by the laser beam can attract or repel particles, enabling precise control over their position, which is particularly useful for directing particles to specific locations. Additionally, this method helps to minimize the amount of gas accompanying the particles, which is responsible for focusing the particle beam, reduces background scattering, and improves the signal-to-noise ratio in imaging experiments. The integration of optical tweezers with electrospray provides a unique solution to the challenges of particle orientation and alignment, along with further reduction in background noise.

Finally, the exploration of new materials for nozzle fabrication could lead to minimize nozzle clogging, further improving the overall performance of the system and reducing the time required for cleaning and maintenance [98, 154, 155]. Moreover, the integration of machine learning for real-time adjustment of delivery parameters offers a solution to optimize experimental conditions dynamically [156]. Machine learning algorithms can analyze data in real time to adjust parameters such as flow rate, particle density, and sonication intensity, ensuring optimal conditions for each experiment.

The advancements made through this research highlight the importance of interdisciplinary efforts, combining physics, chemistry, biology, and engineering to push the boundaries of what is possible in scientific imaging. This collaborative approach can inspire further innovations in sample delivery systems and imaging techniques, leading to broader applications across various scientific domains and pushing the boundaries of what is possible.

References

[1] C.-I. Branden and J. Tooze. *Introduction to Protein Structure*. Garland Science, 2nd edition, 1999.

[2] U. Bergmann, V.K. Yachandra, J. Yano, and Royal Society of Chemistry, editors. *X-ray free electron lasers: applications in materials, chemistry and biology*. Number 18 in Energy and environment series. Royal Society of Chemistry, London, 2017.

[3] F. Boscherini, C. Meneghini, and S. Mobilio, editors. *X-ray free electron lasers: a revolution in structural biology*. Springer International Publishing, Cham, 1st edition edition, 2018.

[4] I. Schlichting. Serial femtosecond crystallography: the first five years. *IUCrJ*, 2 (2):246–255, 2015.

[5] R. Neutze, R. Wouts, D. Van der Spoel, E. Weckert, and J. Hajdu. Potential for biomolecular imaging with femtosecond x-ray pulses. *Nature*, 406(6797): 752–757, 2000.

[6] I. Grguraš, A.R. Maier, C. Behrens, T. Mazza, T.J. Kelly, P. Radcliffe, S. Düsterer, A.K. Kazansky, N.M. Kabachnik, Th. Tschentscher, J.T. Costello, M. Meyer, M.C. Hoffmann, H. Schlarb, and A.L. Cavalieri. Ultrafast x-ray pulse characterization at free-electron lasers. *Nature Photonics*, 6(12):852–857, 2012.

[7] H.F. Lodish. *Molecular cell biology*. W.H. Freeman-Macmillan Learning, New York, eighth edition edition, 2016.

[8] J.C.H. Spence, U. Weierstall, and H.N. Chapman. X-ray lasers for structural and dynamic biology. *Reports on Progress in Physics*, 75(10):102601, 2012.

[9] H.N. Chapman, P. Fromme, A. Barty, T.A. White, R.A. Kirian, A. Aquila, M.S. Hunter, J. Schulz, D.P. DePonte, U. Weierstall, R.B. Doak, F.R.N.C.

Maia, A.V. Martin, I. Schlichting, L. Lomb, N. Coppola, R.L. Shoeman, S.W. Epp, R. Hartmann, D. Rolles, A. Rudenko, L. Foucar, N. Kimmel, G. Weidenspointner, P. Holl, M. Liang, M. Barthelmess, C. Caleman, S. Boutet, M.J. Bogan, J. Krzywinski, C. Bostedt, S. Bajt, L. Gumprecht, B. Rudek, B. Erk, C. Schmidt, A. Hömke, C. Reich, D. Pietschner, L. Strüder, G. Hauser, H. Gorke, J. Ullrich, S. Herrmann, G. Schaller, F. Schopper, H. Soltau, K.-U. Kühnel, M. Messerschmidt, J.D. Bozek, S.P. Hau-Riege, M. Frank, C.Y. Hampton, R.G. Sierra, D. Starodub, G.J. Williams, J. Hajdu, N. Timneanu, M.M. Seibert, J. Andreasson, A. Rocker, O. Jönsson, M. Svenda, S. Stern, K. Nass, R. Andritschke, C.-D. Schröter, F. Krasniqi, M. Bott, K.E. Schmidt, X. Wang, I. Grotjohann, J.M. Holton, T.R.M. Barends, R. Neutze, S. Marchesini, R. Fromme, S. Schorb, D. Rupp, M. Adolph, T. Gorkhover, I. Andersson, H. Hirsemann, G. Potdevin, H. Graafsma, B. Nilsson, and J.C.H. Spence. Femtosecond x-ray protein nanocrystallography. *Nature*, 470(7332): 73–77, 2011.

[10] M.K. Eseev, V.I. Matveev, and D.N. Makarov. Diagnostics of nanosystems with the use of ultrashort x-ray pulses: Theory and experiment (brief review). *JETP Letters*, 114(7):387–405, 2021.

[11] L. Young, K. Ueda, M. Gühr, P.H. Bucksbaum, M. Simon, S. Mukamel, N. Rohringer, K.C. Prince, C. Masciovecchio, M. Meyer, A. Rudenko, D. Rolles, C. Bostedt, M. Fuchs, D.A. Reis, R. Santra, H. Kapteyn, M. Murnane, H. Ibrahim, F. Légaré, M. Vrakking, M. Isinger, D. Kroon, M. Gisselbrecht, A. L'Huillier, H.J. Wörner, and S.R. Leone. Roadmap of ultrafast x-ray atomic and molecular physics. *Journal of Physics B: Atomic, Molecular and Optical Physics*, 51(3):032003, 2018.

[12] J. Bielecki, F.R.N.C. Maia, and A.P. Mancuso. Perspectives on single particle imaging with x rays at the advent of high repetition rate x-ray free electron laser sources. *Structural Dynamics*, 7(4):040901, 2020.

[13] Z. Sun, J. Fan, H. Li, and H. Jiang. Current status of single particle imaging with x-ray lasers. *Applied Sciences*, 8(1):132, 2018.

[14] W. Decking, S. Abeghyan, P. Abramian, A. Abramsky, A. Aguirre, C. Albrecht, P. Alou, M. Altarelli, P. Altmann, K. Amyan, et al. A mhz-repetition-rate hard x-ray free-electron laser driven by a superconducting linear accelerator. *Nature photonics*, 14(6):391–397, 2020.

[15] E.J. Jaeschke, S. Khan, J.R. Schneider, and J.B. Hastings, editors. *Synchrotron light sources and free-electron lasers: accelerator physics, instrumentation and science applications. Volume 2*. Springer reference. Springer, Cham, 2016.

[16] E. Jaeschke, S. Khan, J.R. Schneider, and J.B. Hastings. *Synchrotron Light Sources and Free-Electron Lasers Accelerator Physics, Instrumentation and Science Applications*. Springer International Publishing : Imprint: Springer, Cham, 2020.

[17] D.M. Paganin. *Coherent x-ray optics*. Number 6 in Oxford series on synchrotron radiation. Oxford university press, Oxford, 2013.

[18] H.P. Freund and T.M. Antonsen. *Principles of Free Electron Lasers*. Electrical Engineering. Springer, Cham, Switzerland, third edition edition, 2018.

[19] P. Schmüser, C. Behrens, M. Dohlus, and J. Rossbach. *Free-Electron Lasers in the Ultraviolet and X-Ray Regime: Physical Principles, Experimental Results, Technical Realization*. Number 258 in Springer Tracts in Modern Physics. Springer International Publishing : Imprint: Springer, Cham, 2nd ed. 2014 edition, 2014.

[20] F. Boscherini, C. Meneghini, and S. Mobilio, editors. *Synchrotron Radiation: Basics, Methods and Applications*. Springer Berlin Heidelberg : Imprint: Springer, Berlin, Heidelberg, 1st ed. 2015 edition, 2015.

[21] E. G. Steward. *Fourier optics: an introduction (second edition)*. Dover Publications, Mineola, N.Y, 2004.

[22] K. Khare. *Fourier optics and computational imaging*. Wiley, John Wiley & Sons Ltd, Chichester, West Sussex, 2016.

[23] S. Marchesini, H. He, H.N. Chapman, S.P. Hau-Riege, A. Noy, M.R. Howells, U. Weierstall, and J.C.H. Spence. X-ray image reconstruction from a diffraction pattern alone. *Physical Review B*, 68(14):140101, 2003.

[24] N.-T.D. Loh and V. Elser. Reconstruction algorithm for single-particle diffraction imaging experiments. *Physical Review E*, 80(2):026705, 2009.

[25] K. Ayyer, T.-Y. Lan, V. Elser, and N.D. Loh. *Dragonfly*: an implementation of the expand–maximize–compress algorithm for single-particle imaging. *Journal of Applied Crystallography*, 49(4):1320–1335, 2016.

[26] H. Liu and J.C.H. Spence. Xfel data analysis for structural biology. *Quantitative Biology*, 4(3):159–176, 2016.

[27] Tomas Ekeberg, Dameli Assalauova, Johan Bielecki, Rebecca Boll, Benedikt J. Daurer, Lutz A. Eichacker, Linda E. Franken, Davide E. Galli, Luca Gelisio, Lars Gumprecht, Laura H. Gunn, Janos Hajdu, Robert Hartmann, Dirk Hasse, Alexandr Ignatenko, Jayanath Koliyadu, Olena Kulyk, Ruslan Kurta, Markus Kuster, Wolfgang Lugmayr, Jannik Lübke, Adrian P. Mancuso, Tommaso

Mazza, Carl Nettelblad, Yevheniy Ovcharenko, Daniel E. Rivas, Max Rose, Amit K. Samanta, Philipp Schmidt, Egor Sobolev, Nicusor Timneanu, Sergey Usenko, Daniel Westphal, Tamme Wollweber, Lena Worbs, Paul Lourdu Xavier, Hazem Yousef, Kartik Ayyer, Henry N. Chapman, Jonas A. Sellberg, Carolin Seuring, Ivan A. Vartanyants, Jochen Küpper, Michael Meyer, and Filipe R. N. C. Maia. Observation of a single protein by ultrafast x-ray diffraction. *Light: Science & Applications*, 13(1):15, 2024.

[28] I.K. Robinson, I.A. Vartanyants, G.J. Williams, M.A. Pfeifer, and J.A. Pitney. Reconstruction of the shapes of gold nanocrystals using coherent x-ray diffraction. *Physical Review Letters*, 87:195505, 2001.

[29] G. van der Schot, M. Svenda, F.R.N.C. Maia, M. Hantke, D.P. DePonte, M.M. Seibert, A. Aquila, J. Schulz, R. Kirian, M. Liang, F. Stellato, B. Iwan, J. Andreasson, N. Timneanu, D. Westphal, F.N. Almeida, D. Odic, D. Hasse, G.H. Carlsson, D.S.D. Larsson, A. Barty, A.V. Martin, S. Schorb, C. Bostedt, J.D. Bozek, D. Rolles, A. Rudenko, S. Epp, L. Foucar, B. Rudek, R. Hartmann, N. Kimmel, P. Holl, L. Englert, N.-T.D. Loh, H.N. Chapman, I. Andersson, J. Hajdu, and T. Ekeberg. Imaging single cells in a beam of live cyanobacteria with an x-ray laser. *Nature Communications*, 6(1):5704, 2015.

[30] M.M. Seibert, T. Ekeberg, F.R.N.C. Maia, M. Svenda, J. Andreasson, O. Jönsson, D. Odic, B. Iwan, A. Rocker, D. Westphal, M.F. Hantke, D.P. DePonte, A. Barty, J. Schulz, L. Gumprecht, N. Coppola, A. Aquila, M. Liang, T.A. White, A.V. Martin, C. Caleman, S. Stern, C. Abergel, V. Seltzer, J.-M. Claverie, C. Bostedt, J.D. Bozek, S. Boutet, A. Miahnahri, M. Messerschmidt, J. Krzywinski, G.J. Williams, K.O. Hodgson, M.J. Bogan, C.Y. Hampton, R.G. Sierra, D. Starodub, I. Andersson, S. Bajt, M. Barthelmess, J.C.H. Spence, P. Fromme, U. Weierstall, R.A. Kirian, M.S. Hunter, R.B. Doak, S. Marchesini, S.P. Hau-Riege, M. Frank, R.L. Shoeman, L. Lomb, S.W. Epp, R. Hartmann, D. Rolles, A. Rudenko, C. Schmidt, L. Foucar, N. Kimmel, P. Holl, B. Rudek, B. Erk, A. Hömke, C. Reich, D. Pietschner, G. Weidenspointner, L. Strüder, G. Hauser, H. Gorke, J. Ullrich, I. Schlichting, S. Herrmann, G. Schaller, F. Schopper, H. Soltau, K.U. Kuhnel, R. Andritschke, C.D. Schröter, F. Krasniqi, M. Bott, S. Schorb, D. Rupp, M. Adolph, T. Gorkhover, H. Hirsemann, G. Potdevin, H. Graafsma, B. Nilsson, H.N. Chapman, and J. Hajdu. Single mimivirus particles intercepted and imaged with an x-ray laser. *Nature*, 470(7332):78–81, 2011.

[31] T. Ekeberg, M. Svenda, C. Abergel, F.R.N.C. Maia, V. Seltzer, J.-M. Claverie, M. Hantke, O. Jönsson, C. Nettelblad, G. van der Schot, M. Liang, D.P. DePonte, A. Barty, M.M. Seibert, B. Iwan, I. Andersson, N.D. Loh, A.V. Martin, H. Chapman, C. Bostedt, J.D. Bozek, K.R. Ferguson, J. Krzywinski, S.W.

Epp, D. Rolles, A. Rudenko, R. Hartmann, N. Kimmel, and J. Hajdu. Three-Dimensional Reconstruction of the Giant Mimivirus Particle with an X-Ray Free-Electron Laser. *Physical Review Letters*, 114(9):098102, 2015.

[32] R.P. Kurta, J.J. Donatelli, C.H. Yoon, P. Berntsen, J. Bielecki, B.J. Daurer, H. DeMirci, P. Fromme, M.F. Hantke, F.R.N.C. Maia, A. Munke, C. Nettelblad, K. Pande, H.K.N. Reddy, J.A. Sellberg, R.G. Sierra, M. Svenda, G. van der Schot, I.A. Vartanyants, G.J. Williams, P.L. Xavier, A. Aquila, P.H. Zwart, and A.P. Mancuso. Correlations in scattered x-ray laser pulses reveal nanoscale structural features of viruses. *Physical Review Letters*, 119:158102, 2017.

[33] M. Rose, S. Bobkov, K. Ayyer, R.P. Kurta, D. Dzhigaev, Y.Y. Kim, A.J. Morgan, C.H. Yoon, D. Westphal, J. Bielecki, J.A. Sellberg, G. Williams, F.R.N.C. Maia, O.M. Yefanov, V. Ilyin, A.P. Mancuso, H.N. Chapman, B.G. Hogue, A. Aquila, A. Barty, and I.A. Vartanyants. Single-particle imaging without symmetry constraints at an X-ray free-electron laser. *IUCrJ*, 5(6):727–736, 2018.

[34] A. Munke, J. Andreasson, A. Aquila, S. Awel, K. Ayyer, A. Barty, R.J. Bean, P. Berntsen, J. Bielecki, S. Boutet, et al. Coherent diffraction of single rice dwarf virus particles using hard x-rays at the linac coherent light source. *Scientific data*, 3(1):1–12, 2016.

[35] H.K.N. Reddy, C.H. Yoon, A. Aquila, S. Awel, K. Ayyer, A. Barty, P. Berntsen, J. Bielecki, S. Bobkov, M. Bucher, G.A. Carini, S. Carron, H. Chapman, B. Daurer, H. DeMirci, T. Ekeberg, P. Fromme, J. Hajdu, M.F. Hanke, P. Hart, B.G. Hogue, A. Hosseinizadeh, Y. Kim, R.A. Kirian, R.P. Kurta, D.S.D. Larsson, N.D. Loh, F.R.N.C. Maia, A.P. Mancuso, K. Mühlig, A. Munke, D. Nam, C. Nettelblad, A. Ourmazd, M. Rose, P. Schwander, M. Seibert, J.A. Sellberg, C. Song, J.C.H. Spence, M. Svenda, G. Van der Schot, I.A. Vartanyants, G.J. Williams, and P.L. Xavier. Coherent soft x-ray diffraction imaging of coliphage pr772 at the linac coherent light source. *Scientific Data*, 4(1):170079, 2017.

[36] B.J. Daurer, K. Okamoto, J. Bielecki, F.R.N.C. Maia, K. Mühlig, M.M. Seibert, M.F. Hantke, C. Nettelblad, W.H. Benner, M. Svenda, N. Tîmneanu, T. Ekeberg, N.D. Loh, A. Pietrini, A. Zani, A.D. Rath, D. Westphal, R.A. Kirian, S. Awel, M.O. Wiedorn, G. van der Schot, G.H. Carlsson, D. Hasse, J.A. Sellberg, A. Barty, J. Andreasson, S. Boutet, G. Williams, J. Koglin, I. Andersson, J. Hajdu, and D.S.D. Larsson. Experimental strategies for imaging bioparticles with femtosecond hard X-ray pulses. *IUCrJ*, 4(3):251–262, 2017.

[37] E.V. Sobolev, S. Zolotarev, K. Giewekemeyer, J. Bielecki, K. Okamoto, H.K.N. Reddy, J. Andreasson, K. Ayyer, I. Barák, S. Bari, A. Barty, R. Bean, S. Bobkov,

H.N. Chapman, G. Chojnowski, B.J. Daurer, K. Dörner, T. Ekeberg, L. Flückiger, O.V. Galzitskaya, L. Gelisio, S. Hauf, B.G. Hogue, D.A. Horke, A. Hosseinizadeh, V.A. Ilyin, C. Jung, C. Kim, Y. Kim, R.A. Kirian, H. Kirkwood, O. Kulyk, J. Küpper, R. Letrun, N.D. Loh, K. Lorenzen, M. Messerschmidt, K. Mühlig, A. Ourmazd, N. Raab, A. Rode, M. Rose, A. Round, T. Sato, R. Schubert, P. Schwander, J.A. Sellberg, M. Sikorski, A. Silenzi, C. Song, J.C.H. Spence, S. Stern, J. Sztuk-Dambietz, A. Teslyuk, N. Timneanu, M. Trebbin, C. Uetrecht, B. Weinhausen, G.J. Williams, P.L. Xavier, C. Xu, I.A. Vartanyants, V.S. Lamzin, A.P. Mancuso, and F.R.N.C. Maia. Megahertz single-particle imaging at the european xfel. *Communications in Physics*, 3(1): 97, 2020.

[38] T. Gorkhover, A. Ulmer, K. Ferguson, M. Bucher, F.R.N.C. Maia, J. Bielecki, T. Ekeberg, M.F. Hantke, B.J. Daurer, C. Nettelblad, et al. Femtosecond x-ray fourier holography imaging of free-flying nanoparticles. *Nature Photonics*, 12 (3):150–153, 2018.

[39] I.V. Lundholm, J.A. Sellberg, T. Ekeberg, M.F. Hantke, K. Okamoto, G. van der Schot, J. Andreasson, A. Barty, J. Bielecki, P. Bruza, M. Bucher, S. Carron, B.J. Daurer, K. Ferguson, D. Hasse, J. Krzywinski, D.S.D. Larsson, A. Morgan, K. Mühlig, M. Müller, C. Nettelblad, A. Pietrini, H.K.N. Reddy, D. Rupp, M. Sauppe, M. Seibert, M. Svenda, M. Swiggers, N. Timneanu, A. Ulmer, D. Westphal, G. Williams, A. Zani, G. Faigel, H.N. Chapman, T. Möller, C. Bostedt, J. Hajdu, T. Gorkhover, and F.R.N.C. Maia. Considerations for three-dimensional image reconstruction from experimental data in coherent diffractive imaging. *IUCrJ*, 5(5):531–541, 2018.

[40] M.F. Hantke, D. Hasse, F.R.N.C. Maia, T. Ekeberg, K. John, M. Svenda, N.D. Loh, A.V. Martin, N. Timneanu, D.S.D. Larsson, G. van der Schot, G.H. Carlsson, M. Ingelman, J. Andreasson, D. Westphal, M. Liang, F. Stellato, D.P. DePonte, R. Hartmann, N. Kimmel, R.A. Kirian, M.M. Seibert, K. Mühlig, S. Schorb, K. Ferguson, C. Bostedt, S. Carron, J.D. Bozek, D. Rolles, A. Rudenko, S. Epp, H.N. Chapman, A. Barty, J. Hajdu, and I. Andersson. High-throughput imaging of heterogeneous cell organelles with an X-ray laser. *Nature photonics*, 8(12):943–949, 2014.

[41] C. Neuhaus, J. Alfken, K. Komorowski, M.L. Stammer, R. Bean, J. Bielecki, R. de Wijn, R. Letrun, S. Rafie-Zinedine, E. Juncheng, A. Mancuso, R. Jahn, and T. Salditt. Coherent diffractive imaging of lipid vesicles and synaptic vesicles by femtosecond x-ray fel pulses. *Biophysical Journal*, 122(3, Supplement 1): 322a, 2023.

[42] P.J. Ho, B.J. Daurer, M.F. Hantke, J. Bielecki, A. Al Haddad, M. Bucher, G. Doumy, K.R. Ferguson, L. Flückiger, T. Gorkhover, et al. The role of transient resonances for ultra-fast imaging of single sucrose nanoclusters. *Nature communications*, 11(1):167, 2020.

[43] K. Ayyer, P.L. Xavier, J. Bielecki, Z. Shen, B.J. Daurer, A.K. Samanta, S. Awel, R. Bean, A. Barty, M. Bergemann, et al. 3d diffractive imaging of nanoparticle ensembles using an x-ray laser. *Optica*, 8(1):15–23, 2021.

[44] J. Bielecki, M.F. Hantke, B.J. Daurer, H.K.N. Reddy, D. Hasse, D.S.D. Larsson, L.H. Gunn, M. Svenda, A. Munke, J.A. Sellberg, et al. Electrospray sample injection for single-particle imaging with x-ray lasers. *Science advances*, 5(5): eaav8801, 2019.

[45] D.P. DePonte, U. Weierstall, K. Schmidt, J. Warner, D. Starodub, J.C.H. Spence, and R.B. Doak. Gas dynamic virtual nozzle for generation of microscopic droplet streams. *Journal of Physics D: Applied Physics*, 41(19):195505, 2008.

[46] J. Knoska, L. Adriano, S. Awel, K.R. Beyerlein, O. Yefanov, D. Oberthuer, G.E. Peña Murillo, N. Roth, I. Sarrou, P. Villanueva-Perez, M.O. Wiedorn, F. Wilde, S. Bajt, H.N. Chapman, and M. Heymann. Ultracompact 3d microfluidics for time-resolved structural biology. *Nature Communications*, 11(1):657, 2020.

[47] A. Echelmeier, M. Sonker, and A. Ros. Microfluidic sample delivery for serial crystallography using xfels. *Analytical and Bioanalytical Chemistry*, 411(25):6535–6547, 2019.

[48] B. Marmiroli, G. Grenci, F. Cacho-Nerin, B. Sartori, E. Ferrari, P. Laggner, L. Businaro, and H. Amenitsch. Free jet micromixer to study fast chemical reactions by small angle x-ray scattering. *Lab on a Chip*, 9(14):2063–2069, 2009.

[49] O. Saldanha, R. Graceffa, C.Y.J. Hémonnot, C. Ranke, G. Brehm, M. Liebi, B. Marmiroli, B. Weinhausen, M. Burghammer, and S. Köster. Rapid acquisition of x-ray scattering data from droplet-encapsulated protein systems. *ChemPhysChem*, 18(10):1220–1223, 2017.

[50] I. Steinke, M. Walther, F. Lehmkühler, P. Wochner, J. Valerio, R. Mager, M.A. Schroer, S. Lee, W. Roseker, A. Jain, M. Sikorski, S. Song, R. Hartmann, M. Huth, L. Strüder, M. Sprung, A. Robert, P.H. Fuoss, G.B. Stephenson, and G. Grübel. A liquid jet setup for x-ray scattering experiments on complex liquids at free-electron laser sources. *Review of Scientific Instruments*, 87(6): 063905, 2016.

[51] F. Stellato, D. Oberthür, M. Liang, R. Bean, C. Gati, O. Yefanov, A. Barty, A. Burkhardt, P. Fischer, L. Galli, R.A. Kirian, J. Meyer, S. Panneerselvam, C.H. Yoon, F. Chervinskii, E. Speller, T.A. White, C. Betzel, A. Meents, and H.N. Chapman. Room-temperature macromolecular serial crystallography using synchrotron radiation. *IUCrJ*, 1(4):204–212, 2014.

[52] A.R. Pearson and P. Mehrabi. Serial synchrotron crystallography for time-resolved structural biology. *Current Opinion in Structural Biology*, 65:168–174, 2020.

[53] M. Vakili, J. Bielecki, J. Knoška, F. Otte, H. Han, M. Kloos, R. Schubert, E. Delmas, G. Mills, R. de Wijn, et al. 3d printed devices and infrastructure for liquid sample delivery at the european xfel. *Journal of Synchrotron Radiation*, 29 (2):331–346, 2022.

[54] M.O. Wiedorn, D. Oberthür, R. Bean, R. Schubert, N. Werner, B. Abbey, M. Aepfelbacher, L. Adriano, A. Allahgholi, N. Al-Qudami, J. Andreasson, S. Aplin, S. Awel, K. Ayyer, S. Bajt, I. Barák, S. Bari, J. Bielecki, S. Botha, D. Boukhelef, W. Brehm, S. Brockhauser, I. Cheviakov, M.A. Coleman, F. Cruz-Mazo, C. Danilevski, C. Darmanin, R.B. Doak, M. Domaracky, K. Dörner, Y. Du, H. Fangohr, H. Fleckenstein, M. Frank, P. Fromme, A.M. Gañán-Calvo, Y. Gevorkov, K. Giewekemeyer, H.M. Ginn, H. Graafsma, R. Graceffa, D. Greiffenberg, L. Gumprecht, P. Göttlicher, J. Hajdu, S. Hauf, M. Heymann, S. Holmes, D.A. Horke, M.S. Hunter, S. Imlau, A. Kaukher, Y. Kim, A. Klyuev, J. Knoška, B. Kobe, M. Kuhn, C. Kupitz, J. Küpper, J.M. Lahey-Rudolph, T. Laurus, K. Le Cong, R. Letrun, P.L. Xavier, L. Maia, F.R.N.C. Maia, V. Mariani, M. Messerschmidt, M. Metz, D. Mezza, T. Michelat, G. Mills, D.C.F. Monteiro, A. Morgan, K. Mühlig, A. Munke, A. Münnich, J. Nette, K.A. Nugent, T. Nuguid, A.M. Orville, S. Pandey, G. Pena, P. Villanueva-Perez, J. Poehlsen, G. Previtali, L. Redecke, W.M. Riekehr, H. Rohde, A. Round, T. Safenreiter, I. Sarrou, T. Sato, M. Schmidt, B. Schmitt, R. Schönherr, J. Schulz, J.A. Sellberg, M.M. Seibert, C. Seuring, M.L. Shelby, R.L. Shoeman, M. Sikorski, A. Silenzi, C.A. Stan, X. Shi, S. Stern, J. Sztuk-Dambietz, J. Szuba, A. Tolstikova, M. Trebbin, U. Trunk, P. Vagovic, T. Ve, B. Weinhausen, T.A. White, K. Wrona, C. Xu, O. Yefanov, N. Zatsepin, J. Zhang, M. Perbandt, A.P. Mancuso, C. Betzel, H. Chapman, and A. Barty. Megahertz serial crystallography. *Nature Communications*, 9(1):4025, 2018.

[55] P.E. Konold, T. You, J. Bielecki, J. Valerio, M. Kloos, D. Westphal, A. Bellisario, T. Varma Yenupuri, A. Wollter, J.C.P. Koliyadu, F.H.M. Koua, R. Letrun, A. Round, T. Sato, P. Mészáros, L. Monrroy, J. Mutisya, S. Bódizs, T. Larkiala, A. Nimmrich, R. Alvarez, P. Adams, R. Bean, T. Ekeberg, R.A. Kirian, A.V.

Martin, S. Westenhoff, and F.R.N.C. Maia. 3D-printed sheet jet for stable megahertz liquid sample delivery at X-ray free-electron lasers. *IUCrJ*, 10(6): 662–670, 2023.

[56] D. Oberthuer, J. Knoška, M.O. Wiedorn, K.R. Beyerlein, D.A. Bushnell, E.G. Kovaleva, M. Heymann, L. Gumprecht, R.A. Kirian, A. Barty, V. Mariani, A. Tolstikova, L. Adriano, S. Awel, M. Barthelmess, K. Dörner, P.L. Xavier, O. Yefanov, D.R. James, G. Nelson, D. Wang, G. Calvey, Y. Chen, A. Schmidt, M. Szczepek, S. Frielingsdorf, O. Lenz, E. Snell, P.J. Robinson, B. Šarler, G. Belšak, M. Maček, F. Wilde, A. Aquila, S. Boutet, M. Liang, M.S. Hunter, P. Scheerer, J.D. Lipscomb, U. Weierstall, R.D. Kornberg, J.C.H. Spence, L. Pollack, H.N. Chapman, and S. Bajt. Double-flow focused liquid injector for efficient serial femtosecond crystallography. *Scientific Reports*, 7(1):44628, 2017.

[57] A. Echelmeier, J. Cruz Villarreal, M. Messerschmidt, D. Kim, J.D. Coe, D. Thifault, S. Botha, A. Egatz-Gomez, S. Gandhi, G. Brehm, C.E. Conrad, D.T. Hansen, C. Madsen, S. Bajt, J.D. Meza-Aguilar, D. Oberthür, M.O. Wiedorn, H. Fleckenstein, D. Mendez, J. Knoška, J.M. Martin-Garcia, H. Hu, S. Lisova, A. Allahgholi, Y. Gevorkov, K. Ayyer, S. Aplin, H.M. Ginn, H. Graafsma, A.J. Morgan, D. Greiffenberg, A. Klujev, T. Laurus, J. Poehlsen, U. Trunk, D. Mezza, B. Schmidt, M. Kuhn, R. Fromme, J. Sztuk-Dambietz, N. Raab, S. Hauf, A. Silenzi, T. Michelat, C. Xu, C. Danilevski, A. Parenti, L. Mekinda, B. Weinhausen, G. Mills, P. Vagovic, Y. Kim, H. Kirkwood, R. Bean, J. Bielecki, S. Stern, K. Giewekemeyer, A.R. Round, J. Schulz, K. Dörner, T.D. Grant, V. Mariani, A. Barty, A.P. Mancuso, U. Weierstall, J.C.H. Spence, H.N. Chapman, N. Zatsepin, P. Fromme, R.A. Kirian, and A. Ros. Segmented flow generator for serial crystallography at the european x-ray free electron laser. *Nature Communications*, 11(1):4511, 2020.

[58] U. Weierstall, D. James, C. Wang, T.A. White, D. Wang, W. Liu, J.C.H. Spence, R.B. Doak, G. Nelson, P. Fromme, R. Fromme, I. Grotjohann, C. Kupitz, N.A. Zatsepin, H. Liu, S. Basu, D. Wacker, G.W. Han, V. Katritch, S. Boutet, M. Messerschmidt, G.J. Williams, J.E. Koglin, M.M. Seibert, M. Klinker, C. Gati, R.L. Shoeman, A. Barty, H.N. Chapman, R.A. Kirian, K.R. Beyerlein, R.C. Stevens, D. Li, S.T.A. Shah, N. Howe, M. Caffrey, and V. Cherezov. Lipidic cubic phase injector facilitates membrane protein serial femtosecond crystallography. *Nature Communications*, 5(1):3309, 2014.

[59] K. Giewekemeyer, A. Aquila, N.-T.D. Loh, Y. Chushkin, K.S. Shanks, J.T. Weiss, M.W. Tate, H.T. Philipp, S. Stern, P. Vagovic, M. Mehrjoo, C. Teo, M. Barthelmess, F. Zontone, C. Chang, R.C. Tiberio, A. Sakdinawat, G.J.

Williams, S.M. Gruner, and A.P. Mancuso. Experimental 3D coherent diffractive imaging from photon-sparse random projections. *IUCrJ*, 6(3):357–365, 2019.

[60] M.S. Hunter, B. Segelke, M. Messerschmidt, G.J. Williams, N.A. Zatsepin, A. Barty, W.H. Benner, D.B. Carlson, M. Coleman, A. Graf, S.P. Hau-Riege, T. Pardini, M.M. Seibert, J. Evans, S. Boutet, and M. Frank. Fixed-target protein serial microcrystallography with an x-ray free electron laser. *Scientific Reports*, 4(1):6026, 2014.

[61] S. Rafie-Zinedine, T. Varma Yenupuri, L. Worbs, F.R.N.C. Maia, M. Heymann, J. Schulz, and J. Bielecki. Enhancing electrospray ionization efficiency for particle transmission through an aerodynamic lens stack. *J. Synchrotron Rad*, 31(2):222–232, 2024.

[62] M. et al. Bogan. Single particle diffraction at flash. In *Particle Accelerator Conference (PAC 09)*, page FR3RBI01, 2010.

[63] M.F. Hantke, J. Bielecki, O. Kulyk, D. Westphal, D.S.D. Larsson, M. Svenda, H.K.N. Reddy, R.A. Kirian, J. Andreasson, J. Hajdu, et al. Rayleigh-scattering microscopy for tracking and sizing nanoparticles in focused aerosol beams. *IUCrJ*, 5(6):673–680, 2018.

[64] W.C. Hinds and Y. Zhu. *Aerosol technology: properties, behavior, and measurement of airborne particles*. Wiley, Hoboken, NJ, third edition edition, 2022.

[65] I. Colbeck and M. Lazaridis, editors. *Aerosol science: technology and applications*. Wiley, Chichester, 1. publ edition, 2014.

[66] D.-R. Chen, D.Y.H. Pui, and S.L. Kaufman. Electrospraying of conducting liquids for monodisperse aerosol generation in the 4 nm to 1.8 µm diameter range. *Journal of Aerosol Science*, 26(6):963–977, 1995.

[67] M. Enayati, Z. Ahmad, E. Stride, and M. Edirisinghe. One-step electrohydrodynamic production of drug-loaded micro- and nanoparticles. *Journal of the Royal Society Interface*, 7(45):667–675, 2010.

[68] N. Bock, T. Dargaville, and M. Woodruff. Electrospraying of polymers with therapeutic molecules: State of the art. *Progress in Polymer Science*, 37(11):1510–1551, 2012.

[69] A. Jaworek. Electrospray droplet sources for thin film deposition. *Journal of Materials Science*, 42(1):266–297, 2007.

[70] A. Jaworek and A.T. Sobczyk. Electrospraying route to nanotechnology: An overview. *Journal of Electrostatics*, 66(3):197–219, 2008.

[71] J. Zeleny. The electrical discharge from liquid points, and a hydrostatic method of measuring the electric intensity at their surfaces. *Phys. Rev.*, 3:69–91, 1914.

[72] J. Fernandez de la Mora. The fluid dynamics of taylor cones. *Annual Review of Fluid Mechanics*, 39:217–243, 2007.

[73] J. Zeleny. On the condition of instability of electrified drops. *Proc. Camb. Phil. Soc.*, 18:71–83, 1915.

[74] J. Zeleny. Instability of electrified liquid surfaces. *Phys. Rev.*, 10:1–6, 1917.

[75] B. Vonnegut and R.L. Neubauer. Production of monodisperse liquid particles by electrical atomization. *J. Colloid Sci.*, 7(6):616–622, 1952.

[76] M. Wilm and M. Mann. Electrospray and taylor-cone theory, dole's beam of macromolecules at last? *International Journal of Mass Spectrometry and Ion Processes*, 136(2):167–180, 1994.

[77] G.I.S. Taylor. Disintegration of water drops in an electric field. *Proceedings of the Royal Society of London. Series A. Mathematical and Physical Sciences*, 280 (1382):383 – 397, 1964.

[78] A.M. Gañán-Calvo and J.M. Montanero. Revision of capillary cone-jet physics: Electrospray and flow focusing. *Phys. Rev. E*, 79:066305, 2009.

[79] A. Maïßer, M.B. Attoui, A.M. Gañán-Calvo, and W.W. Szymanski. Electrohydrodynamic generation of monodisperse nanoparticles in the sub-10 nm size range from strongly electrolytic salt solutions: governing parameters of scaling laws. *Journal of Nanoparticle Research*, 15(1):1318, 2013.

[80] D.-R. Chen and D.Y.H. Pui. Experimental investigation of scaling laws for electrospraying: Dielectric constant effect. *Aerosol Science and Technology*, 27 (3):367–380, 1997.

[81] M. Cloupeau and B. Prunet-Foch. Electrohydrodynamic spraying functioning modes: a critical review. *Journal of Aerosol Science*, 25(6):1021–1036, 1994.

[82] M. Cloupeau and B. Prunet-Foch. Electrostatic spraying of liquids: Main functioning modes. *Journal of Electrostatics*, 25(2):165–184, 1990.

[83] Q. Liu and D.-R. Chen. An electrospray aerosol generator with x-ray photoionizer for particle charge reduction. *Journal of Aerosol Science*, 76:148–162, 2014.

[84] H.C.W. Beijerinck, R.J.F. Van Gerwen, E.R.T. Kerstel, J.F.M. Martens, E.J.W. Van Vliembergen, M.R.Th. Smits, and G.H. Kaashoek. Campargue-type supersonic beam sources: absolute intensities, skimmer transmission and scaling laws for mono-atomic gases he, ne and ar. *Chemical physics*, 96(1):153–173, 1985.

[85] R. Campargue. Progress in overexpanded supersonic jets and skimmed molecular beams in free-jet zones of silence. *The Journal of Physical Chemistry*, 88(20): 4466–4474, 1984.

[86] L. Worbs, N. Roth, J. Lübke, A.D. Estillore, P.L. Xavier, A.K. Samanta, and J. Küpper. Optimizing the geometry of aerodynamic lens injectors for single-particle coherent diffractive imaging of gold nanoparticles. *Journal of applied crystallography*, 54(6):1730–1737, 2021.

[87] M.J. Bogan, W.H. Benner, S. Boutet, U. Rohner, M. Frank, A. Barty, M.M. Seibert, F.R.N.C. Maia, S. Marchesini, S. Bajt, B.W. Woods, V.J. Riot, S.P. Hau-Riege, M. Svenda, E.G. Marklund, E. Spiller, J. Hajdu, H.N. Chapman, et al. Single particle x-ray diffractive imaging. *Nano Letters*, 8(1):310–316, 2008.

[88] P. Liu, P.J. Ziemann, D.B. Kittelson, and P.H. McMurry. Generating particle beams of controlled dimensions and divergence: I. theory of particle motion in aerodynamic lenses and nozzle expansions. *Aerosol Science and Technology*, 22 (3):293–313, 1995.

[89] P. Liu, P.J. Ziemann, D.B. Kittelson, and P.H. McMurry. Generating particle beams of controlled dimensions and divergence: Ii. experimental evaluation of particle motion in aerodynamic lenses and nozzle expansions. *Aerosol Science and Technology*, 22(3):314–324, 1995.

[90] W.K. Murphy and G.W. Sears. Production of particulate beams. *Journal of Applied Physics*, 35(6):1986–1987, 1964.

[91] M.M. Seibert, T. Ekeberg, F.R.N.C. Maia, M. Svenda, J. Andreasson, O. Jönsson, D. Odić, B. Iwan, A. Rocker, D. Westphal, M. Hantke, D.P. DePonte, A. Barty, J. Schulz, L. Gumprecht, N. Coppola, A. Aquila, M. Liang, T.A. White, A. Martin, C. Caleman, S. Stern, C. Abergel, V. Seltzer, J.-M. Claverie, C. Bostedt, J.D. Bozek, S. Boutet, A.A. Miahnahri, M. Messerschmidt, J. Krzywinski, G. Williams, K.O. Hodgson, M.J. Bogan, C.Y. Hampton, R.G. Sierra, D. Starodub, I. Andersson, S. Bajt, M. Barthelmess, J.C.H. Spence, P. Fromme, U. Weierstall, R. Kirian, M. Hunter, R.B. Doak, S. Marchesini, S.P. Hau-Riege, M. Frank, R.L. Shoeman, L. Lomb, S.W. Epp, R. Hartmann, D. Rolles, A. Rudenko, C. Schmidt, L. Foucar, N. Kimmel, P. Holl, B. Rudek, B. Erk, A. Hömke, C. Reich, D. Pietschner, G. Weidenspointner, L. Strüder,

G. Hauser, H. Gorke, J. Ullrich, I. Schlichting, S. Herrmann, G. Schaller, F. Schopper, H. Soltau, K.-U. Kühnel, R. Andritschke, C.-D. Schröter, F. Krasniqi, M. Bott, S. Schorb, D. Rupp, M. Adolph, T. Gorkhover, H. Hirsemann, G. Potdevin, H. Graafsma, B. Nilsson, H.N. Chapman, and J. Hajdu. Single mimivirus particles intercepted and imaged with an x-ray laser. *Nature*, 470 (7332):78–81, 2011.

[92] M. Göppert-Mayer. Elementary processes with two quantum transitions. *Annalen der Physik*, 18(7-8):466–479, 2009.

[93] Q. Hu. Multiphoton lithograpy based 3d micro/nano printing. *EPSRC Centre for Innovative Manufacturing in Additive Manufacturing*, pages 1–30.

[94] V. Harinarayana and Y.C. Shin. Two-photon lithography for three-dimensional fabrication in micro/nanoscale regime: A comprehensive review. *Optics & Laser Technology*, 142:107180, 2021.

[95] W.G.C.G.B. Kaiser and C.G.B. Garrett. Two-photon excitation in ca f 2: Eu 2+. *Physical review letters*, 7(6):229, 1961.

[96] S. Maruo, O. Nakamura, and S. Kawata. Three-dimensional microfabrication with two-photon-absorbed photopolymerization. *Optics letters*, 22(2):132–134, 1997.

[97] Z. Faraji Rad, P.D. Prewett, and G.J. Davies. High-resolution two-photon polymerization: the most versatile technique for the fabrication of microneedle arrays. *Microsystems & Nanoengineering*, 7(1):71, 2021.

[98] A.-I. Bunea, N. del Castillo Iniesta, A. Droumpali, A.E. Wetzel, E. Engay, and R. Taboryski. Micro 3d printing by two-photon polymerization: Configurations and parameters for the nanoscribe system. *Micro*, 1(2):164–180, 2021.

[99] Richard B. Cole, editor. *Electrospray and MALDI mass spectrometry: fundamentals, instrumentation, practicalities, and biological applications*. Wiley, Hoboken, N.J, 2nd ed edition, 2010.

[100] Richard B. Cole, editor. *Electrospray ionization mass spectrometry: fundamentals, instrumentation, and applications*. Wiley, New York, 1997.

[101] D.L. Nelson, M.M. Cox, and A.L. Lehninger. *Lehninger principles of biochemistry*. W.H. Freeman and Company ; Macmillan Higher Education, New York, NY : Houndmills, Basingstoke, seventh edition edition, 2017.

[102] J.M. Berg, J.L. Tymoczko, G.J. Gatto, and L. Stryer. *Biochemistry*. Macmillan International, Higher Education, New York, ninth edition edition, 2019.

[103] P.W. Atkins and J. De Paula. *Physical chemistry for the life sciences*. W.H. Freeman and Co. ; Oxford University Press, New York : Oxford, 2nd ed edition, 2011.

[104] E. de Hoffmann and V. Stroobant. *Mass spectrometry: principles and applications*. J. Wiley, Chichester, West Sussex, England ; Hoboken, NJ, 3rd ed edition, 2007.

[105] S.K. Kulkarni. *Nanotechnology: Principles and Practices*. Springer International Publishing Springer e-books Imprint: Springer, Cham, 3rd ed. 2015 edition, 2015.

[106] C. N. R. Rao, A. Müller, and A. K. Cheetham, editors. *The chemistry of nanomaterials: synthesis, properties and applications in 2 volumes*. Wiley-VCH, Weinheim, 2004.

[107] C. Binns. *Introduction to nanoscience and nanotechnology*. John Wiley & Sons, Inc, Hoboken, NJ, USA, second edition edition, 2022.

[108] M.F. Hantke, J. Bielecki, O. Kulyk, D. Westphal, D.S.D. Larsson, M. Svenda, H.K.N. Reddy, R.A. Kirian, J. Andreasson, J. Hajdu, and F.R.N.C. Maia. Rayleigh-scattering microscopy for tracking and sizing nanoparticles in focused aerosol beams. *IUCrJ*, 5(6):673–680, 2018.

[109] A. Jaworek and A. Krupa. Classification of the modes of ehd spraying. *Journal of Aerosol Science*, 30(7):873–893, 1999.

[110] J.F. De La Mora and P. Riesco-Chueca. Aerodynamic focusing of particles in a carrier gas. *Journal of Fluid Mechanics*, 195:1–21, 1988.

[111] P. Liu, P.J. Ziemann, D.B. Kittelson, and P.H. McMurry. Generating particle beams of controlled dimensions and divergence: I. Theory of particle motion in aerodynamic lenses and nozzle expansions. *Aerosol Science and Technology*, 22 (3):293–313, 1995.

[112] A.M. Gañán-Calvo. Cone-jet analytical extension of taylor's electrostatic solution and the asymptotic universal scaling laws in electrospraying. *Physical Review Letters*, 79:217–220, 1997.

[113] D.D. Ebeling, M.S. Westphall, M. Scalf, and L.M. Smith. Corona discharge in charge reduction electrospray mass spectrometry. *Analytical Chemistry*, 72(21): 5158–5161, 2000.

[114] H. Fu, A.C. Patel, M.J. Holtzman, and D.-R. Chen. A new electrospray aerosol generator with high particle transmission efficiency. *Aerosol Science and Technology*, 45(10):1176–1183, 2011.

[115] S. Seltzer. Tables of x-ray mass attenuation coefficients and mass energy-absorption coefficients, nist standard reference database 126, 1995.

[116] T.V. Yenupuri, S. Rafie-Zinedine, L. Worbs, M. Heymann, J. Schulz, J. Bielecki, and F.R.N.C. Maia. Helium-electrospray improves sample delivery in x-ray single-particle imaging experiments. *Scientific Reports*, 14(1):4401, 2024.

[117] J. Miao, T. Ishikawa, I.K. Robinson, and M.M. Murnane. Beyond crystallography: Diffractive imaging using coherent x-ray light sources. *Science*, 348(6234): 530–535, 2015.

[118] A. Aquila, A. Barty, C. Bostedt, S. Boutet, G. Carini, D. DePonte, P. Drell, S. Doniach, K.H. Downing, T. Earnest, et al. The linac coherent light source single particle imaging road map. *Structural Dynamics*, 2(4):041701, 2015.

[119] M.M. Seibert, T. Ekeberg, F.R.N.C. Maia, M. Svenda, J. Andreasson, O. Jönsson, D. Odić, B. Iwan, A. Rocker, D. Westphal, et al. Single mimivirus particles intercepted and imaged with an x-ray laser. *Nature*, 470(7332):78–81, 2011.

[120] A. Munke, J. Andreasson, A. Aquila, S. Awel, K. Ayyer, A. Barty, R.J. Bean, P. Berntsen, J. Bielecki, S. Boutet, et al. Coherent diffraction of single rice dwarf virus particles using hard x-rays at the linac coherent light source. *Scientific data*, 3(1):1–12, 2016.

[121] H.K.N. Reddy, C.H. Yoon, A. Aquila, S. Awel, K. Ayyer, A. Barty, P. Berntsen, J. Bielecki, S. Bobkov, M. Bucher, et al. Coherent soft x-ray diffraction imaging of coliphage pr772 at the linac coherent light source. *Scientific data*, 4(1):1–9, 2017.

[122] I.V. Lundholm, J.A. Sellberg, T. Ekeberg, M.F. Hantke, K. Okamoto, G. van der Schot, J. Andreasson, A. Barty, J. Bielecki, P. Bruza, M. Bucher, S. Carron, B.J. Daurer, K. Ferguson, D. Hasse, J. Krzywinski, D.S.D. Larsson, A. Morgan, K. Mühlig, M. Müller, C. Nettelblad, A. Pietrini, H.K.N. Reddy, D. Rupp, M. Sauppe, M. Seibert, M. Svenda, M. Swiggers, N. Timneanu, A. Ulmer, D. Westphal, G. Williams, A. Zani, G. Faigel, H.N. Chapman, T. Möller, C. Bostedt, J. Hajdu, T. Gorkhover, F.R.N.C. Maia, et al. Considerations for three-dimensional image reconstruction from experimental data in coherent diffractive imaging. *IUCrJ*, 5(Pt 5):531–541, 2018.

[123] M. Rose, S. Bobkov, K. Ayyer, R.P. Kurta, D. Dzhigaev, Y.Y. Kim, A.J. Morgan, C.H. Yoon, D. Westphal, J. Bielecki, J.A. Sellberg, G. Williams, F.R.N.C. Maia, O.M. Yefanov, V. Ilyin, A.P. Mancuso, H.N. Chapman, B.G. Hogue, A. Aquila, A. Barty, and I.A. Vartanyants. Single-particle imaging without

symmetry constraints at an x-ray free-electron laser. *IUCrJ*, 5(Pt 6):727–736, 2018.

[124] G. Van Der Schot, M. Svenda, F.R.N.C. Maia, M. Hantke, D.P. DePonte, M.M. Seibert, A. Aquila, J. Schulz, R. Kirian, M. Liang, et al. Imaging single cells in a beam of live cyanobacteria with an x-ray laser. *Nature communications*, 6(1):5704, 2015.

[125] K. Ayyer, P.L. Xavier, J. Bielecki, Z. Shen, B.J. Daurer, A.K. Samanta, S. Awel, R. Bean, A. Barty, M. Bergemann, T. Ekeberg, A.D. Estillore, H. Fangohr, K. Giewekemeyer, M.S. Hunter, M. Karnevskiy, R.A. Kirian, H. Kirkwood, Y. Kim, J. Koliyadu, H. Lange, R. Letrun, J. Lübke, T. Michelat, A.J. Morgan, N. Roth, T. Sato, M. Sikorski, F. Schulz, J.C.H. Spence, P. Vagovic, T. Wollweber, L. Worbs, O. Yefanov, Y. Zhuang, F.R.N.C. Maia, D.A. Horke, J. Küpper, N.D. Loh, A.P. Mancuso, H.N. Chapman, et al. 3d diffractive imaging of nanoparticle ensembles using an x-ray laser. *Optica*, 8(1):15–23, 2021.

[126] M.J. Bogan, W.H. Benner, S. Boutet, U. Rohner, M. Frank, A. Barty, M.M. Seibert, F. Maia, S. Marchesini, S. Bajt, et al. Single particle x-ray diffractive imaging. *Nano letters*, 8(1):310–316, 2008.

[127] A. Bellisario, F.R.N.C. Maia, and T. Ekeberg. Noise reduction and mask removal neural network for x-ray single-particle imaging. *Journal of applied crystallography*, 55(1):122–132, 2022.

[128] S. Pandey, R. Bean, T. Sato, I. Poudyal, J. Bielecki, J. Cruz Villarreal, O. Yefanov, V. Mariani, T.A. White, C. Kupitz, et al. Time-resolved serial femtosecond crystallography at the european xfel. *Nature methods*, 17(1):73–78, 2020.

[129] I. Poudyal, M. Schmidt, and P. Schwander. Single-particle imaging by x-ray free-electron lasers—How many snapshots are needed? *Structural Dynamics*, 7 (2):024102, 2020.

[130] T.V. Yenupuri, L. Worbs, T. You, and F.R.N.C. Maia. Optical detection and sizing of single sub-20 nm bioparticles in a focused aerosol particle beam. Manuscript in progress, 2023.

[131] COMSOL. Comsol multiphysics®, 2022.

[132] I.G. Loscertales, A. Barrero, I. Guerrero, R. Cortijo, M. Marquez, and A.M. Gañán-Calvo. Micro/nano encapsulation via electrified coaxial liquid jets. *Science*, 295(5560):1695–1698, 2002.

[133] Adrian P. Mancuso, Andrew Aquila, Lewis Batchelor, Richard J. Bean, Johan Bielecki, Gannon Borchers, Katerina Doerner, Klaus Giewekemeyer, Rita Graceffa, Oliver D. Kelsey, Yoonhee Kim, Henry J. Kirkwood, Alexis Legrand, Romain Letrun, Bradley Manning, Luis Lopez Morillo, Marc Messerschmidt, Grant Mills, Steffen Raabe, Nadja Reimers, Adam Round, Tokushi Sato, Joachim Schulz, Cedric Signe Takem, Marcin Sikorski, Stephan Stern, Prasad Thute, Patrik Vagovič, Britta Weinhausen, and Thomas Tschentscher. The Single Particles, Clusters and Biomolecules and Serial Femtosecond Crystallography instrument of the European XFEL: initial installation. *Journal of Synchrotron Radiation*, 26(3):660–676, 2019.

[134] F. Paschen. Ueber die zum funkenübergang in luft, wasserstoff und kohlensäure bei verschiedenen drucken erforderliche potentialdifferenz. *Ann. Phys.*, 273:69–96, 1889.

[135] H. Gerhardter, R. Prieler, S. Zausinger, and C. Hochenauer. Investigating the advantages of laval blasting nozzles in combination with injector-type sandblasters using efficient numerical methods. *Surface and Coatings Technology*, 445:128699, 2022.

[136] Hong Zhang, Kasra Darabi, Narges Yaghoobi Nia, Anurag Krishna, Paramvir Ahlawat, Boyu Guo, Masaud Hassan S. Almalki, Tzu-Sen Su, Dan Ren, Viacheslav Bolnykh, Luigi Angelo Castriotta, Mahmoud Zendehdel, Linfeng Pan, Sandy Sanchez Alonso, Ruipeng Li, Shaik M. Zakeeruddin, Anders Hagfeldt, Ursula Rothlisberger, Aldo Di Carlo, Aram Amassian, and Michael Grätzel. A universal co-solvent dilution strategy enables facile and cost-effective fabrication of perovskite photovoltaics. *Nature Communications*, 13(1):89, 2022.

[137] W. M. Haynes, David R. Lide, and Thomas J. Bruno, editors. *CRC Handbook of Chemistry and Physics*. CRC Press, 97 edition, 2016. ISBN 978-1-315-38047-6.

[138] Jihoon Kim, Si Bui Quang Tran, Baekhoon Seong, Hyungdong Lee, Giho Kang, Jin Hwan Ko, and Doyoung Byun. Experimental study on fluid selection for a stable taylor cone formation via micro-piv measurement. *Journal of Visualization*, 23(3):449–457, 2020.

[139] Zi Yang, Jingjin Fan, Jia Wang, Xiao Fan, Zheng Ouyang, Hong-Wei Wang, and Xiaoyu Zhou. Electrospray-assisted cryo-em sample preparation to mitigate interfacial effects. *Nature Methods*, 21(6):1023–1032, 2024.

[140] N. Roth. *Control of airborne nanoparticles*. PhD thesis, Deutsches Elektronen-Synchrotron, DESY, Hamburg, 2020.

[141] H.K. Versteeg and W. Malalasekera. *An introduction to computational fluid dynamics: the finite volume method*. Pearson/Prentice Hall, Harlow, 2. ed., [nachdr.] edition, 2007.

[142] D.J. Hucknall. *Vacuum technology and applications*. Butterworth-Heinemann, Oxford ; Boston, 1991.

[143] C.F. Bohren and D.R. Huffman. *Absorption and Scattering of Light by Small Particles*. Wiley Science Series. Wiley, 2008.

[144] B. Chu. *Laser Light Scattering 2e: Basic Principles and Practice*. Elsevier Science, Saint Louis, 2nd ed edition, 2014.

[145] B.E.A. Saleh and M.C. Teich. *Fundamentals of photonics*. Wiley series in pure and applied optics. Wiley, Hoboken, NJ, third edition edition, 2019.

[146] K. Uchino, editor. *Advanced piezoelectric materials: science and technology*. Woohead Publishing series in electronic and optical materials. WP, an imprint of Elsevier, Duxford ; Cambridge, MA, second edition edition, 2017.

[147] K.S. Suslick. *Ultrasound: its chemical, physical and biological effects*. VCH, New York Weinheim (RFA), 1988.

[148] Z. Qiao, Y. Huang, N. Vincenzo, and W. Dong. Aerosol manipulation by acoustic tunable phase-control at resonant frequency. *Powder Technology*, 281: 76–82, 2015.

[149] D. Zang, editor. *Acoustic levitation: from physics to applications*. Springer, Singapore, 2020.

[150] T.B. Jones. *Electromechanics of Particles*. Cambridge University Press, Cambridge, GBR, 2009.

[151] Z. Gong, Y.-L. Pan, G. Videen, and C. Wang. Optical trapping and manipulation of single particles in air: Principles, technical details, and applications. *Journal of Quantitative Spectroscopy and Radiative Transfer*, 214:94–119, 2018.

[152] E. Otte and C. Denz. Optical trapping gets structure: Structured light for advanced optical manipulation. *Applied Physics Reviews*, 7(4):041308, 2020.

[153] A. Ashkin. *Optical trapping and manipulation of neutral particles using lasers*. World Scientific, Singapore, reprint volume with commentaries edition, 2006.

[154] E. Skliutas, M. Lebedevaite, S. Kasetaite, S. Rekštytė, S. Lileikis, J. Ostrauskaite, and M. Malinauskas. A bio-based resin for a multi-scale optical 3d printing. *Scientific Reports*, 10(1):9758, 2020.

[155] R.S. Ketchum, P.E. Alcaraz, and P.-A. Blanche. Modified photoresins with tunable refractive index for 3d printed micro-optics. *Opt. Mater. Express*, 12(8): 3152–3160, 2022.

[156] K.P. Murphy. *Machine learning: a probabilistic perspective*. Adaptive computation and machine learning series. MIT Press, Cambridge, Mass., 4. print. (fixed many typos) edition, 2013.